NONLINEAR DYNAMICS OF

A ROTOR SUPPORTED BY HOMOPOLAR MAGNETIC BEARINGS

WITH SATURATION

A Dissertation

by

KYUNGDAE KANG

Submitted to the Office of Graduate Studies of
Texas A&M University
in partial fulfillment of the requirements for the degree of

DOCTOR OF PHILOSOPHY

December 2010

Major Subject: Mechanical Engineering

Nonlinear Dynamics of

a Rotor Supported by Homopolar Magnetic Bearings

with Saturation

NONLINEAR DYNAMICS OF

A ROTOR SUPPORTED BY HOMOPOLAR MAGNETIC BEARINGS

WITH SATURATION

A Dissertation

by

KYUNGDAE KANG

Submitted to the Office of Graduate Studies of
Texas A&M University
in partial fulfillment of the requirements for the degree of

DOCTOR OF PHILOSOPHY

Approved by:

Chair of Committee,	Alan B. Palazzolo
Committee Members,	Darbha Swaroop
	Reza Langari
	Thomas W. Strganac
Head of Department,	Dennis L. O'Neal

December 2010

Major Subject: Mechanical Engineering

ABSTRACT

Nonlinear Dynamics of a Rotor Supported by Homopolar Magnetic Bearings

with Saturation. (December 2010)

Kyungdae Kang, B.S., Yonsei Universtiy; M.S., Korea Advanced Institute of Science

and Technology; M.S., University of Texas at Austin

Chair of Advisory Committee: Dr. Alan B. Palazzolo

An objective in the design of high performance machinery is to minimize weight so magnetic bearings are often designed to operate slightly lower than the magnetic material saturation. Further weight reduction in the bearings requires operation in the nonlinear portion of the B-H curve. This necessitates a more sophisticated analysis at the bearing and rotordynamic system levels during the design stage. This dissertation addresses this problem in a unique manner by developing a fully nonlinear homopolar magnetic bearing model.

The nonlinear dynamics of permanent magnet-biased homopolar magnetic bearing (PMB HoMB) system with 2-dof rigid and 4-dof flexible rotor is analyzed. The dynamic behavior of the rotor-bearing system is examined in the feedback control loop that includes low pass filter effects.

An analytical magnetization curve model is proposed to predict the nonlinear magnetic force under the influence of the magnetic flux saturation more accurately. The modified Langmuir method with the novel correction terms for the weak flux region is

used to curve-fit the experimental magnetization data of Hiperco 50. A new curve fit model of the B-H curve is shown to have significantly better agreement with the measured counterpart than conventional piecewise linear and other models. PMB HoMB characteristics with flux saturation, such as forces depending on the rotor position and bearing stiffness, are compared with these other models.

Frequency response curve, bifurcation diagram, Poincare plot, and orbit plot are utilized to demonstrate the effects of the nonlinearities included in the 2-dof rotor-bearing system.

Due to heavy static loads applied to the rotor, it operates within the magnetic flux saturation region at the bearing clearance. The voltage saturation in the power amplifier of the magnetic bearing introduces lag in the control loop and the response of the heavily loaded 4-dof rotor-bearing system shows that limit cycle stability can be achieved due to the magnetic flux saturation or current saturation in the amplifier; otherwise the system would experience a destructive instability. These simulation results provide the first explanation of this commonly observed limit cycle which is referred to as 'virtual catcher bearings'.

DEDICATION

To my father and mother,

who have always given their love and support to me

To my wife,

who has devoted her life to supporting me,

and To my son,

who has let me know the joy of life.

ACKNOWLEDGEMENTS

I would like to express my gratitude to a number of people without whom it would not have been possible to complete this work. First of all, I would like to express my deepest appreciation to my advisor, Dr. Alan Palazzolo. He always provided me with invaluable guidance and insightful knowledge that led me to critical thinking to keep the research moving. As my mentor, his perseverance and enthusiasm for learning is going to be an example for the rest of my life. I am also thankful to Dr. Darbha Swaroop, Dr. Reza Langari and Dr. Thomas W. Strganac for serving on my advisory committee in spite of their busy schedules and for extending their valuable suggestions for my research.

There are many friends and colleagues who have been greatly helpful and I appreciate their support and care for me.

I would like to extend my deepest gratitude to my parents for their generous love, encouragement and boundless understanding. This work would not have been possible without the encouragement and support of my loving wife Jieun.

TABLE OF CONTENTS

LIST OF FIGURES

Page

LIST OF TABLES

CHAPTER I

INTRODUCTION AND LITERATURE LEVIEW

1.1   Introduction

Active magnetic bearings (AMB) have many advantages over conventional bearings such as ball bearings and journal bearings. The absence of lubrication system and mechanical wear that can cause any contamination makes it suitable for the application in the system required in vacuum and clean room. Energy storage flywheel exploits the magnetic bearing benefits of low power loss at high rotor speed and low maintenance requirement resulting from no mechanical friction. Also successful operation in industrial turbomachines with magnetic bearings was reported, such as compressors and turboexpanders in the oil and gas industry [1].

AMB have two general categories according to the magnetic pole arrangement, i.e., homopolar or heteropolar type. Magnetic South pole(S) and North pole(S) alternates in heteropolar AMB, while the same poles are placed on one plane in homopolar AMB. Diagrams of these two types of AMB are shown in Fig. 1.1. Because of the pole arrangement, homopolar AMB has two stator planes. Opposite poles are located on each plane and the axial flow of magnetic flux is always involved, which makes the magnetic flux paths mixed in radial and axial directions, whereas in heteropolar AMB the flux paths are mainly radial.

This thesis follows the style of *Journal of Sound and Vibration.*
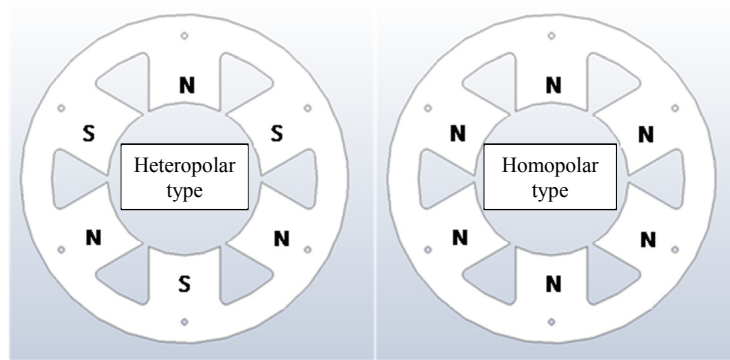
Fig. 1.1   Pole arrangement of heteropolar and homopolar magnetic bearing

The dissertation analyzes the nonlinear dynamics of permanent magnet-biased homopolar magnetic bearing (PMB HoMB) system. Because the static suspension forces are provided to the rotor primarily by permanent magnet flux, the electromagnetic forces from control current only handle the dynamic force compensation. PMB HoMB has advantages over heteropolar AMB from the aspect of power consumption; eddy current loss remains low since the rotor is not exposed to polar change when it rotates unlike the heteropolar type AMB and the current required for operation is less than heteropolar type AMB because of the permanent magnet bias flux[2, 3]. In addition, reliability can be increased by the extended lifetime of the power amplifier due to the reduced amount of power required for PMB HoMB. Disadvantages of PMB HoMB are the fixed bias flux level, a lower load capacity in some cases, or the necessity of two stator planes to utilize the axial flux[4].

Fig. 1.2 shows a magnetic bearing system that consists of several components such as controllers, power amplifiers, electromagnets, and position sensors. Because all these components possess some nonlinear behavior, the whole system is essentially

nonlinear[5]. Among those nonlinearities, the most important ones are as follows:

1. The nonlinear magnetic force to displacement and nonlinear force to coil current (or magnetic flux) relationship;

2. The nonlinear magnetization B-H curve (the saturation of the ferromagnetic core material);

3. The hysteresis of the magnetic core material;

4. The saturation of the power amplifier (voltage / current);

These nonlinearities are usually ignored to simplify the model and analysis, which makes only small motion around the operation point to be valid. In other words, with the nonlinear electromagnetic forces linearized about the operating point and considered to be linear functions of currents and air gaps, these linearized models can only be used to predict small rotor motions with small control current in the vicinity of the operating point. Thus, in order to utilize the full capacity of the magnetic bearings, nonlinear dynamic analysis with the model that includes the inherent nonlinearities of the magnetic bearing system is needed. The studies of the effect of nonlinearities on the dynamic behavior of magnetic bearing systems provide valuable insights into the system characteristics under variable operating cases that cannot be achievable with linear
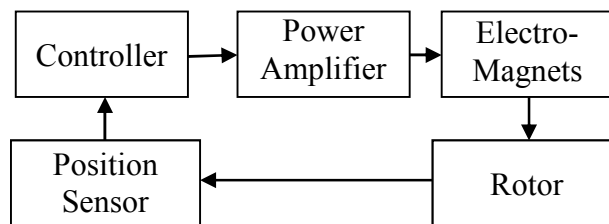
Fig. 1.2   Block diagram of a simple magnetic bearing system

modeling. Also, more precise model leads to the controller design which delivers reliable and stable operation.

1.2　Literature review

Previously, various functions, including rational function, power series, exponential functions, etc., have been used to model the magnetization curve accuratedly. But all these attempts use the equation form of B as a function of H, which is not suitable to solve the simultaneous equations derived from the magnetic circuit model of homopolar magnetic bearing. The equation form of H as a function of B makes it easier to solve those equations, because they can be arranged in terms of fluxes, ϕ. Macfadyen [6] investigated the approximation of magnetization curves by an exponential series. One example of typical magnetization curve for silicon steel is presented and shows good agreement from the low to high flux region, but this example has a low initial slope.

Widger [7] represented the magnetization curve by rational-fraction approximations. This approximations can be expressed either as H as a function of B or B as a function of H. With the relative or percentage errors minimized, the parameters of the approximation are found. A few examples of curve-fittings are shown, but the errors in the weak flux region are large. And this approximation method is not suitable for the magnetization curve that has very steep initial slope, sharp knee, and very shallow final slope, considering the example that shows almost 20% relative error in H.

Simatani [8] approximated the magnetization curve by exponential functions.

Macfadyen's function is modified to accommodate the magnetization curve in weak flux region. The magnetization curve is modeled with three equations in three different regions, but only one equation corresponding to the lowest part of the regions among these three regions is used to demonstrate the usefulness of the proposed method.

Rivas et al. [9] investigated the approximation of the magnetization curve with a second-order rational fraction function whose coefficients are related to material constants. But the curve-fitting qualities with this approximation are only good for magnetization curves that rise slowly and in which the knee portion has a large curvature.

Extensive research has been done in nonlinear dynamics analysis of rotor-AMB systems, but there are few publications dealing with the effect of magnetic saturation and amplifier voltage / current saturation on the nonlinear dynamic response of rotor. Maslen et al. [10] investigated the performance limits of heteropolar magnetic bearings, such as peak force, slew rate, and displacement sensitivity. He describes that peak force limitation is primarily due to the nonlinearity in the magnetization curve of the electromagnet core material and force slew rate limit is caused by the power amplifier voltage limit, which results in phase lag and reduction in both stiffness and damping in the bearing. For PMB HoMB, Lee et al. [11] studied similar performance limits. But these two papers do not deal with the effects of these limits on nonlinear dynamic response of a flexible rotor. They instead considered the magnetic core saturation in the maximum static force and the power amplifier voltage saturation in the force slew rate, respectively.

Antila [12] investigated the effect of power amplifier saturation on the large amplitude response at low frequency when high frequency disturbance that is added to this response saturates the amplifier. When the amplifier is saturated due to the high frequency large amplitude disturbance in the response, it is predicted that limit cycle oscillation may be possible, based on the reduced saturation effect and the phase increase which the large amplitude component at low frequency causes. But, it is not specified whether this is caused by voltage saturation, current saturation, or the both.

Steinschaden et al. [13] investigated the dynamics of active magnetic bearing systems for the case of large rotor eccentricities. He modeled the nonlinearities such as magnetic saturation effect, saturation of the amplifier and limitations of the control current, but only showed the results from the control current limitation. Also, he mentioned that bilinear type model of magnetic saturation he used is not suitable for the case of very high value of the magnetic flux density far above the saturation level that is starting point of the second linear part of the bilinear B-H curve. For specific parameter sets he used, symmetry breaking and quasiperiodic solution may occur from the effects of current saturation of the PID-controller.

Zhang et al. [14] studied two-dof rotor-AMB with 8 pole legs system considering time-varying stiffness, quadratic and cubic nonlinearities. The time-varying periodic coefficient is introduced to the proportional gain in the PD controller. Because heteropolar type AMB is used, the flux in each pole is independent of each other and the electromagnetic force resultant in x and y direction are expanded in power up to third-order terms. Using the method of multiple scales to obtain the averaged equations that

are solved numerically, it is found that there exist 2-period, 3-period, 4-period, 5-period, multi-period and quasiperiodic modulated amplitude oscillations.

Chinta [15] investigated the forced response of a two-dof rigid rotor in one heteropolar magnetic bearing for one-frequency harmonic excitation. Also, a simple bilinear model of magnetic flux saturation is used to analyze the effects of flux saturation on the rotor dynamics of a simple flexible rotor. The flux saturation reduces the maximum excitation forces in different manner depending on the rotor speed of a flexible rotor.

Nataraj [16] has discussed a nonlinear analysis of free and forced response of a simple rigid rotor supported on magnetic bearings that consists of four independent poles. With only the proportional controller gain in the linearized system, a qualitative analysis is carried in nondimensional parameter space to determine the range of safe operation which means the rotor response is within the physical bearing clearance. A forced response analysis predict that unbalance response can cause several resonances at various frequencies.

Satoh et al. [17] discussed the cause and mechanism of the self-exited vibration resulted from the interaction between voltage saturation of the power amplifier and the bearing support flexibility. The nonlinearity of force-to-displacement or force-to-current was not included. Stable regions of the rigid and flexible mode depending on the parameter φ at the operating point are found. The parameter φ is the ratio of the maximum voltage to the slope of the voltage limit plot. It is shown that the self-excited vibration contains two different frequency vibrations, and the rigid mode (low frequency

component) is caused by flexible mode (high frequency component).

A review of the types of nonlinearities and their resulting motions for rotating machinery is found in [18].

1.3 Contributions of this research

The development of a comprehensive model of magnetic bearing system is challenging but accurate model plays an important part in the dynamic analysis and controller design. Thus, including nonlinearities such as magnetic flux saturation, amplifier voltage / current saturation in the model may be critical to properly analyze the rotor magnetic bearing system in certain high performance applications.

The analysis of nonlinear dynamics of the flexible rotor that operates in the magnetic flux saturation zone may make it practical to utilize the full load capacity of the magnetic bearings by predicting the rotor response for the large motions or with heavy static loads.

The original contributions of this dissertation are:

(1) Modeling and simulation methodologies for including nonlinear effects in homopolar magnetic bearings. Prior methods focused on heteropolar magnetic bearings.

(2) Development of an improved accuracy curve fit of the magnetization curve. This analytical model of the magnetization curve provides a more accurate force prediction when the bearing is operating dynamically with both weak and high magnetic fluxes. Heavy static and dynamic loads applied to the

rotor causes the magnetic bearings to operate within the regions of the magnetic bearing clearance that cause flux saturation. The standard bilinear magnetization curve approach may be unsuitable for the analysis over flux saturation limit[13], which is explained in SECTION 3.1. Modeling error can be reduced by utilizing the new modified Langmuir method with correction terms for the weak flux region when Hiperco 50 experimental magnetization data is curve-fitted.

(3) In addition to magnetic flux saturation, the investigation is made into the nonlinear dynamics of rotor-AMB system including a flexible rotor, the effects of controller gains, low pass filter, amplifier dynamics, and amplifier voltage/current saturation.

(4) It is shown that the limit cycle is formed due to the magnetic flux saturation or the amplifier current saturation, even if the small motion, linearized feedback control loop is unstable. This explains experimental phenomenon observed.

(5) Investigation into nonlinear dynamics of rotor-AMB system with the above characteristics demonstrates the feasibility of the stable operation when the rotor operates in the saturated zone of PMB HoMB actuator. This provides a support for increasing the rated load capacity of the magnetic bearings, which will reduce their size / weight / costs.

1.4   Chapter summary

Chapter II presents Permanent magnet-biased homopolar magnetic bearing (PMB HoMB) and the rotor-bearing system model used through this dissertation, which is composed of the rotor model, the magnetic circuit model of PMB HoMB, the control system, the flux saturation model. Analytical magnetization curve for magnetic circuit equation is proposed to take the flux saturation into account. Chapter III presents PM HOMB characteristics such as forces and bearing stiffness. These characteristics with the proposed flux saturation model are compared with the cases of bilinear type flux saturation model. The case with the material reluctance excluded is also compared. The static force capacity of PMB HoMB with flux saturation is presented. Chapter IV presents the nonlinear dynamic responses of 2-dof rotor supported by PMB HoMB, when the flux saturation is considered in the magnetic circuit model. Heavy static load and large dynamic forces are assumed. Nonlinear system characteristics such as jump, bifurcation, and period-doubling path to chaos are clearly visible with the flux saturation model. The trigonometric collocation method is used to obtatin the periodic responses and the results are compared with the numerical integration as the benchmark. Chapter V investigates the effects of amplifier voltage / current saturation and flux saturation on the 4-dof rotor bearing system with heavy static load. Chapter VI concludes the dissertation by summarizing the contents and by presenting the directions for future research on the topic.

CHAPTER II

ROTOR-BEARING SYSTEM MODEL

The essential components of a magnetic bearing supported rotating machine are described below. Specific values are provided for some parameters which are later used in the results section.

2.1 Permanent magnet-biased homopolar magnetic bearing

A six-pole magnetic bearing consists of two stator lamination packs, 12 permanent magnets, electric coils on each pole, and back irons. Six permanent magnets are placed circumferentially on each stator lamination pack. Those permanent magnets provide the bias magnetic flux that flows both axially radially and is commonly used to provide the reaction force to counter the static load applied to the bearing. The control flux is generated by the electric coils and is restricted to radial flow in the rotor and stator lamination stacks. This flux component is used to regulate the shaft position at the target location within the magnetic bearing clearance circle (gap), and to produce desired
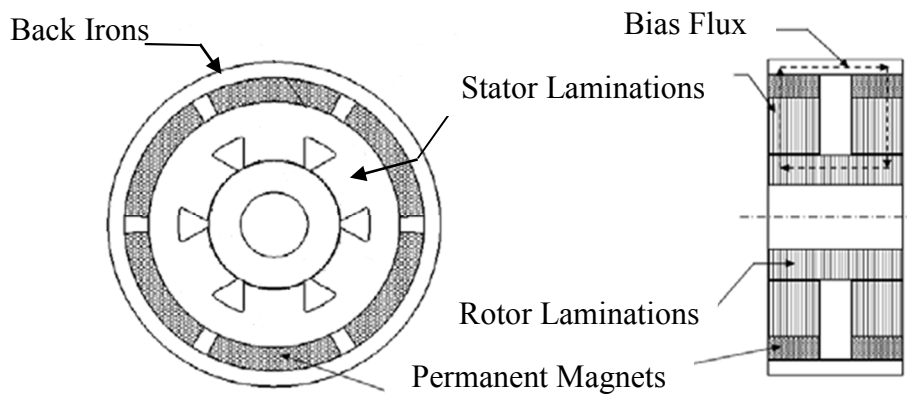
Fig. 2.1   Permanent magnet-biased homopolar magnetic bearing

stiffness, damping and disturbance cancellation forces. Fig. 2.1 shows the diagram of one permanent magnet-biased homopolar magnet bearing (PMB HoMB).

Stator laminate and back irons are made of Hiperco 50. The dimensional parameters of the bearing are described in Table 2.1. The magnetic properties of permanent magnet at room temperature are described in Table 2.2[19].

Table 2.1 Dimensional parameters of radial magnetic bearing

Pole length	Nominal air gap length	Inner radius of stator	Outer radius of rotor	Rotor length under bearing	Magnet length	Pole area	Air gap area	Magnet area
L_p (m)	L_g (m)	IR_{stator} (m)	OR_{rotor} (m)	L_r (m)	L_m (m)	$A_p(m^2)$	$A_g(m^2)$	$A_m(m^2)$
3.81×10^{-2}	5.08×10^{-4}	4.12×10^{-2}	4.06×10^{-2}	7.23×10^{-2}	1.83×10^{-2}	1.15×10^{-3}	1.15×10^{-3}	2.68×10^{-3}

Table 2.2 Magnetic properties of permanent magnet

Permeability of free space	Permeability of permanent magnet	Coercive field intensity of magnet	Residual flux density of magnet
μ_0 (H/m)	μ_{pm} (H/m)	H_c (kA/m)	B_r (T)
4πE-7	1.350E-6	633	0.855

2.2   Description of rotor-bearing system

The solid model of a magnetic bearing supported rotor-bearing system is shown in Fig. 2.2. The rotor is suspended by two sets of radial PMB HoMB's and a thrust bearing is used for axial position control. But the influence of the thrust bearing force is not included in the nonlinear analysis of the rotor-bearing system since it is typically the case that the radial and axial magnetic bearings are highly uncoupled. The rotor models of rigid 2-dof and flexible 4-dof are utilized in the analysis along with the PMB HoMB.

The magnetic bearing is modeled with 1-D magnetic circuit model including material reluctance and an analytical equation is proposed to curve fit to the experimental data of the BH magnetization curve of the material. The control system is described in detail at the SECTION 2.6.

2.3 Analytical magnetization curve model for magnetic circuit equation

Previous models[6-9] of the magnetization curve develop an equation for B as a function of H, however solution of a magnetic circuit model for flux requires a material description in the form of H as a function of B, which follows from Ampere's law stated in terms of H. This approach easily permits the system of coupled magnetic circuit equations to be expressed in terms of a set of fluxes, which are made independent by applying conservation of flux. This is illustrated in the following analysis of a homopolar magnetic bearing with permanent magnet bias and material saturation effects.

The Eq. (1) below is used for the initial curve fit to the experimental Hiperco 50 BH magnetization data that was published in NASA technical report[20].
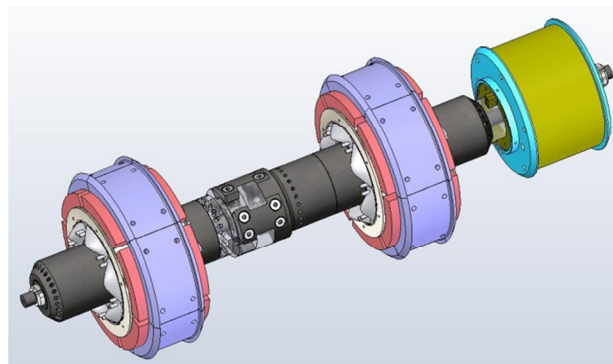
Fig. 2.2   Solid model of rotor-bearing system

$$H = \frac{P}{(1+Q \cdot B^R)^2}, \quad 0 \le B \le 2.4, \tag{1}$$

where H is the magnetic field intensity (A·turn/m); B is the magnetic flux density (Teslar); and P, Q, and R are the constants.

It is listed in Lab Fit software[21] as a predefined curve-fit function. This curve fit equation, so called 'modified Langmuir method', is a isotherm model proposed for the adsorption of solutes in a liquid solution onto a solid surface[22]. It results in excellent fit to the experimental data as shown in Fig. 2.3 in semi logarithmic scale except for the lower flux density zone below 0.8T. Fig. 2.4 is the magnified plot for ranging from 0 to 1000 H.

In the present work, the curve fitting equation is further modified to get better match with the experimental data and the final form of proposed function becomes a modified Langmuir method with a polynomial function multiplied by Gaussian function that acts as correction terms for the weak flux region, as Eq. (2).

$$H = \frac{P}{(1+Q \cdot B^R)^2} - P + \frac{1}{\sqrt{2\pi\sigma^2}} e^{-\frac{B^2}{2\sigma^2}} \cdot (a_0 + a_1 B + a_2 B^2 + a_3 B^3 + a_4 B^4 + a_5 B^5 + a_6 B^6), \tag{2}$$

where H is the magnetic field intensity (A·turn/m); B is the magnetic flux density (Teslar) ($0 \le B \le 2.4$); and P, Q, R, σ, $a_0 \sim a_6$ are the constants.

The constants in Eq. (2) can be determined by minimizing an appropriate cost function like Eq. (4).
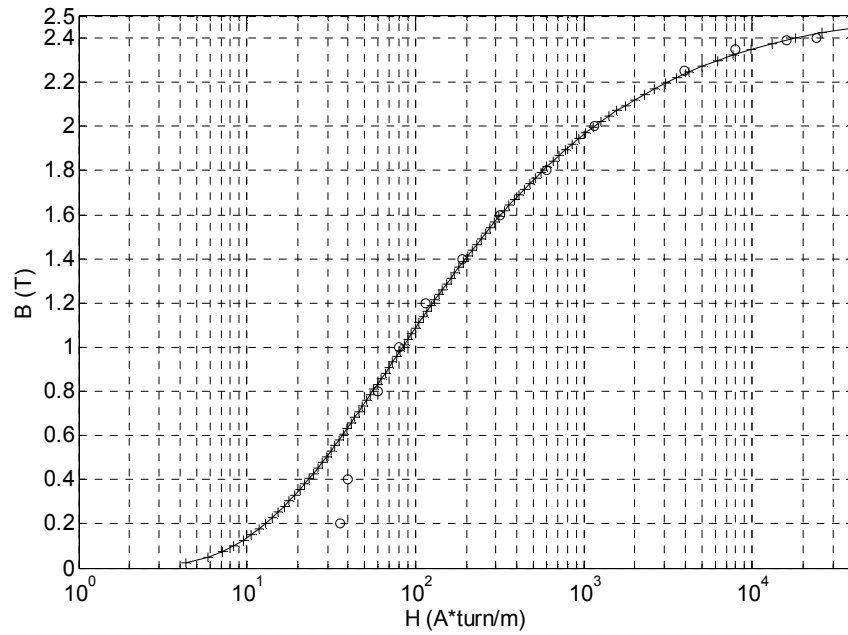
Fig. 2.3   Curve fitting with modified Langmuir method to the experimental Hiperco
50 data
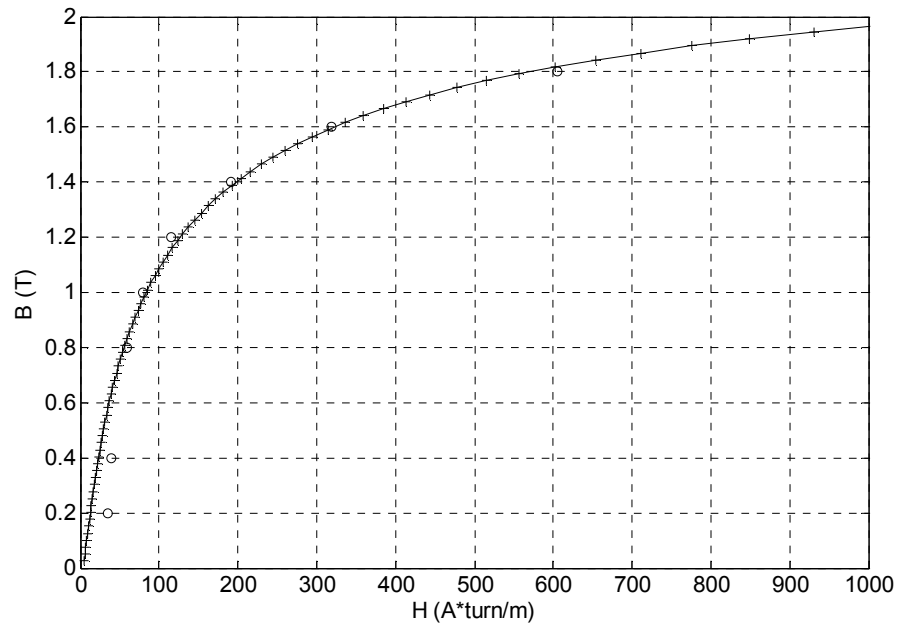
Fig. 2.4   Curve fitting with modified Langmuir method to the experimental Hiperco 50
data (Magnified for the range from 0 to 1000 H)

The relative deviation[23] D_i of the magnetic intensity $H(B_i)$ from the experimental values H_i appears in the cost function as:

$$D_i = \sqrt{\left(\frac{H(B_i) - H_i}{H(B_i) + H_i}\right)}, \tag{3}$$

where H_i and B_i are the experimental magnetization data of Hiperco 50 and $H(B_i)$ is calculated from Eq. (2).

The cost function has the form

$$F_{cost} = \sum_{i=1}^{n} h_i D_i, \tag{4}$$

where h_i is a weighting factor for i=1, …, n (n=13), and n is the number of experimental data points. The weighting factor h_i=1 are selected for all data steps except for the data around the knee curve region, which are 7th, 8th, 9th, and 10th data. The weight factor of 2 is given to these data.

Thus, the constants in Eq. (2) are determined by minimizing the cost function with the test data as:

$$
\begin{aligned}
&P = 0.994,\ Q = -0.891,\ R = 0.124, \\
&\sigma = 2.175 \times 10^{-1}, \\
&a_0 = 1.223 \times 10^{-3},\ a_1 = -5.729,\ a_2 = 2.166 \times 10^{3},\ a_3 = -1.578 \times 10^{4}, \\
&a_4 = 5.107 \times 10^{4},\ a_5 = -7.814 \times 10^{4},\ a_6 = 5.064 \times 10^{4}.
\end{aligned} \tag{5}
$$

At least three significant terms are needed after the decimal point to curve fit the data well until the saturation region.

Fig. 2.5 shows the modified curve fit that matches the entire experimental BH data from 0 to 2.4T and Fig. 2.6 is the magnified plot for ranging from 0 to 1000 H.
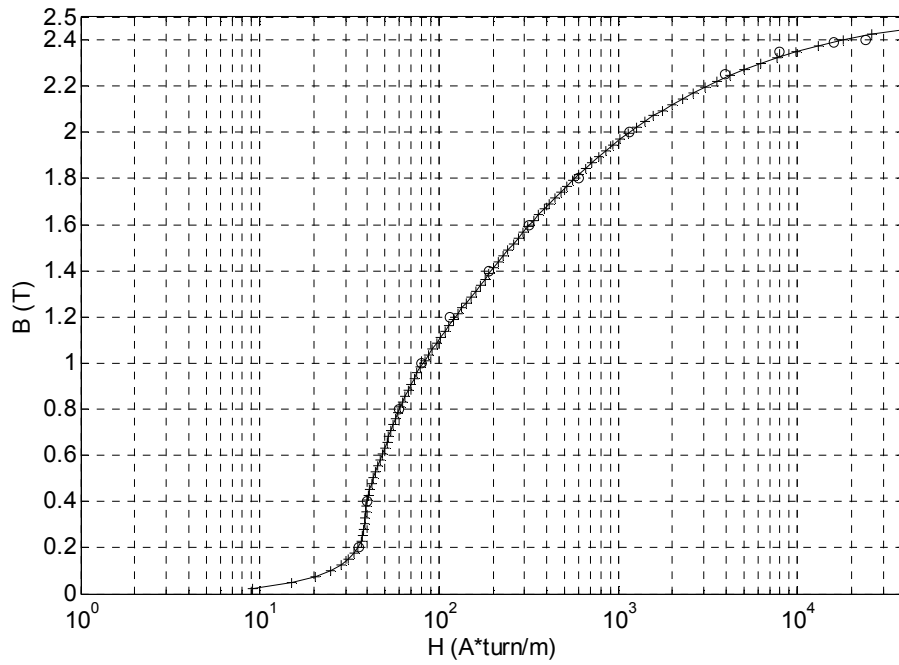
Fig. 2.5   Curve fitting to the experimental Hiperco 50 data with final form of curve fit
equation
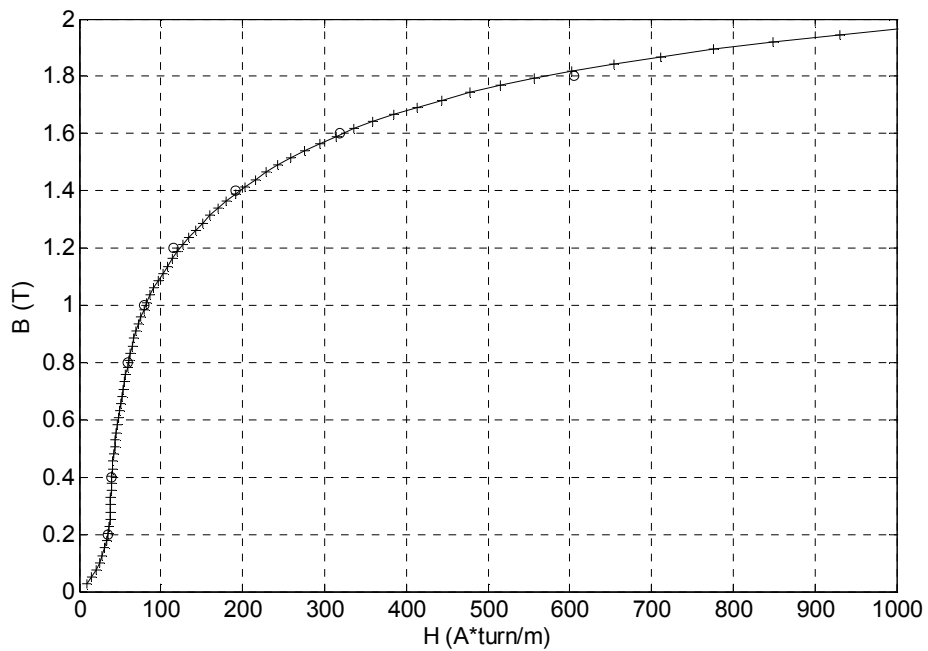
Fig. 2.6   Curve fitting to the experimental Hiperco 50 data with final form of curve fit
equation (Magnified for the range from 0 to 1000 H)

2.4   Magnetic circuit model

Some assumptions are made to model the magnetic bearing and to derive the equations from it, which are as follows:

1. Magnetic fluxes between two planes of the stator are symmetric.

2. Constant flux density on every flux carrying cross section (No fringing at air gap).

3. No leakage flux from permanent magnet.

4. Magnetic flux saturation occurs only in magnetic bearing poles.

The knowledge that the stator circumferential path is unlikely to saturate allows the stator circumferential reluctances to be removed [4]. This simplifies the model and also allows it to have just one element for the bias permanent magnet.

An equivalent magnetic circuit model of PMB HoMB is presented in Fig. 2.7. It includes 6 independent fluxes, 6 gap and 6 pole reluctances, 6 NI current sources and a lumped permanent magnet source along with its reluctance. The right hand side plane of Fig. 2.7 has an identical magnetic circuit as the left hand side and operates
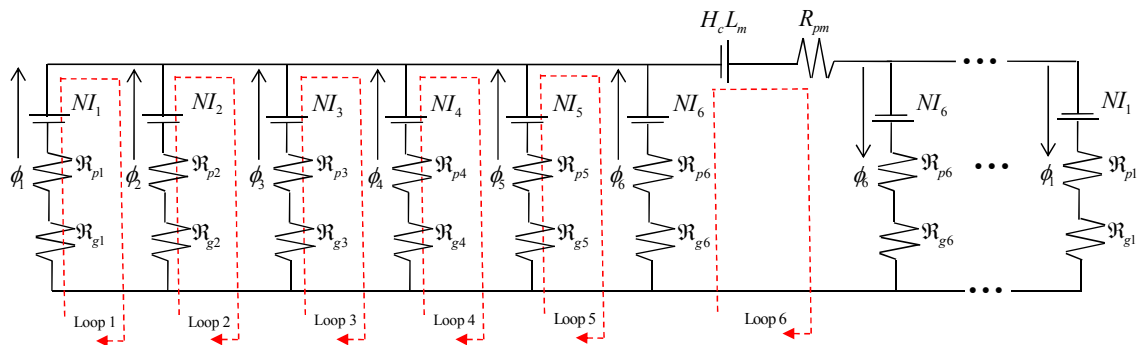
Fig. 2.7   1-D magnetic circuit model of homopolar magnetic bearing with permanent magnet and electric coil sources

symmetrically with identical sources, parameter values and fluxes. Hence the right hand side is only partially shown in Fig. 2.7. The magnetic circuit is a highly simplified, yet reasonably accurate representation of the actual 3-dimensional magnetic field that actually occurs in the real system. The circuit fluxes are typically reduced by a de-rate factor (typically 0.75 - 0.9) to account for fringing at air gaps and leakage around permanent magnets. For the sake of illustration, the model presented here utilizes unity de-rate factors and concentrates the material paths in the pole reluctance terms.

Loops from 1 to 5 represent the radial flux paths, with each loop containing the reluctances of the air gaps and the stator poles and the magneto-motive forces from the coils for an adjacent set of poles. The pole reluctances represent the general causal relation between source and flux including the nonlinear B-H expression in Eq. (2) which incorporates flux saturation into the model. The pole reluctances increase with saturation since they are inversely proportional to the slope of the BH curve in Fig. 2.5. The axial flux path is expressed in loop 6 which contains the permanent magnet source and reluctance terms. In this paper, only pole material is assumed to be saturated for the illustration purpose.

From Ampere's law given by Eq. (6), a single equation of the magnetic field for each loop is generated. The air gap reluctances are linear in their source-flux causal relation and are dependent on the instantaneous air gaps determined by radial motions of the journal. This dependence and the Maxwell stress tensor force formula's dependence on the square of flux, causes the magnetic bearing forces to become nonlinear functions of the displacement coordinates at the bearings. This holds even in the absence of

saturation in the material or in the feedback components.

Ampere's law Eq. (6) is applied to each loop to obtain 6 nonlinear algebraic Eq. (7) for the 6 unknown fluxes ϕ_i (i=1,…,6) and the H_{pi}-B_{pi} relation in Eq. (2) is substituted into Eq. (7). The magnetic bearing control currents and x and y gaps, in the air gap reluctance terms, change continuously as commanded by the controller when the magnetic bearing is operating. Therefore, in general Eq. (7) must be solved for the fluxes at each integration time step in the simulation of the entire rotor-bearing system.

$$\oint H(\phi)dl = NI \tag{6}$$

$$
\begin{aligned}
&\text{Loop1}: \ (H_{p1} - H_{p2})L_p + H_{g1}L_{g1} - H_{g2}L_{g2} = N(I_1 - I_2), \\
&\text{Loop2}: \ (H_{p2} - H_{p3})L_p + H_{g2}L_{g2} - H_{g3}L_{g3} = N(I_2 - I_3), \\
&\text{Loop3}: \ (H_{p3} - H_{p4})L_p + H_{g3}L_{g3} - H_{g4}L_{g4} = N(I_3 - I_4), \\
&\text{Loop4}: \ (H_{p4} - H_{p5})L_p + H_{g4}L_{g4} - H_{g5}L_{g5} = N(I_4 - I_5), \\
&\text{Loop5}: \ (H_{p5} - H_{p6})L_p + H_{g5}L_{g5} - H_{g6}L_{g6} = N(I_5 - I_6), \\
&\text{Loop6}: \ H_{p6}L_p + H_{g6}L_{g6} + H_{pm}L_m = NI_6 + H_c L_m,
\end{aligned}
\tag{7}
$$

where

$$
H_{pi} = \frac{P}{(1+Q \cdot B_{pi}^{R})^2} - P + \frac{1}{\sqrt{2\pi\sigma^2}} e^{-\frac{B_{pi}^2}{2\sigma^2}} \cdot (a_0 + a_1 B_{pi} + a_2 B_{pi}^2 + a_3 B_{pi}^3 + a_4 B_{pi}^4 + a_5 B_{pi}^5 + a_6 B_{pi}^6)
$$

, magnetic field intensity of the ith pole material, i= 1~6;

$B_{pi} = \dfrac{\phi_i}{A_p}$, flux density of the ith pole material, i= 1~6;

$H_{gi} = \dfrac{\phi_i}{\mu_0 A_g}$, magnetic field intensity of the ith air gap, i= 1~6;

$H_{pm} = \dfrac{\phi_i}{\mu_{pm} A_m}$, magnetic field intensity of the permanent magnet (A·turn/m);

μ_0: permeability of free space;

μ_{pm}: permeability of the permanent magnet;

H_c: coercivity of the permanent magnet;

L_p: length of the pole;

L_{gi}: instantaneous length of the ith air gap, i= 1~6;

L_m: length of the permanent magnet;

N: the number of coil turns on each pole;

I_i: current applied to i^{th} pole, i= 1~6

Air gap L_{gi} can be found by Eq. (8)

$$L_{gi} = L_{g0} - x\cos\theta_i - y\sin\theta_i, \tag{8}$$

where L_{g0} is the nominal air gap when the shaft is at the bearing center, $\theta_i = 30 + 60 \times (i-1)$ degrees, i=1,…6.

The PMB HoMB magnetic circuit model of Eq. (7) provides a means to calculate the 6 fluxes shown in Fig. 2.7 given the instantaneous currents in the 6 poles and the X and Y journal coordinates. The Levenberg-Marquardt algorithm[24] is used to solve the set of nonlinear algebraic Eq. (7), given that the solution for the fluxes from the previous time step are used as initial guesses of their values for the present step.

Fluxes from Eq. (7) are utilized in Eq. (9) to determine the X and Y forces.

$$F_i = \frac{\chi_i \phi_i^2}{2\mu_0 A_g}, \quad i = 1,...,6, \qquad F_{x,m} = \sum_{i=1}^{6} F_i \cos(\theta_i), \qquad F_{y,m} = \sum_{i=1}^{6} F_i \sin(\theta_i), \tag{9}$$

where A_g is the air gap area, $\theta_i = 30 + 60 \times (i-1)$ degrees, i=1,…6 (pole number).

The forces are modified by the derate factors χ_i to correct the 1-D magnetic circuit model for 2-D and 3-D effects, including fringing and leakage. The derate factors are typically selected in the range 0.7~0.9, although for sake of illustration the results here are shown for $\chi_i = 1$. The poles are positioned 60 degrees apart and the pole #1 is located at 30 degrees counter clockwise from X axis, as shown in Fig. 2.1.

2.5 Rotor model

In this nonlinear dynamic analysis, the rotor is modeled as 2-dof rigid rotor with a radial PMB HoMB and as four-dof flexible rotor model with two, radial PBM HoMB. Fig. 2.8 shows the diagram of the two-dof rigid rotor model including the bearing and shaft lumped mass, static and imbalance loads, and bearing coordinates. Equation of motion for two-dof rotor model is represented in Eq. (10). In Fig. 2.9, the four-dof flexible rotor model is depicted with the bearings, central disk and bearing lumped masses, static imbalance loads, and bearing and disk coordinates. The flexible model
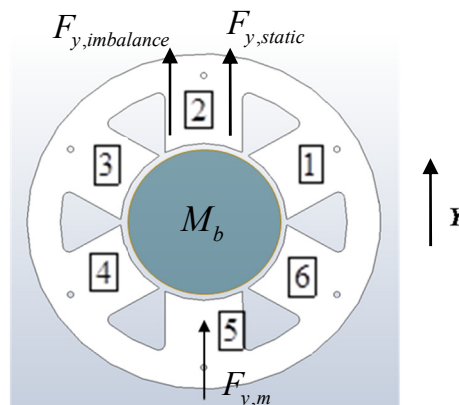
Fig. 2.8   Rigid rotor model with 2 dofs and Y direction static loading

neglects gyroscopic effects, and the resulting equations of motion with imbalance force and static force in the negative y direction are shown in Eq. (11). The shaft model is simplified relative to those of actual compressors, turbines, etc. in order to focus on the high fidelity, nonlinear magnetic bearing model and to make the system model more amenable to numerical integration based simulation. The target positions for the journals in the magnetic bearings are intentionally set above the centers of the magnetic bearing clearance circles in order for the static load to be balanced by the permanent magnet bias flux. This commonly employed approach yields a significant reduction in coil currents and in the resulting ohmic losses.

$$
\begin{aligned}
M_b \ddot{x} &= F_{x,m} + M_b e \omega^2 \cos(\omega t), \\
M_b \ddot{y} &= F_{y,m} + M_b e \omega^2 \sin(\omega t) + F_{y,static},
\end{aligned}
\tag{10}
$$

$$
\begin{aligned}
M_b \ddot{x}_b + k_r (x_b - x_d) &= F_{x,m}, \\
M_d \ddot{x}_d + k_r (x_d - x_b) &= M_d e \omega^2 \cos(\omega t), \\
M_b \ddot{y}_b + k_r (y_b - y_d) &= F_{y,m}, \\
M_d \ddot{y}_d + k_r (y_d - y_b) &= M_d e \omega^2 \sin(\omega t) + F_{y,static},
\end{aligned}
\tag{11}
$$

where

M_b = concentrated mass lumped at the bearing,

M_d = concentrated mass lumped at the central disc,

k_r = effective shaft stiffness connecting the bearings and the disc,

ω = shaft spin rate in rad/sec,

e = eccentricity of disc mass center,

$F_{y,static}$ = static load applied to central disc,

$F_{x,m}, F_{y,m}$ = magnetic bearing x and y forces.
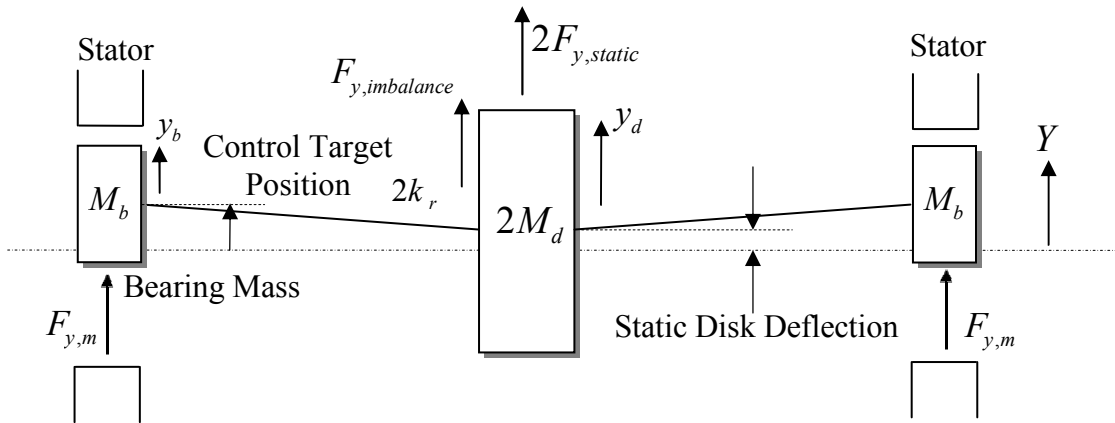
Fig. 2.9   Flexible shaft model with four dos and Y direction static loading

2.6   Control system

Each magnetic bearing has 2 parallel stator and rotor stacks of laminations that are offset axially, and are sometimes referred to as "active planes". Axially adjacent poles in these stacks have identical coils, are wired in series and are powered by the same power amplifier to which the vertical and horizontal control voltages are divided into 6 voltages by the current distribution matrix (**CDM**) and supplied. This approach facilitates fault tolerant operation (FTO) of the PMB HoMBs as explained in [25]. Implementation of FTO requires use of a "decoupling choke", as shown in Fig. 2.10, to electrically stabilize the magnetic bearing by converting a singular inductance matrix into a diagonal matrix with zero mutual inductances between the poles. This approach for FTO was first proposed in [26] for heteropolar magnetic bearings (HeMB). The model used here has fully operational coils since FTO is not of primary importance in this study.
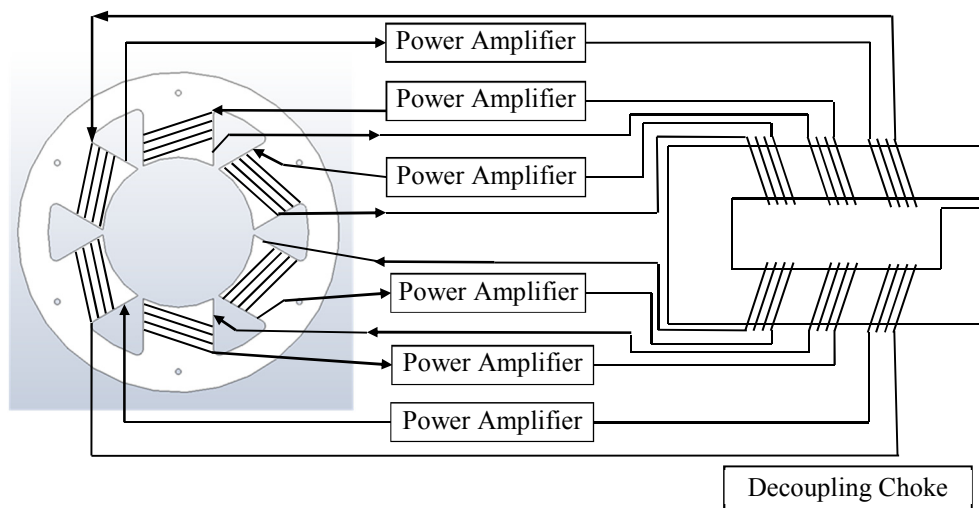
Fig. 2.10 Decoupling choke that is connected to power amplifiers and coils
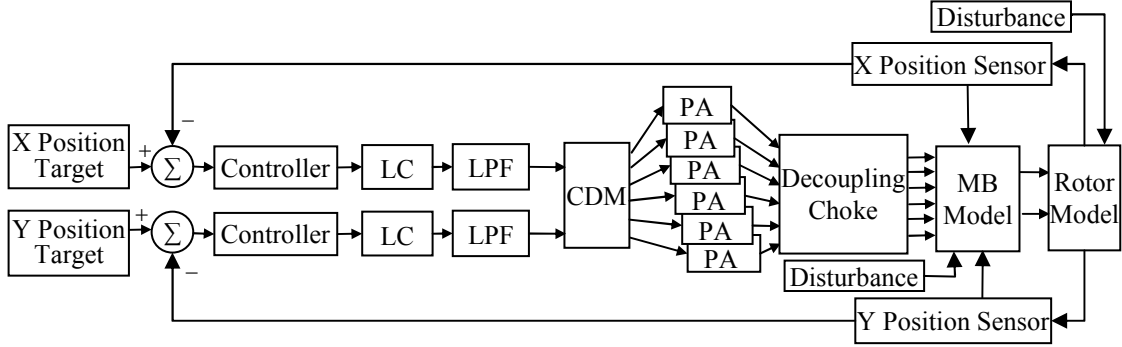
Fig. 2.11 Diagram for journal motions feedback position control

The 6 power amplifiers in Fig. 2.11 drive currents through the 6 pole-coil pairs to produce x any y radial control forces at each bearing. The controller is composed of a proportional-derivative PD stage, lag compensation (LC) and a low pass filter (LPF) to represent input and output filters on a digital controller. This model is again simplified to focus primarily on the nonlinear aspects of the model, while utilizing credible components in other areas. Inclusion of the LC, LPF and power amplifier (PA) dynamics in the model accounts for the loss in phase margin that destabilizes real magnetic bearing systems. The LC is employed as a pseudo-finite gain integrator to reduce the static offset error (droop) caused by the static loading. The inductances of the coils are assumed to be constant. Transfer functions for the LC, LPF, and PA are described in Eqs. (8), (9), and (10), respectively.

$$D_{LC}(s) = \frac{s+z}{s+p}, \quad z > p. \tag{12}$$

$$D_{LPF}(s) = \frac{1}{(\tau s + 1)^2}, \quad \tau = \frac{1}{2\pi f_c}, \quad f_c : \text{cutoff frequency.} \tag{13}$$

$$D_{PA}(s) = \frac{1}{Ls+R}, \quad L:\text{coil inductance}, \ R: \text{ coil resistance.} \tag{14}$$

The X and Y control voltages are routed into a current distribution matrix (**CDM**) [25] which outputs linear combinations of the input voltages to the 6 power amplifiers (PA's) that drive currents through the 6 pole/coil pairs, as shown in Fig. 2.11. The parameter values for **CDM** are as follows

$$\mathbf{CDM} = \begin{bmatrix} 0.5615 & 0.3242 \\ 0 & 0.6484 \\ -0.5615 & 0.3242 \\ -0.5615 & -0.3242 \\ 0 & -0.6484 \\ 0.5615 & -0.3242 \end{bmatrix}. \tag{15}$$

Any of the PA voltages or currents may saturate as indicated by Fig. 2.12, where $V_{CDM,i}$ is the output voltage from the **CDM**, $V_{amp,i}$ is the voltage output and I_i is the current output from PA (i=1, … ,6), and γ is the current feedback gain (V/A).

The possible disturbance input to the magnetic bearing is the sensor runout. The
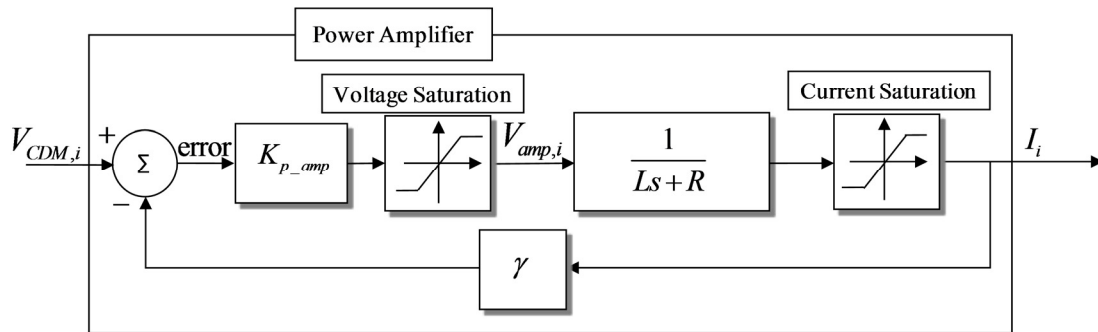
Fig. 2.12 Simplified power amplifier model with output voltage / current saturation limiters

unbalance force and static load is the disturbance input to the rotor model in this analysis.

Different configurations are used for 2-dof and 4-dof rotor models. As shown in Fig. 2.11, the controller with LC, LPF, PA dynamics is used in the analysis involving 4-dof rotor model, while all of which are not considered with 2-dof rotor model. Magnetic flux saturation is included in the component of magnetic bearing model in each rotor model analysis.

CHAPTER III

PMB HOMB CHARACTERISTICS WITH FLUX SATURATION

In this chapter, the bearing forces generated from the proposed BH curve model is compared with the forces from a bilinear model. The bearing stiffness with the proportional gain from both the proposed BH model and material reluctance exclusion are compared.

3.1 Force comparison between bilinear and modified Langmuir model

The bilinear B-H curve model [13] shown in Eq. (16) provides the effective relative permeability values.

$$\mu_{r,mi} = \frac{1-\mu_{r,mi,0}}{\pi} \arctan\left(K_{M,mi} \frac{|B_{mi}| - B_{mi,\max}}{B_{mi,\max}} \right) + \frac{1+\mu_{r,mi,0}}{2}, \tag{16}$$

where $\mu_{r,mi,0}$ is the relative permeability well below the saturation value $B_{mi,\max}$, B_{mi} is the actual magnetic flux density, $K_{M,mi}$ is a shaping factor of the B-H curve, and i denotes the number of poles (i=1,…,6). Fig. 3.1 shows the Y direction force vs. Y direction journal position, as determined from the magnetic circuit model with the proposed B-H curve model from Eq. (2) and the bilinear type B-H curve model from Eq. (16).

The control currents are all set to zero so the flux is driven only with the permanent magnets. The parameter values utilized in Eq. (16) are: $\mu_{r,mi,0} = 8000$, $B_{mi,\max} = 2.0$, and $K_{M,mi} = 100$. The coercive field intensity of magnet (H_c) is 633 kA/m and the residual flux density of magnet (B_r) is 0.855 T at room temperature. The air gap length of PMB HoMB is 5.080×10^{-4} m. Permanent magnet and magnetic bearing properties are listed in
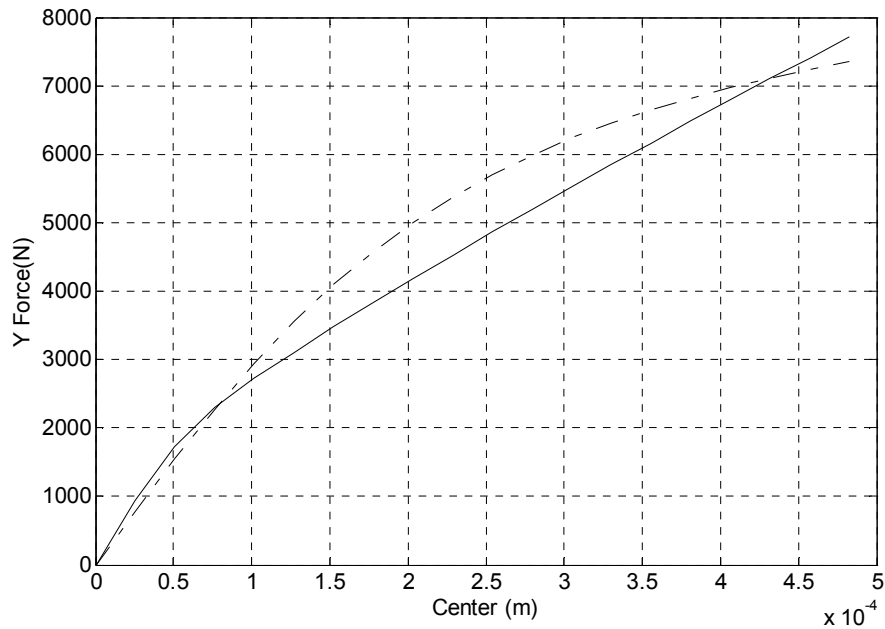
Fig. 3.1 Y direction force vs. Y direction journal position with the bilinear
and proposed saturation model. Key: —, bilinear; -·-, proposed

Table 2.1 and Table 2.2.

As seen in Fig. 3.1, the force generated when the bilinear type B-H curve model is used is not as large as the one with the proposed B-H curve model beyond 7.6×10^{-5}m in the Y direction. The proposed B-H curve model closely follows the experimental data, thus the bilinear B-H curve model is less suitable for rotor motion simulations involving magnetic fluxes that exceed saturation levels. Fig. 3.2 shows the flux density in each pole as a function of journal position in the Y direction utilizing the proposed and bilinear B-H curve model.
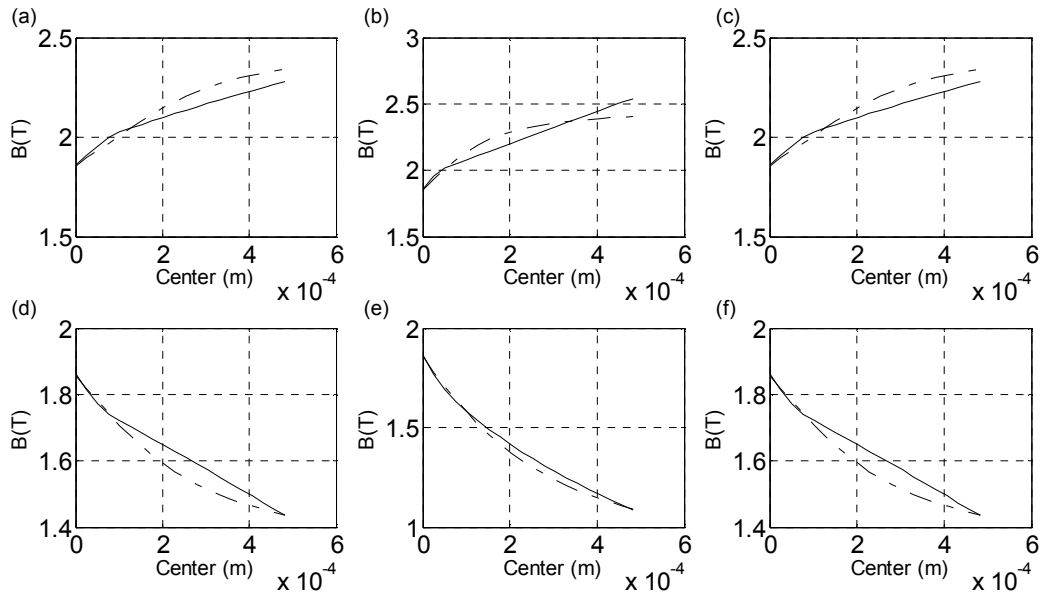
Fig. 3.2 Flux density in each pole vs. Y journal position. Key: —, bilinear; – -, proposed. (a) pole 1, (b) pole 2, (c) pole 3, (d) pole 4, (e) pole 5, and (f) pole 6

3.2 Force comparison between model without flux saturation and modified Langmuir model

The PMB HoMB force with the proposed flux saturation model is investigated compared to the force without flux saturation. Fig. 3.3 shows the Y direction force vs. Y direction journal position, as determined from the magnetic circuit model with the proposed B-H curve model, when the control currents are all set to zero so the flux is driven only with the permanent magnets. As the journal moves in Y direction, the air gap between the journal and bearing top three poles, or pole 1, pole 2, and pole 3 as shown in Fig. 2.8, decreases, and the fluxes at these poles are saturated as shown in Fig. 3.4. Therefore, the slope becomes gentle as the journal approaches the bearing clearance

limit. On the contrary, the force determined from the magnetic circuit model without the material reluctance shows that the position stiffness grows as the journal gets close to the bearing top 3 poles and it deviates unreasonably from its counterpart found from the proposed flux saturation model. Fig. 3.5 shows the comparison between these two force characteristics and the corresponding poles flux density plots are in Fig. 3.6.

By comparing these two models, it can be concluded that the nonlinear dynamic analysis with the force determined from the magnetic circuit model which includes the proposed B-H curve model is more appropriate when the large amplitude response is involved or the journal center is offset from the bearing center because of the heavy load applied to the journal.
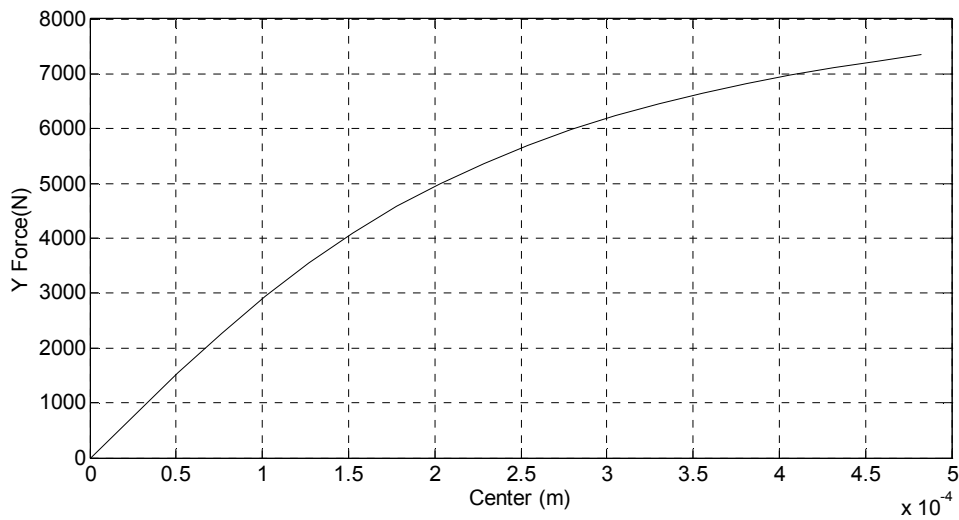
Fig. 3.3   Y direction force vs. Y direction journal position with the proposed
saturation model
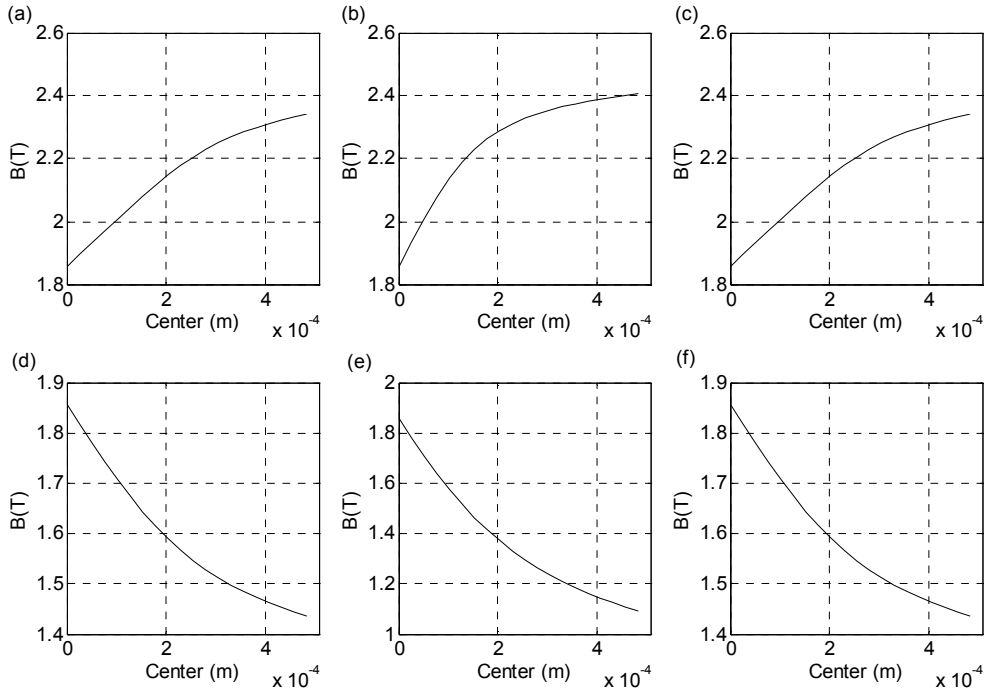
Fig. 3.4   Flux density in each pole vs. Y journal position. (a) pole 1, (b) pole 2, (c) pole 3, (d) pole 4, (e) pole 5, and (f) pole 6
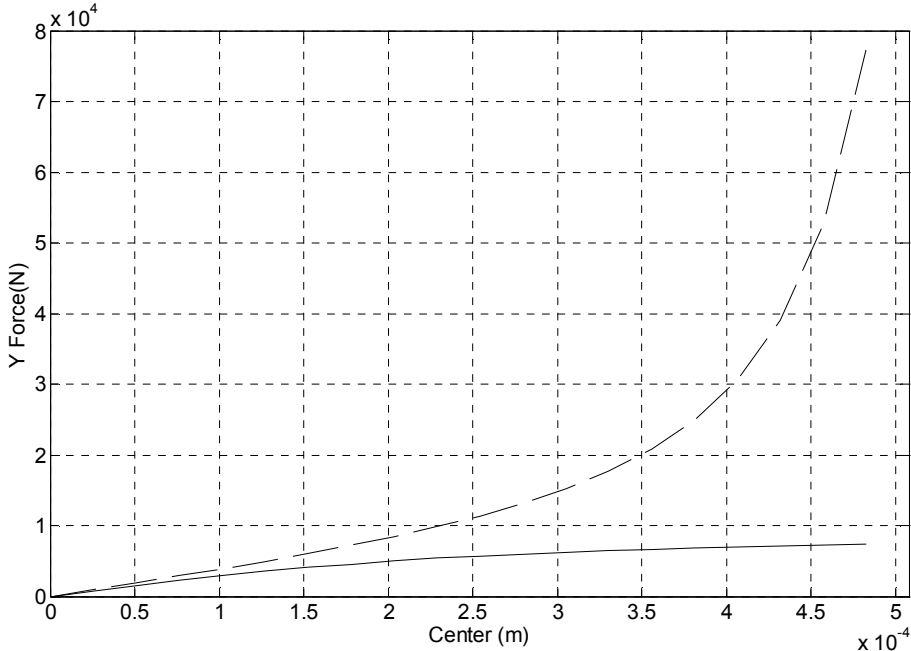
Fig. 3.5   Y direction force vs. Y direction journal position with the proposed saturation model and without the material saturation. Key: —, with saturation; - -, without saturation
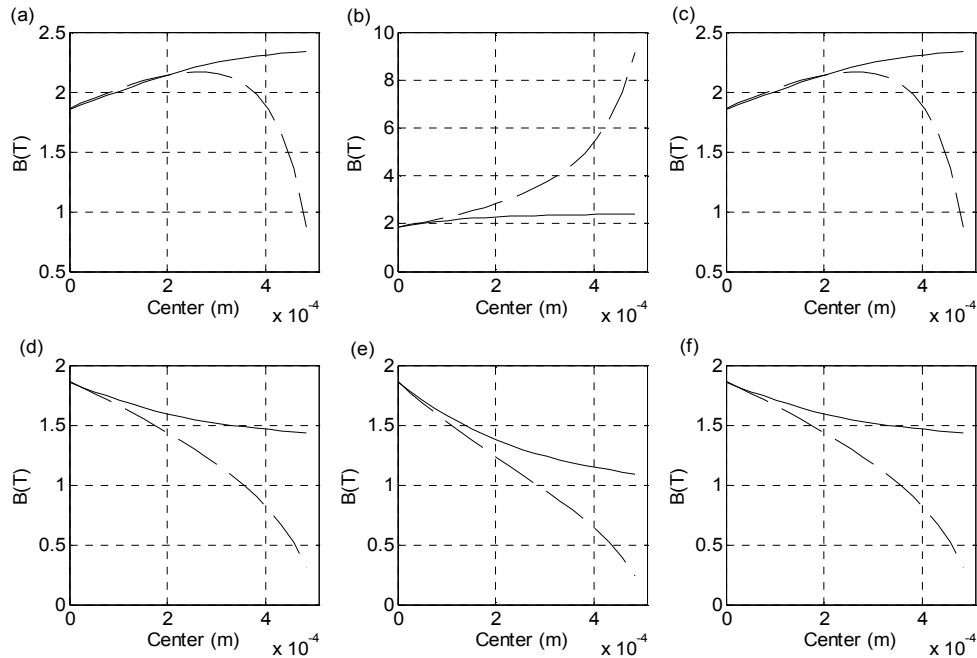
Fig. 3.6   Flux density in each pole vs. Y journal position. Key: —, with saturation; - -, without saturation. (a) pole 1, (b) pole 2, (c) pole 3, (d) pole 4, (e) pole 5, and (f) pole 6

3.3   Nonlinear bearing stiffness comparison

The resultant magnetic forces in Y direction acting on the shaft with several cases of the proportional gain G_p, setting $G_d = 0$, are shown in Fig. 3.7, Fig. 3.8, and Fig. 3.9. The shaft is moved in Y direction and held at each step of position and the Y direction forces are numerically found with both the magnetic circuit model containing the proposed BH curve model and the model excluding the material reluctance. Because the control target position is at the bearing center coordinate, the forces at Y=0 is zero and positive Y displacements lead to stable restoring forces in negative Y direction, staring from zero at the bearing center.

Fig. 3.7 with the proportion gain $G_p = 33.68$ shows a hardening spring characteristics. The forces generated with flux saturation are slightly less that the forces without flux saturation. The force difference is not significant with this amount of proportional gain within the half of the bearing clearance, 2.54x10^{-4}m, though the difference gets larger as Y displacement approaches the clearance limit, 5.08x10^{-4}m. The flux density calculated with flux saturation model remains less than 2 Tesla, shown in Fig. 3.10.

The force with the proportional gain $G_p = 60.39$ and $G_p = 96.01$ is shown in Fig. 3.8 and Fig. 3.9, respectively, and corresponding flux densities in each pole are plotted in Fig. 3.11 and Fig. 3.12. These two cases indicate that the bearing has hardening spring characteristics. With the hardening spring characteristics, the forces calculated from the model excluding the material reluctance shows large deviation from the forces including flux saturation and these comparisons along with the result in SECTIONS 3.1 and 3.2 clearly manifests that the force model with the proposed BH curve is more suitable for the analysis involving rotor response with large amplitude or within flux saturation region.

Fig. 3.13 is plotted with Y forces at each journal displacement step, including flux saturation for the different values of proportional gains. Fig. 3.14 shows how the bearing stiffness coefficients, K_y, changes with the shaft displacement in Y direction for the different values of proportional gains.
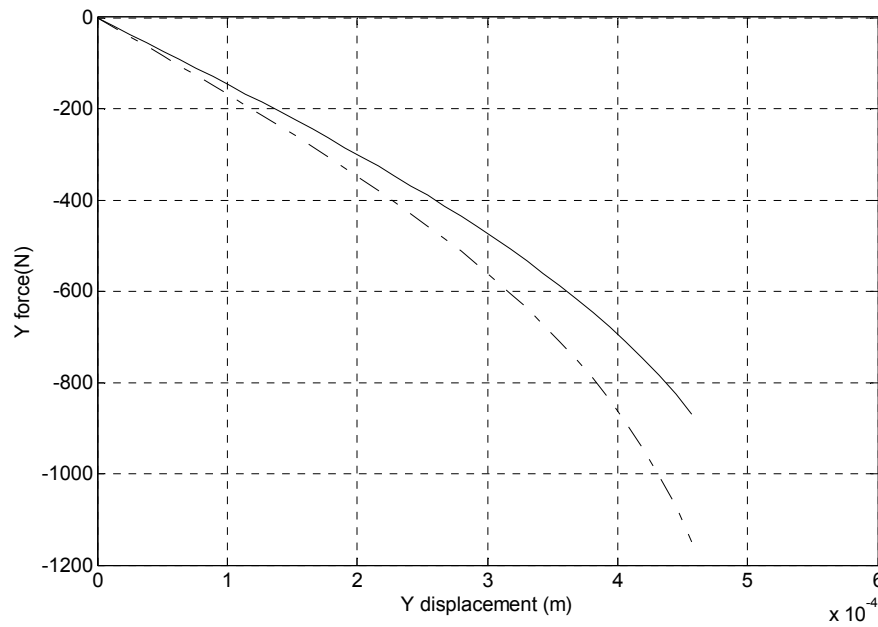
Fig. 3.7   Y direction force vs. Y displacement with proportional gain G_p=33.68. Key:
—, with flux saturation; - -, without flux saturation
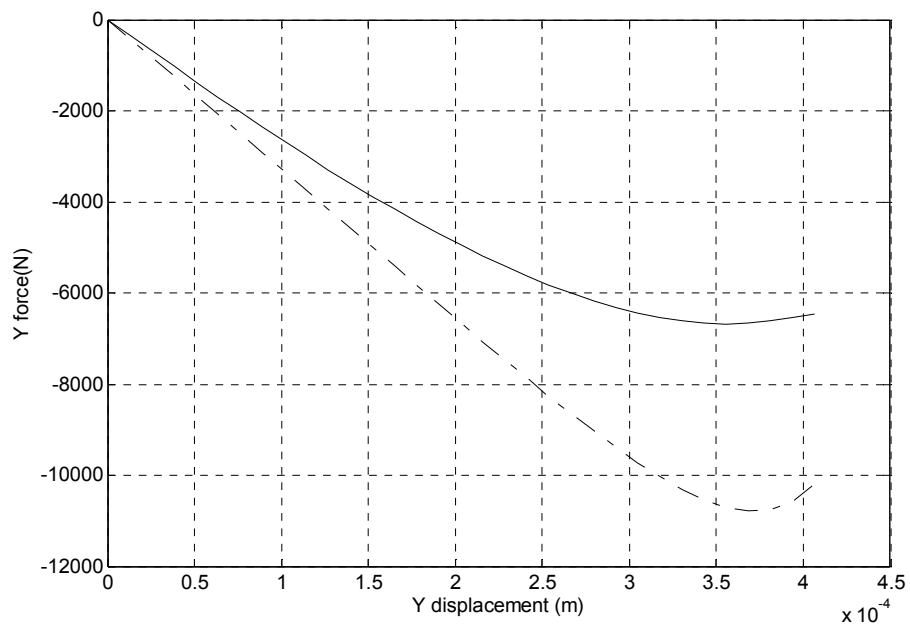
Fig. 3.8   Y direction force vs. Y displacement with proportional gain G_p = 60.39.
Key: —, with flux saturation; - -, without flux saturation
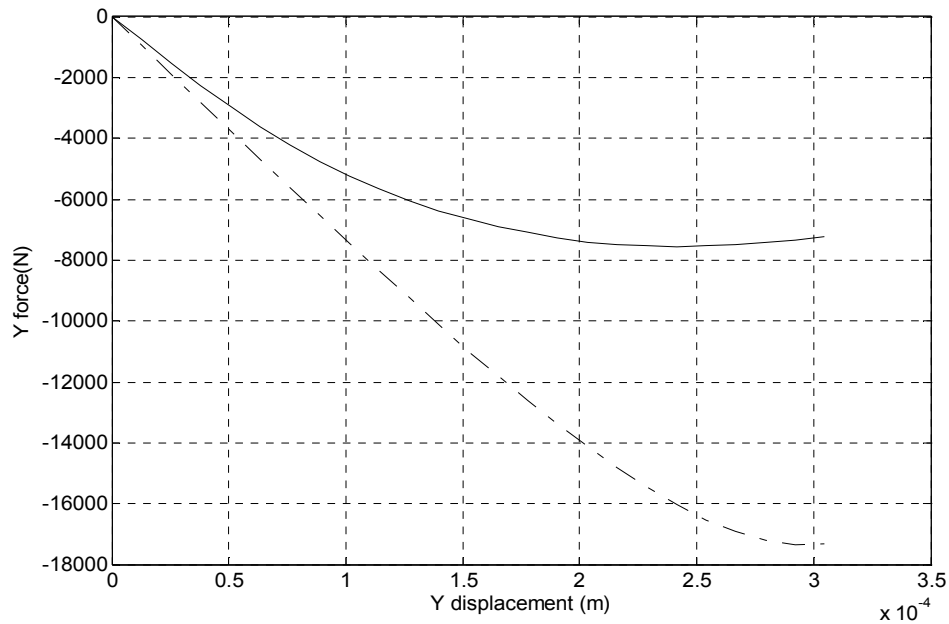
Fig. 3.9   Y direction force vs. Y displacement with proportional gain $G_p = 96$.
Key: —, with flux saturation; - -, without flux saturation
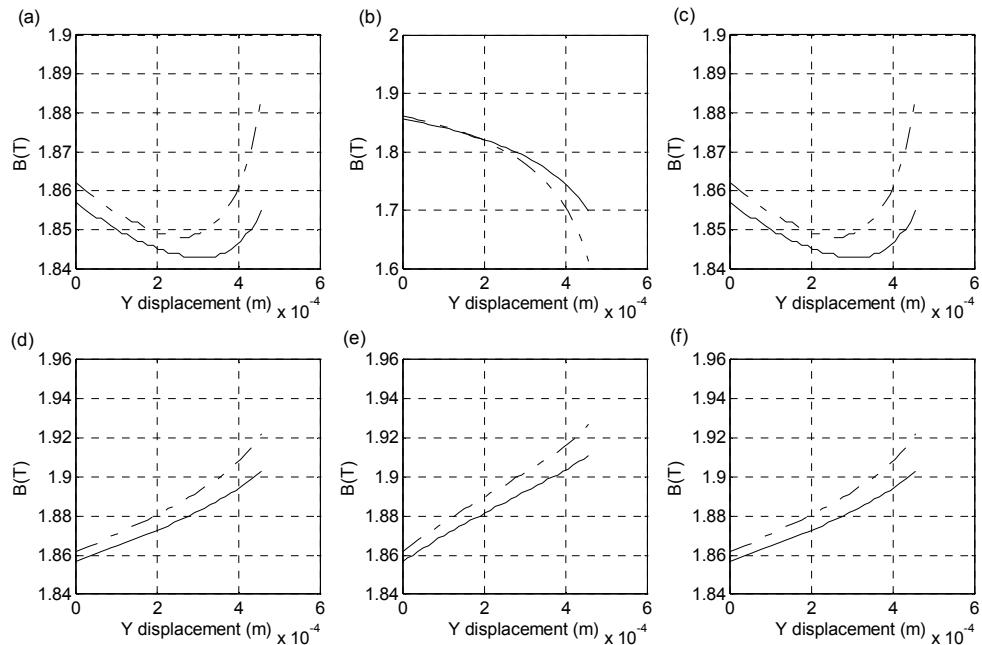
Fig. 3.10 Flux density vs. Y journal position with $G_p = 33.68$. Key: —, with flux
saturation; - -, without flux saturation. (a) pole 1, (b) pole 2, (c) pole 3, (d)
pole 4, (e) pole 5, and (f) pole 6
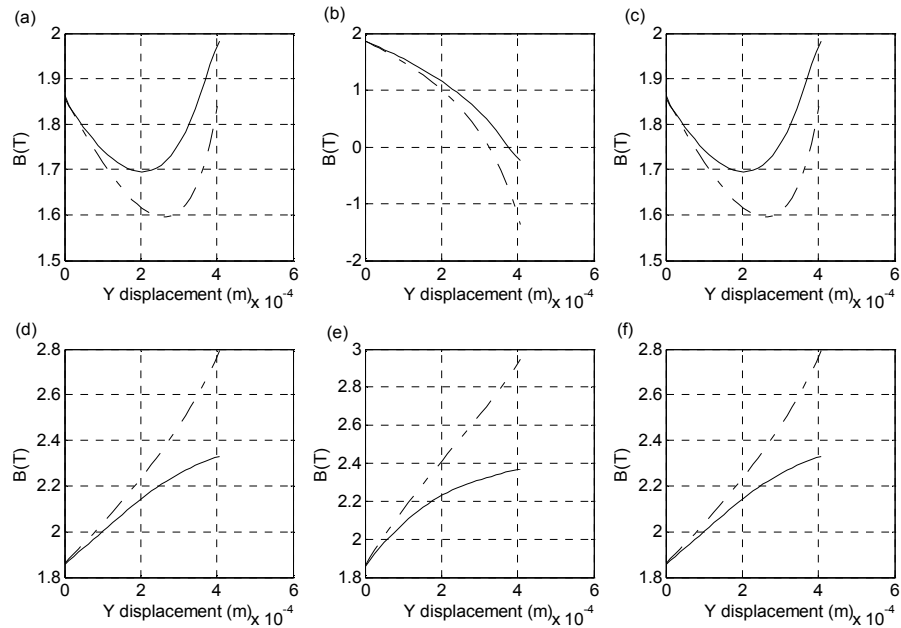
Fig. 3.11 Flux density vs. Y journal position with $G_p = 60.39$. Key: —, with flux saturation; - -, without flux saturation. (a) pole 1, (b) pole 2, (c) pole 3, (d) pole 4, (e) pole 5, and (f) pole 6
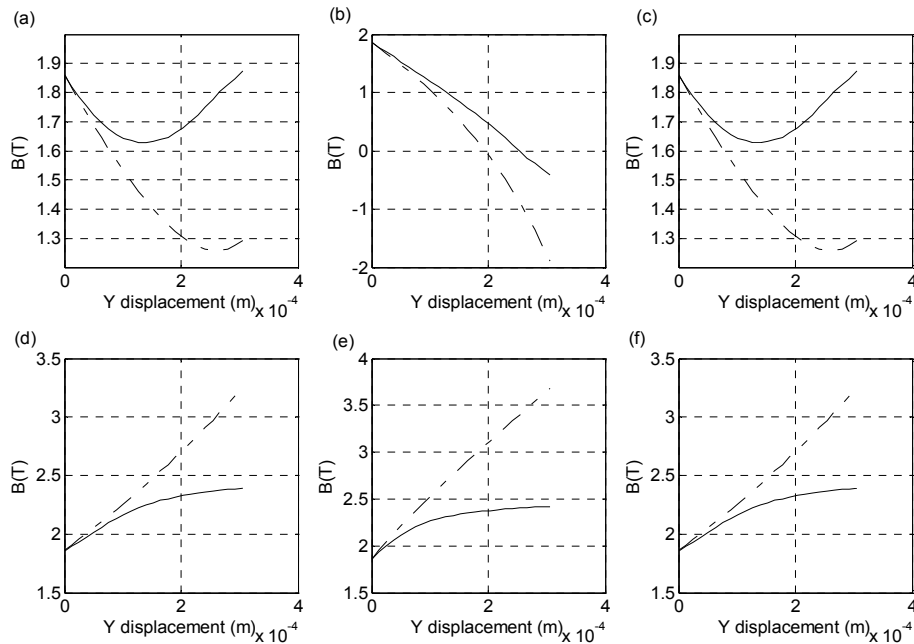
Fig. 3.12 Flux density vs. Y journal position with $G_p = 96$. Key: —, with flux saturation; - -, without flux saturation. (a) pole 1, (b) pole 2, (c) pole 3, (d) pole 4, (e) pole 5, and (f) pole
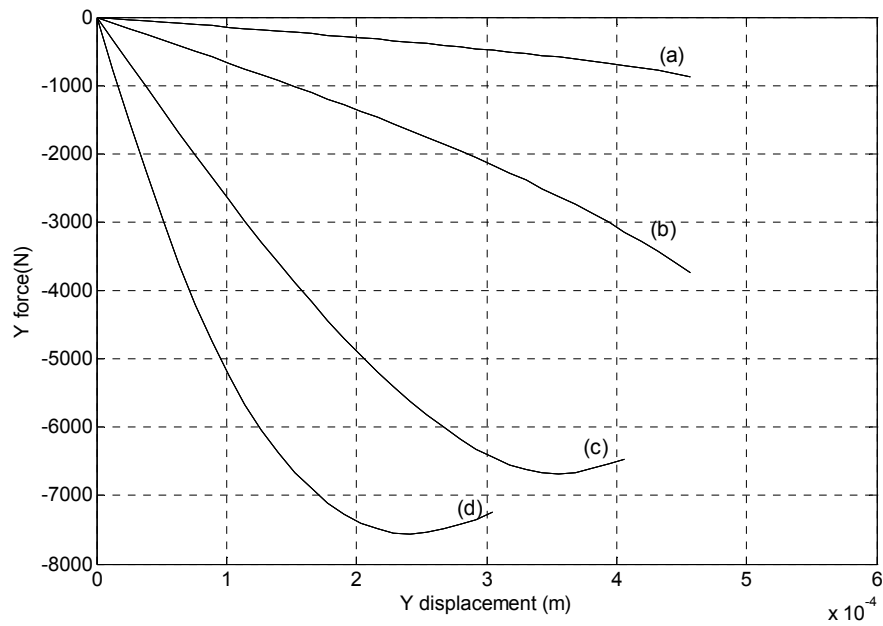
Fig. 3.13 Y direction force vs. Y displacement with flux saturation for different proportional gains. (a) 33.68, (b) 39, (c) 60.39, (d) 96
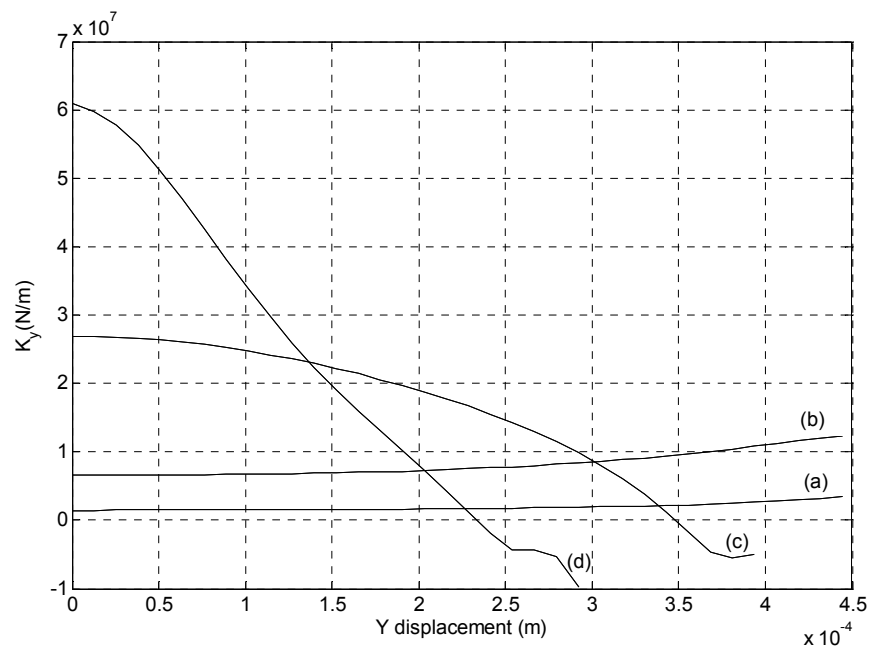
Fig. 3.14 Y direction bearing stiffness coefficient with flux saturation for different proportional gains. (a) 33.68, (b) 39, (c) 60.39, (d) 96

3.4 Static load capacity of PMB HoMB with flux saturation

Maximum static load capacity of PMB HoMB was measured through numerically integrated solutions. Each static force can be balanced by the forces from PMB HoMB and the static forces increase until the magnetic forces cannot hold them. The steady state deflection gets smaller with the increase in the proportional gain value, as shown in Fig. 3.15 and Fig. 3.16. A larger value of lag compensator ratio reduces static deflection at steady state.

With the same static force applied, the magnetic forces that should compensate it are the same regardless of the proportional gain or lag compensator ratio. Thus, the magnetic fluxes generated in each pole are almost the same, given the static force. This is shown in Fig. 3.17. The currents that are needed to produce the required fluxes at the steady state deflection (which results in the air gap) are plotted in Fig. 3.18.
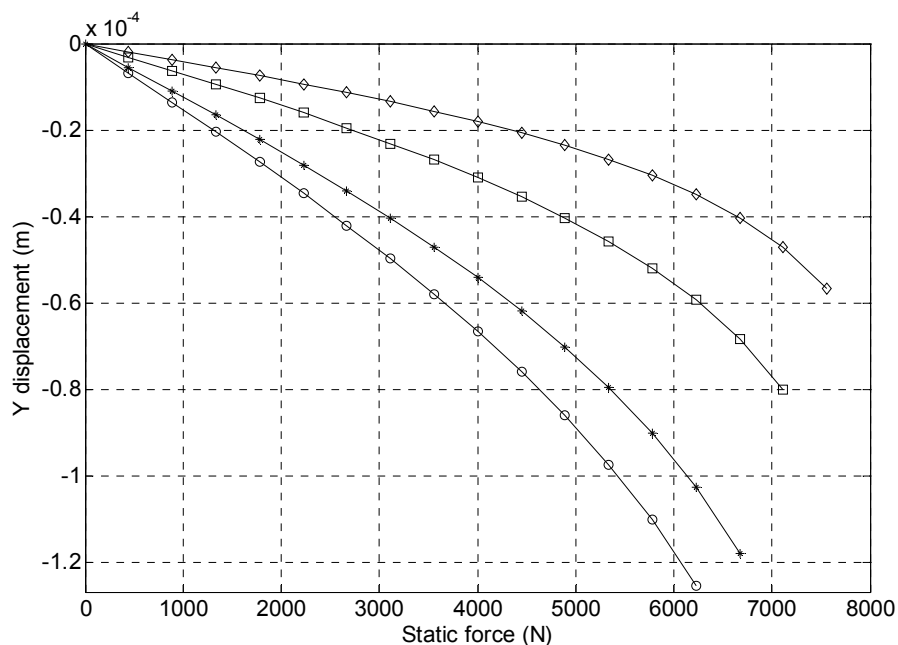
Fig. 3.15 Static force vs. Y displacement plot. z/p=3. Key: o, G_p=33.68; *, G_p=39.02; □, G_p=60.39; ◊, G_p=96.01
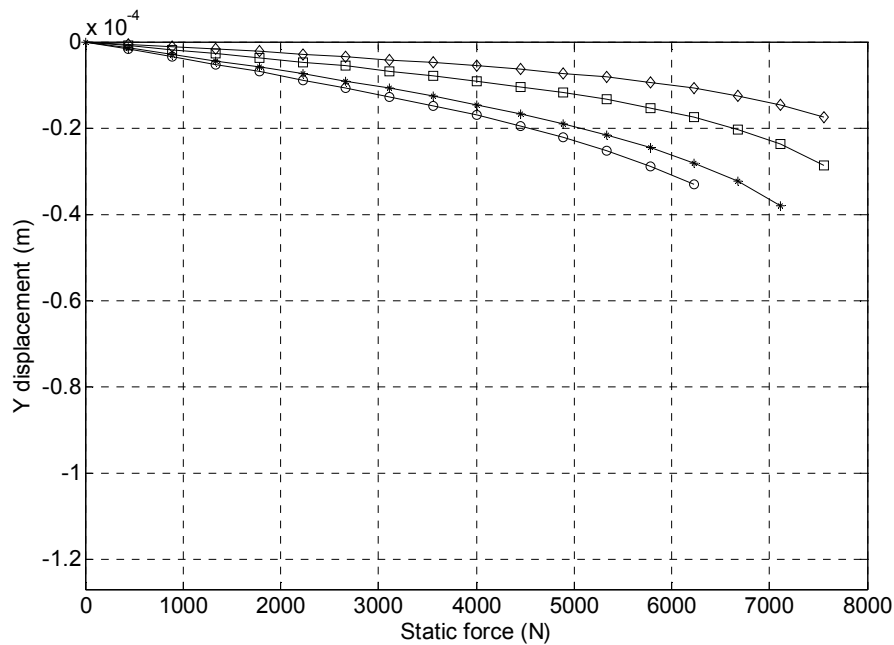
Fig. 3.16 Static force vs. Y displacement plot. z/p=9. Key: o, G_p=33.68; *, G_p=39.02; □, G_p=60.39; ◊, G_p=96.01

Usually, the B-H curve is modeled with a simple linear line that varies until the flux density of 2 Tesla. Based on this and the flux density in the pole 2, the forces from the flux saturation model in this research may predict 3 times more than those from the simple linear line B-H curve model.

The benefits of moving the control target point to where the forces only from the bias flux can hold the static forces are well shown in Fig. 3.19 and Fig. 3.20. At the control target point (X, Y) = (0, 2.032x10^{-4})m, the control current at pole 2 is almost zero with the static force at steady state, because all the static force is supported by the force from the bias flux. If a proper control target point is selected according to the static force, the control currents that are needed for supporting it can be minimized.
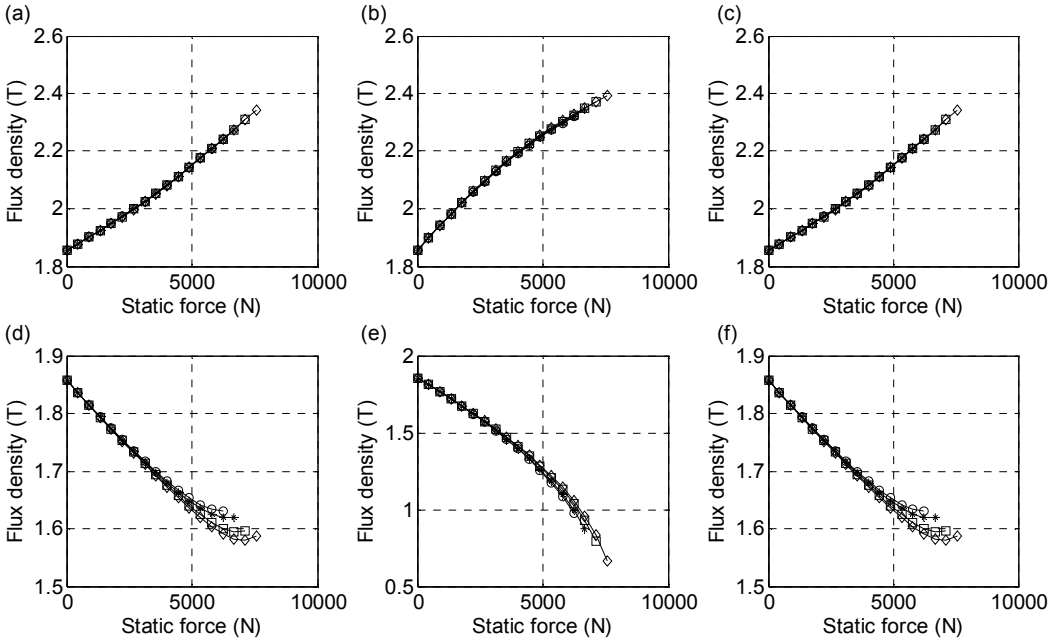
Fig. 3.17 Static force vs. flux density plot. z/p=3. Key: o, G_p=33.68; *, G_p=39.02; □, G_p=60.39; ◊, G_p=96.01. (a) pole 1, (b) pole 2, (c) pole 3, (d) pole 4, (e) pole 5, and (f) pole 6
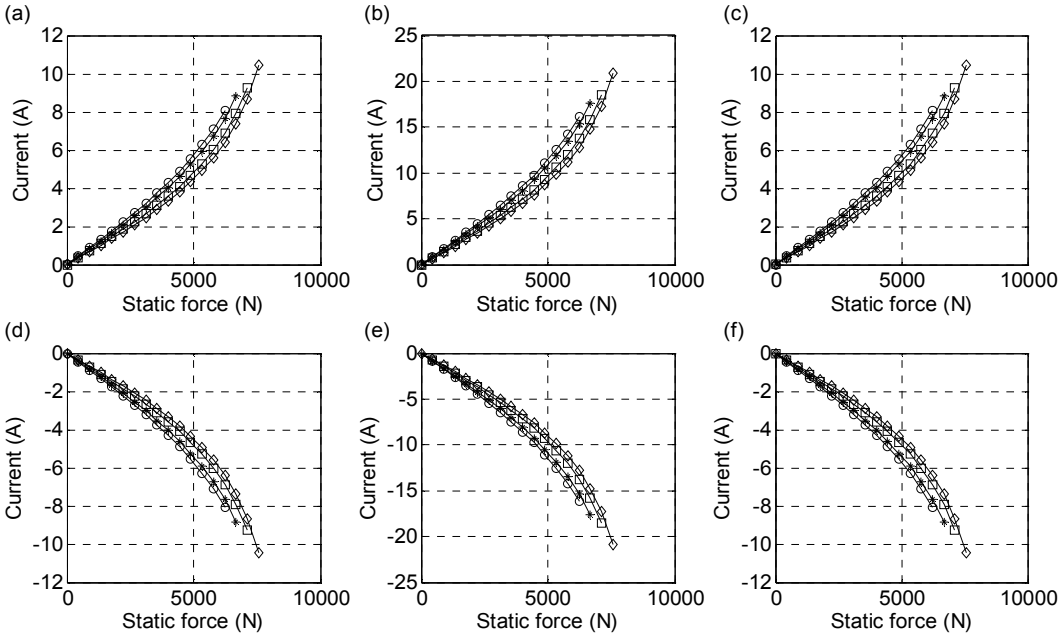
Fig. 3.18 Static force vs. current plot. z/p=3. Key: o, G_p=33.68; *, G_p=39.02; □, G_p=60.39; ◊, G_p=96.01. (a) pole 1, (b) pole 2, (c) pole 3, (d) pole 4, (e) pole 5, and (f) pole 6
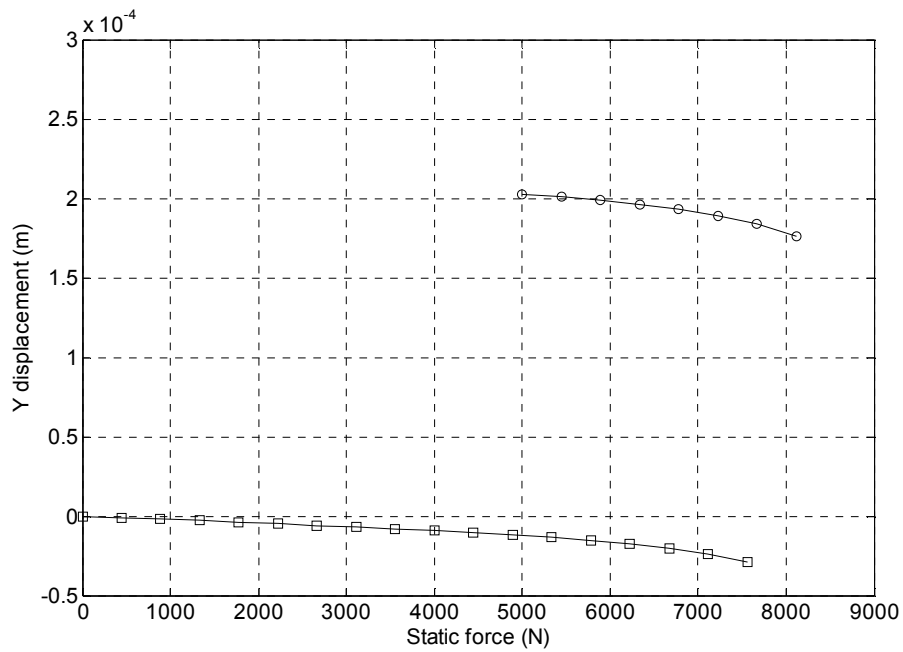
Fig. 3.19 Static force vs. Y displacement plot. z/p=9. G_p=60.39. Key: □, control target Y=0m; o, control target Y=2.032x10^{-4}m
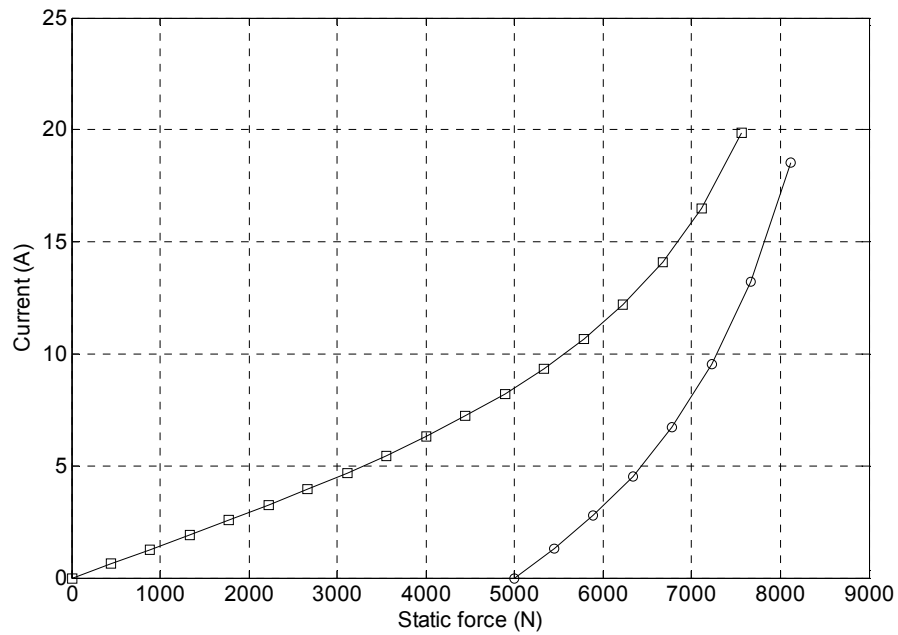
Fig. 3.20 Static force vs. current plot (pole2). z/p=9. G_p=60.39. Key: □, control target Y=0m; o, control target Y=2.032x10^{-4}m

CHAPTER IV

RIGID ROTOR AND FLUX SATURATION

The effects of flux saturation on nonlinear characteristics in response are identified utilizing frequency response plots, bifurcation diagrams, and Poincaré maps. The responses of two-dof rotor supported by PMB HoMBs with flux saturation are investigated in closed loop employing PD controller.

4.1 Natural frequencies of linearized close loop system

Nonlinear force relationship to the instantaneous air gap and amplifier output current, along with flux saturation in the material and without it, is numerically linearized at the control target point to find out the natural frequencies of closed loop with 2-dof rotor model.

Transfer function from input error to X and Y control voltage, as shown in Fig. 4.1, can be expressed as

$$
\begin{aligned}
\frac{V_{k,control}}{V_{k,error}} &= G_d s + G_p, \\
V_{k,error} &= V_{k,ref} - G_s k, \\
(k &= x, y),
\end{aligned}
\tag{17}
$$

where G_d is the derivative gain, G_p is the proportional gain, $V_{k,ref}$ is the reference voltage (V) depending on the control target position, and G_s is the sensor gain with the value of 1969V/m.

Converting the transfer function of Eq. (17) into the differential equation form with respect to time becomes
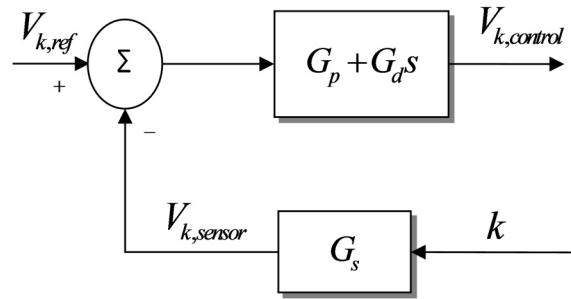
Fig. 4.1   Partial control loop from input error voltage to output control voltage

$$V_{k,control} = G_d \dot{V}_{k,error} + G_p V_{k,error}. \tag{18}$$

The schematic of signal path between the output voltage from the controller and the input forces to the rotor is expressed in Fig. 4.2. Algebraic nonlinear (NL) Eq. (7) is solved at each time step and at static condition PA can be just expressed as its DC gain, 1A/V. This nonlinear relation can be linearized into Equations
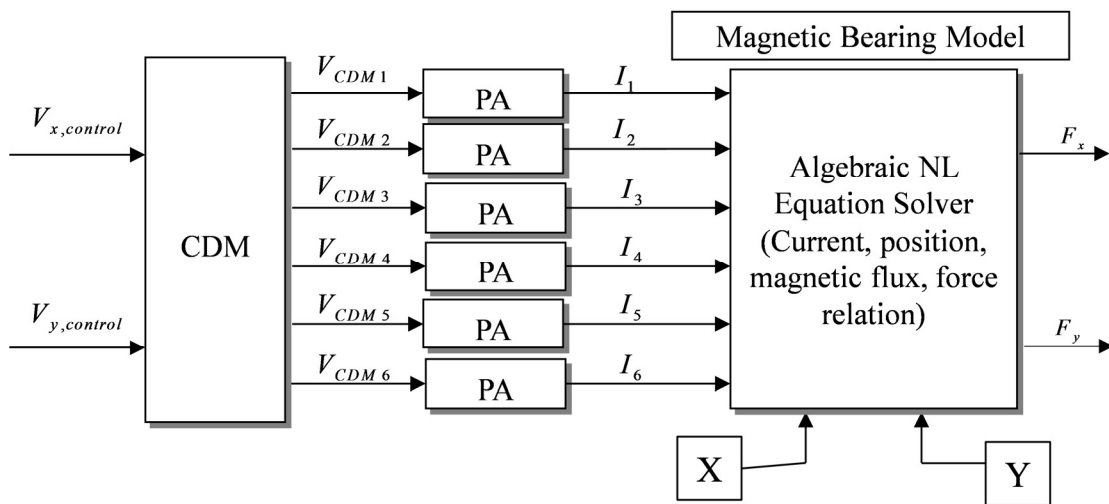
Fig. 4.2   Partial control loop from control voltage to X and Y forces

$$F_{x,m} = K_{x,p}x_b + K_{x,v}V_{x,control},$$
$$F_{y,m} = K_{y,p}y_b + K_{y,v}V_{y,control},$$

(19)

where $K_{x,p}, K_{y,p}$ are the position stiffness (N/m) in X and Y directions and $K_{x,v}, K_{y,v}$ are

the voltage stiffness (N/V) in X and Y directions at the point of interest.

Fig. 4.3 shows the Y direction force calculated from Eqs. (7) and (9) without X

control current and material saturation when the shaft moves in Y direction from the

center of bearing. Y voltage axis implies that Y control voltage is applied while Y

position is fixed at each step. Fig. 4.4 is plotted with the same way including the

proposed flux saturation model.
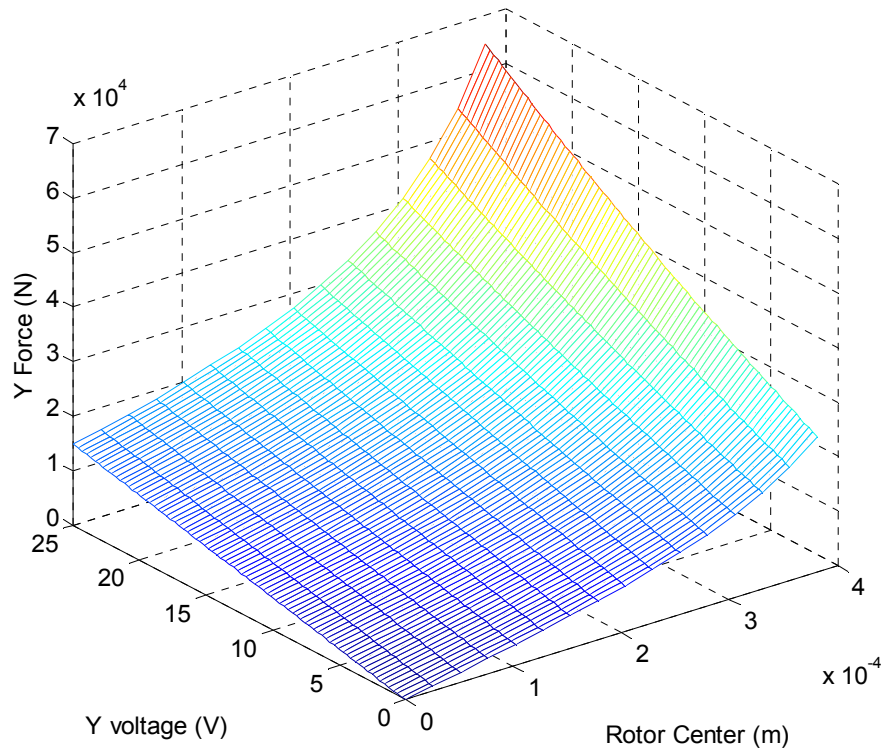
Fig. 4.3   Y force vs. shaft Y position vs. controller Y output voltage at each shaft Y
position when flux saturation model is excluded
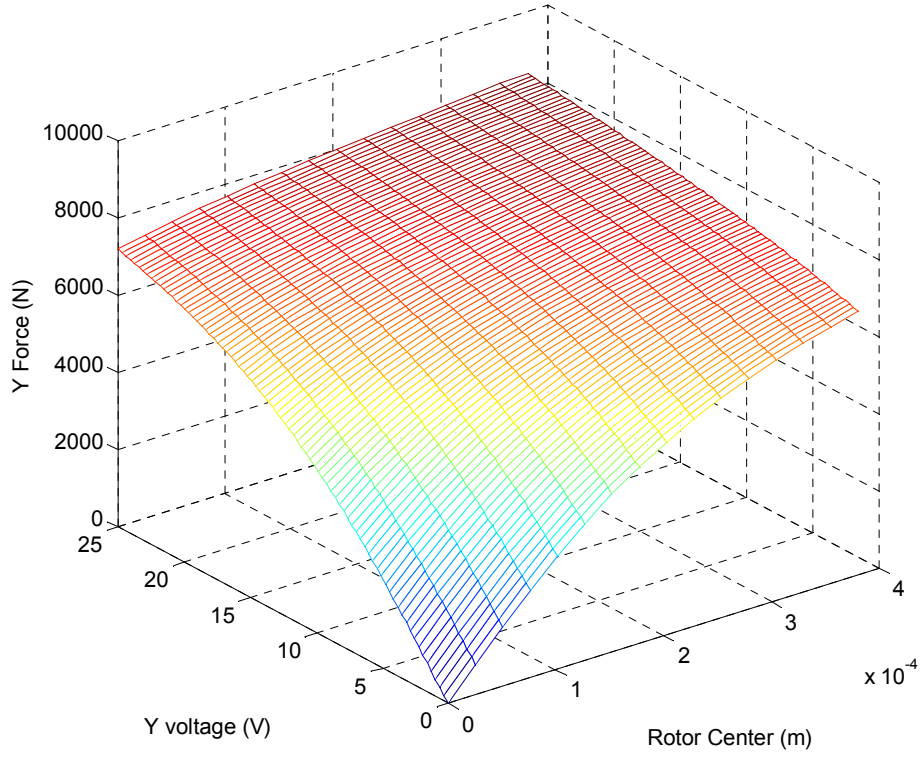
Fig. 4.4 Y force vs. shaft Y position vs. controller Y output voltage at each shaft Y
position when flux saturation model is included

From Fig. 4.3 and Fig. 4.4, the position and voltage stiffness can be calculated

numerically. For example, if the control target point is set at $(x, y(j)) = (0, 1.016 \times 10^{-4})$

m , taking finite difference of the values of Y force, Y control voltage, and Y

displacement,

$$K_{y,p} = \frac{\partial F_{y,m}}{\partial y} = \left. \frac{F_{y,m}(j+1) - F_{y,m}(j)}{y(j+1) - y(j)} \right|_{\substack{V_{x,control}=0 \\ V_{y,control}=0}}, \tag{20}$$

$$K_{y,v} = \frac{\partial F_{y,m}}{\partial V_{y,control}} = \left. \frac{F_{y,m}(q+1) - F_{y,m}(q)}{V_{y,control}(q+1) - V_{y,control}(q)} \right|_{\substack{x=0 \\ y=y(j)}}, \tag{21}$$

where $y(j)$ is the control target point, $y(j+1) - y(j) = 1.27 \times 10^{-5}$ m , j=1,...,n (total

displacement steps), and q=1,…,m (total voltage steps). The position and voltage

stiffness in X direction can be derived similarly. These values that are numerically found

by Eqs. (20) and (21) are described in Table 4.1 when the flux saturation model is not

considered. Table 4.2 shows the values when the flux saturation model is taken into

account. The position and voltage stiffness in X and Y directions are assumed to be the

same.

The natural frequencies of linearized closed loop system with the flux saturation

model and without it can be derived from Eqs. (10), (18), and (19).

$$
\begin{aligned}
K_{equ} &= K_v G_p G_s - K_p, \\
C_{equ} &= K_v G_d G_s, \\
\omega_n &= \sqrt{\frac{K_{equ}}{M_b}}, \\
\varsigma &= \frac{C_{equ}}{2M_b \omega_n},
\end{aligned}
\tag{22}
$$

where K_{equ} and C_{equ} are the equivalent stiffness and damping of the linearized closed

loop, ω_n and ς are the natural frequency and damping ratio of the linearized closed loop.

Table 4.1   Numerically calculated position stiffness and voltage stiffness at a target position (X, Y) when flux saturation model is excluded

(X, Y) (m)	K_p (N/m)	K_v (N/V)
$(0, 1.02 \times 10^{-4})$	4.04×10^{7}	613

Table 4.2 Numerically calculated position stiffness and voltage stiffness at a target position (X, Y) when flux saturation model is included

(X, Y) (m)	K_p (N/m)	K_v (N/V)
$(0, 1.02 \times 10^{-4})$	2.53×10^7	394

4.2 Nonlinear frequency response

The frequency response plot of a rigid rotor in a PMB HOMB is studied with the static load applied in negative Y direction. The case without flux saturation model is compared with the case with the proposed flux saturation model. The air gap fluxes are weakened by the inclusion of material path flux saturation leading to a loss of load capacity for counteracting the applied static load with the permanent magnet bias flux. The target (reference) position could be adjusted to compensate for this or the static load could be decreased to maintain the same target position in the Y direction. The latter approach was employed with a reduction of static applied load from a value of 3903.8 N to a value of 2939.6 N to keep the control target position at $(X, Y) = (0, 1.016 \times 10^{-4})$ m.

Only PD controllers are included in the close loop and proportional gain (G_P) and derivative gain (G_d) of the controller are the same in x and y direction, $G_p = 97.07$, $G_d = 0.0076$. LCs and LPFs are excluded. PAs are simplified as having only DC gains, 1A/V. The Eq. (10) is numerically integrated using the fourth-order Runge-Kutta method and at each time step, the X and Y force are numerically calculated from the Eqs. (7) and (9), given the instantaneous currents in the 6 poles and the X and Y journal coordinates. The Levenberg-Marquardt algorithm[24] is used to solve the set of nonlinear algebraic Eq.

(7), given the solution for the fluxes from the previous time step are used as initial guesses of their values for the present step.

Amplitude at each spin speed is defined as the absolute distance value from the control target point to the point where the steady state shaft response returns at each period of time (periodic solution).

With G_p = 97.07, the bearing has softening spring characteristics as shown inFig. 3.13, and Fig. 4.5 shows this feature clearly. Fig. 4.5 plots the frequency response for both increasing and decreasing spin speed when the flux saturation model is considered. For increasing speed at 13600 rpm, there is sudden amplitude increase and the jump in a
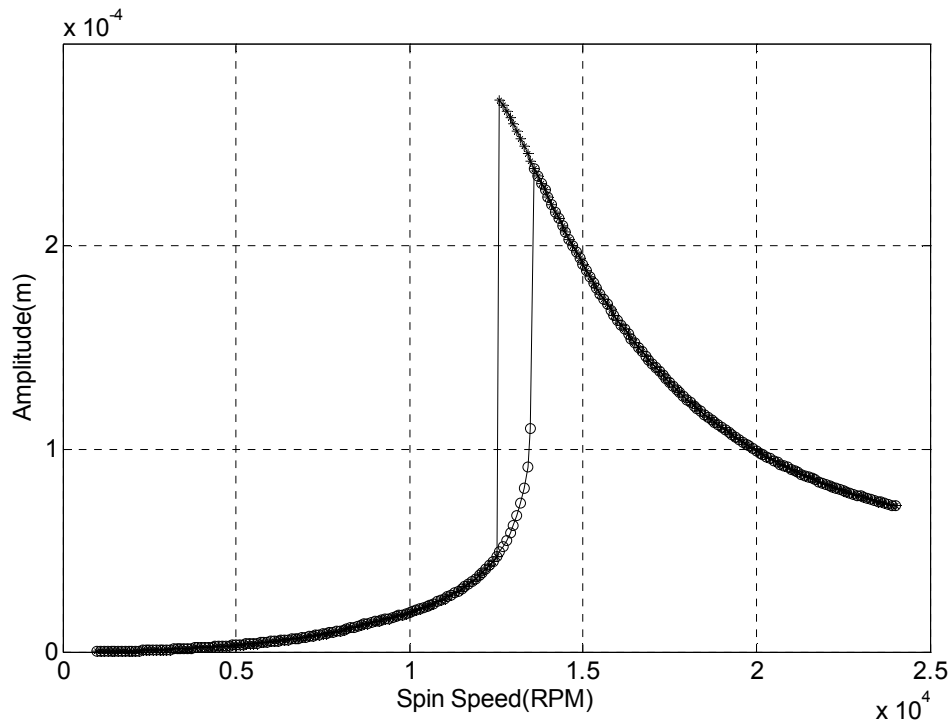
Fig. 4.5   Amplitude vs. spin speed plot. G_p=97.07, G_d=0.0076, e=3.8x10^{-5}m. Flux saturation model is included. Key: o, increasing; *, decreasing

downward direction occurs at 12500 rpm for decreasing speed. The hysteresis region forms for speeds between 12500 rpm and 13600 rpm, where stable responses are difference depending on the increasing or decreasing spin speed, i.e., two stable solutions exist depending on which initial condition is selected.

The jump and hysteresis result in Fig. 4.5 makes it clear that the analysis including the flux saturation model is more appropriate to predict the nonlinear system characteristics. For Comparison, the frequency response plot without the flux saturation model, shown in Fig. 4.6, does not indicate any jump or hysteresis region. The orbit plots in Fig. 4.7 and Fig. 4.8 shows two stable period-1 responses at the same spin speed,
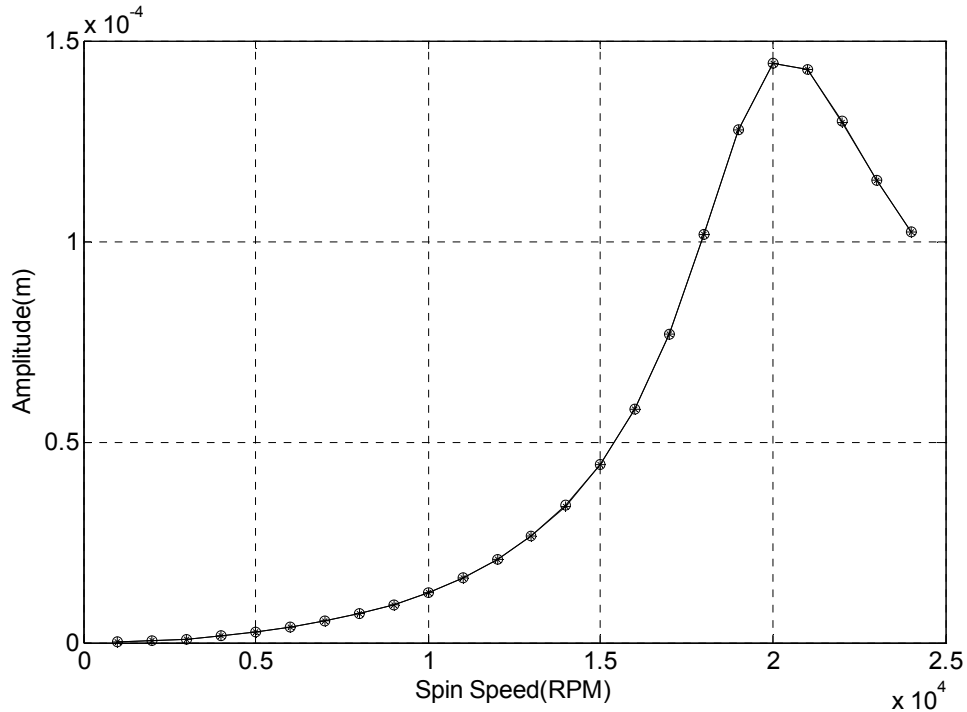
Fig. 4.6   Amplitude vs. spin speed plot. G_p=97.07, G_d=0.0076, e=3.8x10^{-5}m. Flux saturation model is not included. Key: o, increasing; *, decreasing

13000 rpm. Fig. 4.7 is for increasing speed and Fig. 4.8 is for decreasing speed. The '+' mark indicates the control target point and 'o', the returning point at each time period.

The flux density variation at each air gap with decreasing speed at 13000 rpm is plotted in Fig. 4.9, Fig. 4.10, and Fig. 4.11 with the horizontal axis as time, X displacement, and Y displacement respectively. Because of the large amplitude response generated by the unbalance force, all the flux densities at air gaps swing from 0 to 2.4 Tesla which is the maximum value of flux density in the flux saturation model.

The forces in X and Y direction exerted by the magnetic poles on the shaft are obtained while the reluctances of air gap and pole material and flux saturation are taken into account. The X and Y forces with decreasing speed at 13000 rpm are plotted in Fig. 4.12, Fig. 4.13, and Fig. 4.14 with the horizontal axis as time, X displacement, and Y displacement, respectively. Nonlinear force characteristics due to the flux saturation are clearly shown in these figures.

Fig. 4.7   Orbit plot at 13000 rpm when spin speed increases. G_p=97.07, G_d=0.0076, e=3.8x10^{-5}m. Flux saturation model is included.

Fig. 4.8   Orbit plot at 13000 rpm when spin speed decreases. G_p=97.07, G_d=0.0076, e=3.8x10^{-5}m. Flux saturation model is included.
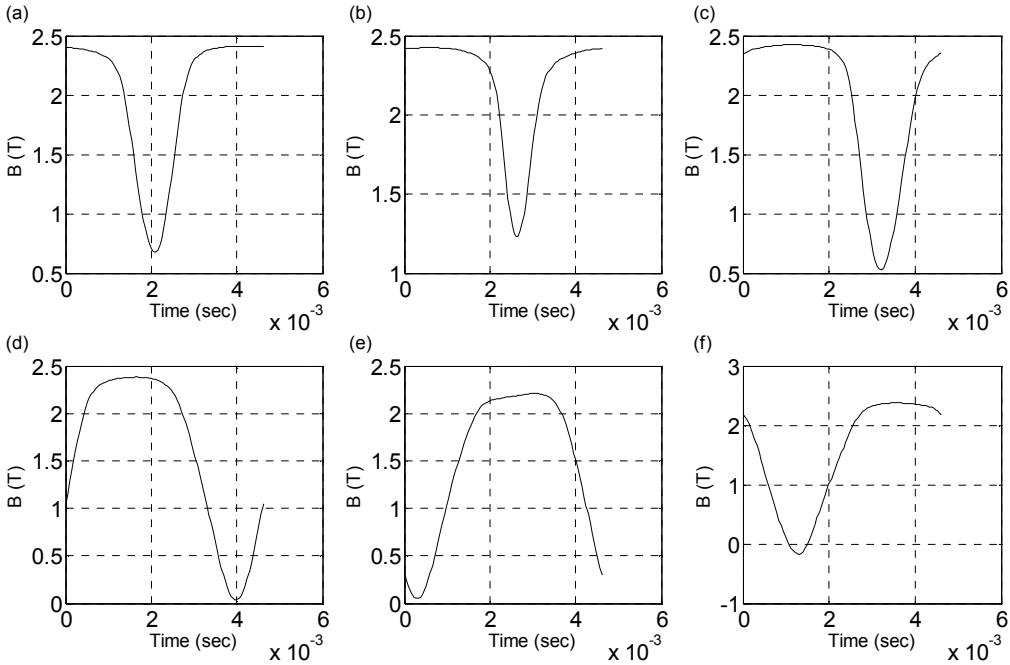
Fig. 4.9   Flux density at each air gap vs. time at 13000 rpm when spin speed
decreases. G_p=97.07, G_d=0.0076, e=3.8x10^{-5}m. Flux saturation model is
included. (a) pole 1, (b) pole 2, (c) pole 3, (d) pole 4, (e) pole 5, (f) pole 6
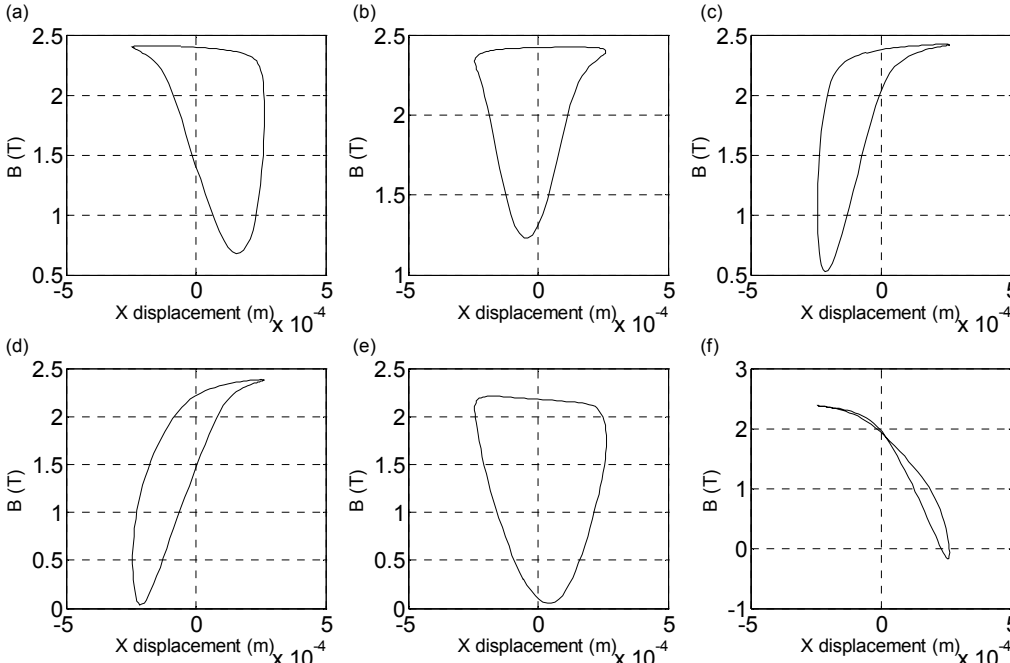
Fig. 4.10 Flux density at each air gap vs. X displacement at 13000 rpm when spin
speed decreases. G_p=97.07, G_d=0.0076, e=3.8x10^{-5}m. Flux saturation
model is included. (a) pole 1, (b) pole 2, (c) pole 3, (d) pole 4, (e) pole 5,
(f) pole 6
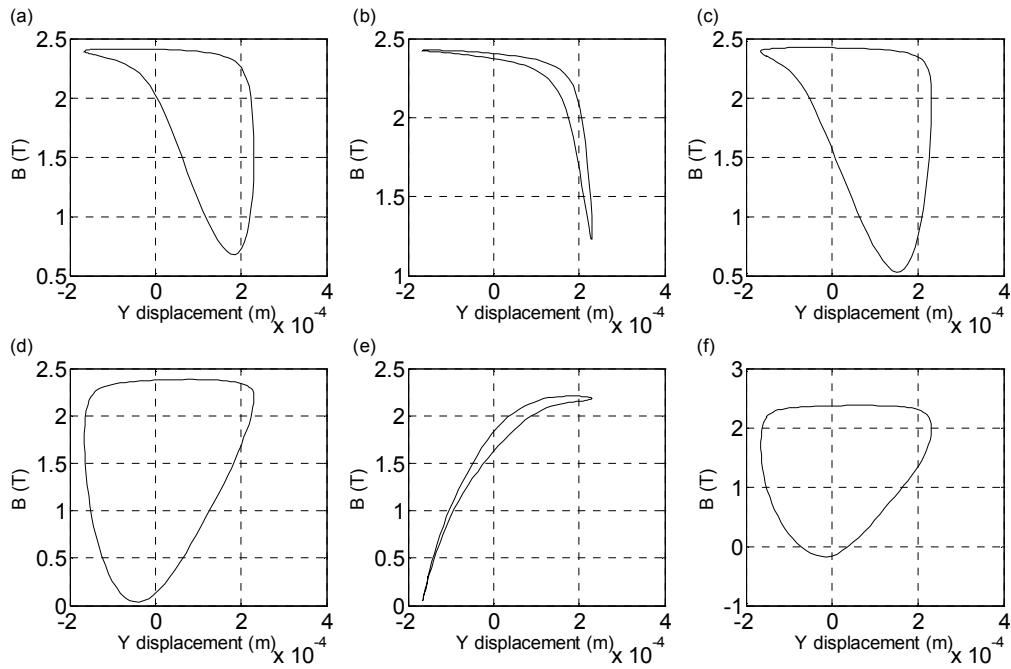
Fig. 4.11 Flux density at each air gap vs. Y displacement at 13000 rpm when spin speed decreases. G_p=97.07, G_d=0.0076, e=3.8x10^{-5}m. Flux saturation model is included. (a) pole 1, (b) pole 2, (c) pole 3, (d) pole 4, (e) pole 5, (f) pole 6
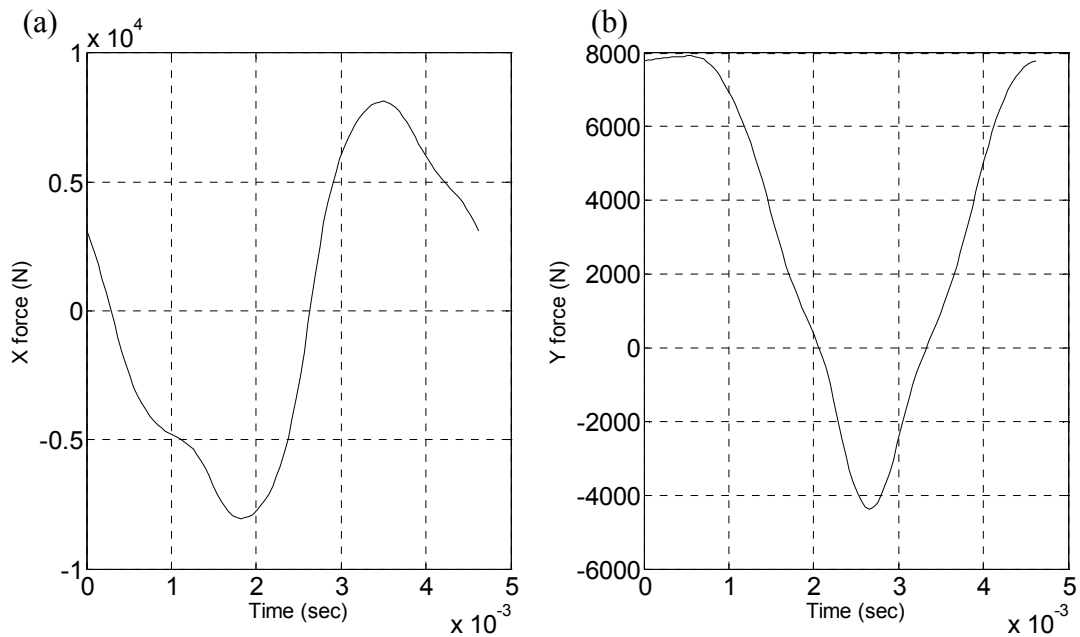
Fig. 4.12 Force vs. time at 13000 rpm when spin speed decreases. G_p=97.07, G_d=0.0076, e=3.8x10^{-5}m. Flux saturation model is included. (a) X force, (b) Y force
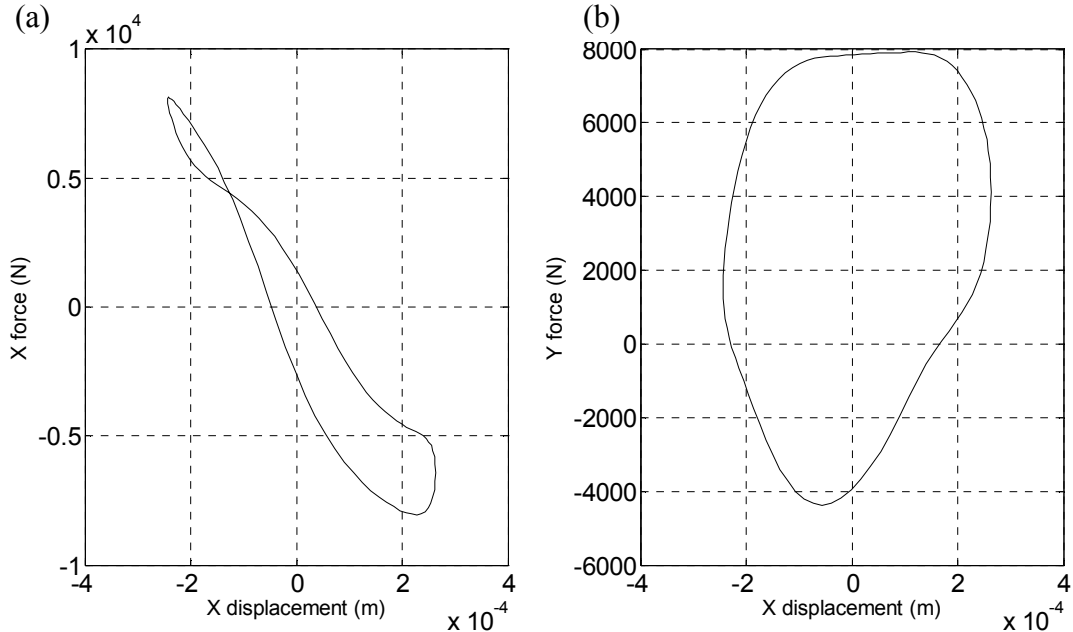
Fig. 4.13 Force vs. X displacement at 13000 rpm when spin speed decreases. G_p=97.07, G_d=0.0076, e=3.8x10^{-5}m. Flux saturation model is included. (a) X force, (b) Y force
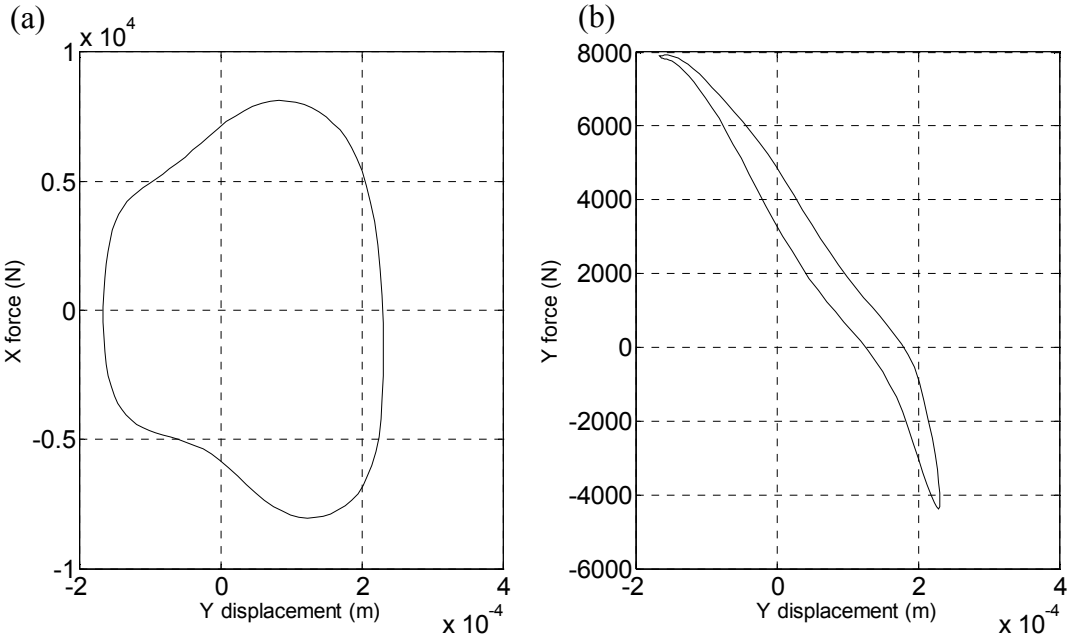
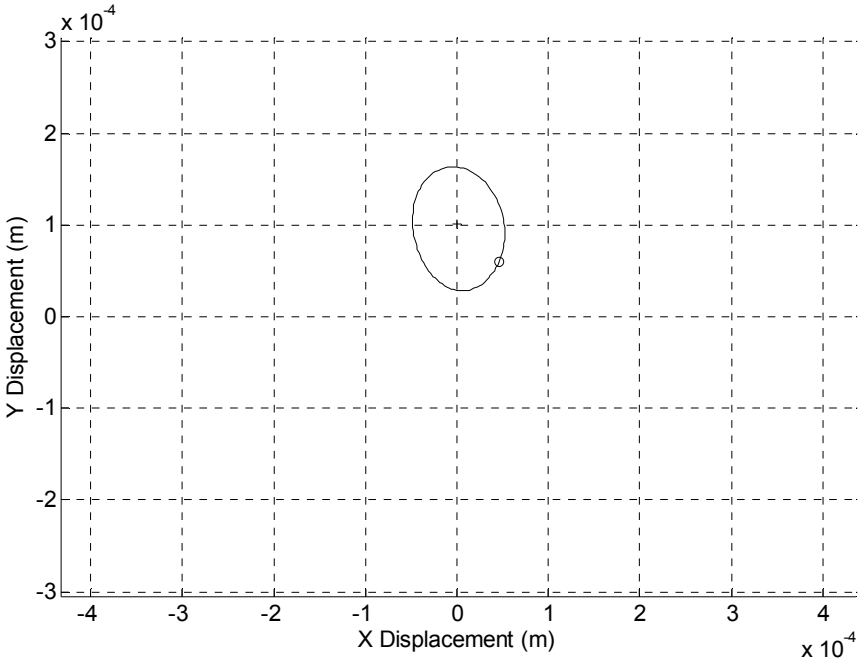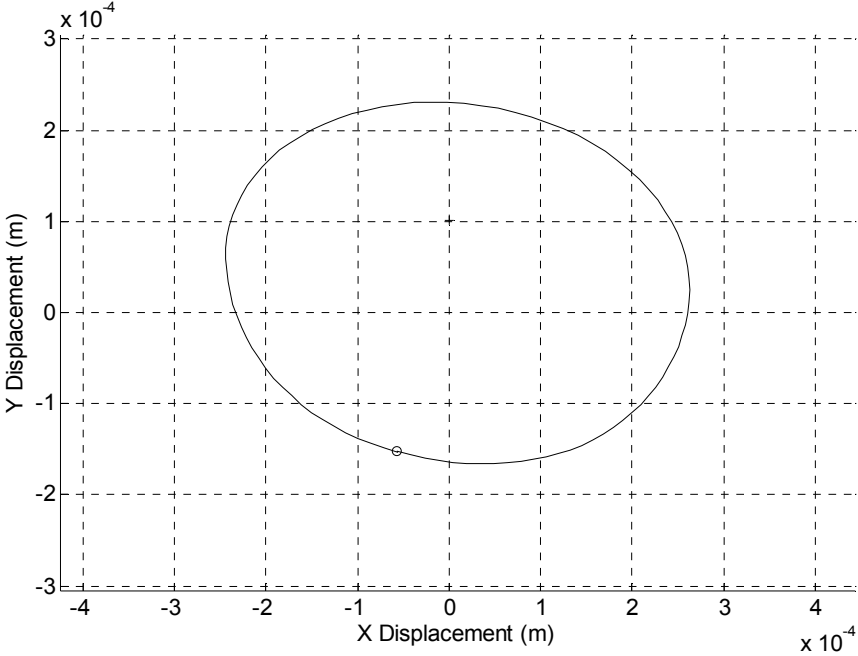Fig. 4.14 Force vs. Y displacement at 13000 rpm when spin speed decreases. G_p=97.07, G_d=0.0076, e=3.8x10^{-5}m. Flux saturation model is included. (a) X force, (b) Y force

## 4.3   Bifurcation diagram

The subharmonic motion can be observed using Poincaré maps and bifurcation diagram. A simple Poincaré map can be obtained by sampling the rotor response once every rotor forcing period of time. A Poincaré map with n discrete points represents a 'period-n' response, for which the lowest frequency is 1/n times the rotor spin speed.

A bifurcation diagram provides the qualitative response behavior when a parameter of the system is varied. Poincaré points are plotted in the bifurcation diagram for certain range of the parameter such as mass unbalance eccentricity, e.

For both bifurcation diagram and Poincaré map in this section, the control target point is set at $(X, Y) = (0, 1.016x10^{-4})$ m to compensate the static load 2939.6 N with the force generated from the bias flux. The shaft spin speed is chosen at 13000 rpm. The proportional gain G_p of 97.07 and derivative gain G_d of 0.0076 are selected for the analysis in this section, i.e., the same as in SECTION 4.2.

Fig. 4.15 and Fig. 4.16 show the X and Y bifurcation diagrams when the unbalance eccentricity is selected as a parameter. The tendency of the Poincaré points is similar in X and Y coordinates. The Poincaré points at the 4th quadrant jump to the 3rd quadrant as the unbalance eccentricity increases and are kept as the period-1 response until the unbalance eccentricity approaches $7.5x10^{-5}$ m. After that, the Poincaré points bifurcate into the period-2 response, as shown in Fig. 4.17 and Fig. 4.18 in detail.

Fig. 4.19 and Fig. 4.20 show a zoomed view for Fig. 4.17 and Fig. 4.18 in the range from $7.811x10^{-5}$ m to $7.885x10^{-5}$ m. This reveals clearly the period doubling path to chaos. This plot was constructed with 60 steps of the unbalance eccentricities and 100

forcing periods per each e value are plotted after a delay period of 100 cycles. When the unbalance eccentricity passes 7.83×10^{-5} m, the Poincaré points become quasi-periodic and the number of periods keeps increasing. Chaos occurs in the band where the dots seem to be merged at random. Periodic windows within the chaotic bands can be seen as light vertical strips around the unbalance eccentricity 7.87×10^{-5} m. The response was unstable after $e = 7.885 \times 10^{-5}$ m.

Similar result in SECTION 4.2 was obtained when the bearing model does not include the flux saturation effect, i.e., the material reluctance is excluded. The nonlinear characteristics do not appear in the responses and the X and Y Poincaré points with unbalance eccentricity as a parameter does not exhibit any bifurcation, shown in Fig. 4.21 and Fig. 4.22.

The Poincaré points with $e = 7.833 \times 10^{-5}$ m are plotted at Fig. 4.23 and Fig. 4.24 for 500 forcing periods at 13000 rpm. At this unbalance eccentricity step, the period-2 responses, shown at Fig. 4.19, are grown into larger periodic responses, and X Poincaré points indicate two closed curves that can be categorized as quasi-periodic responses. Fig. 4.25 shows the orbit plot with this unbalance eccentricity.

The Poincaré points with $e = 7.885 \times 10^{-5}$ m are plotted at Fig. 4.26 and Fig. 4.27 for 5000 forcing periods at 13000 rpm. This unbalance step was the last before the shaft response became unstable, resulting from the numerical analysis with the flux saturation model. These figures clearly show strange attractors and along with the time response plots for 50 forcing periods at Fig. 4.28, confirm the chaotic behavior of the system. Fig. 4.29 shows the orbit plot with this unbalance eccentricity.
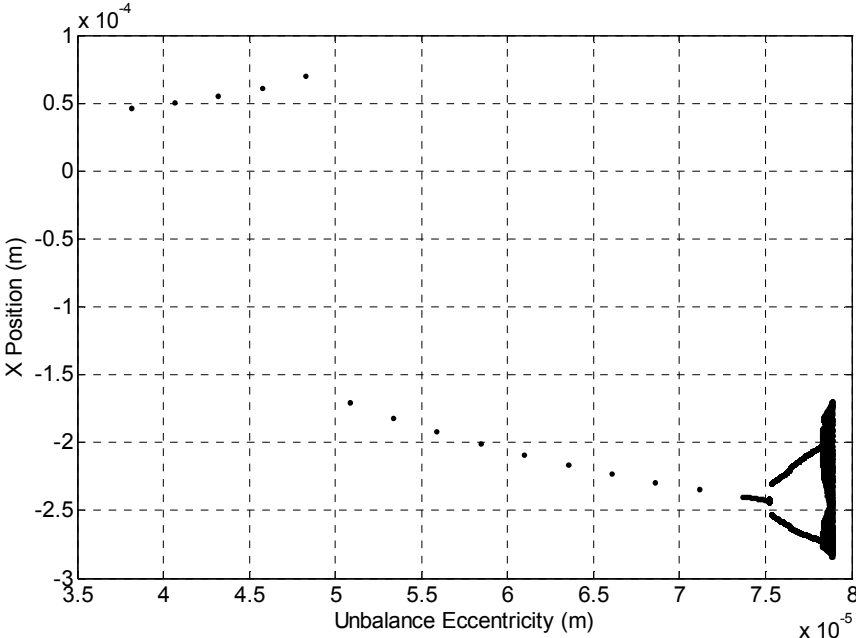
Fig. 4.15 Bifurcation diagram with unbalance eccentricity as a parameter (X response). RPM = 13000
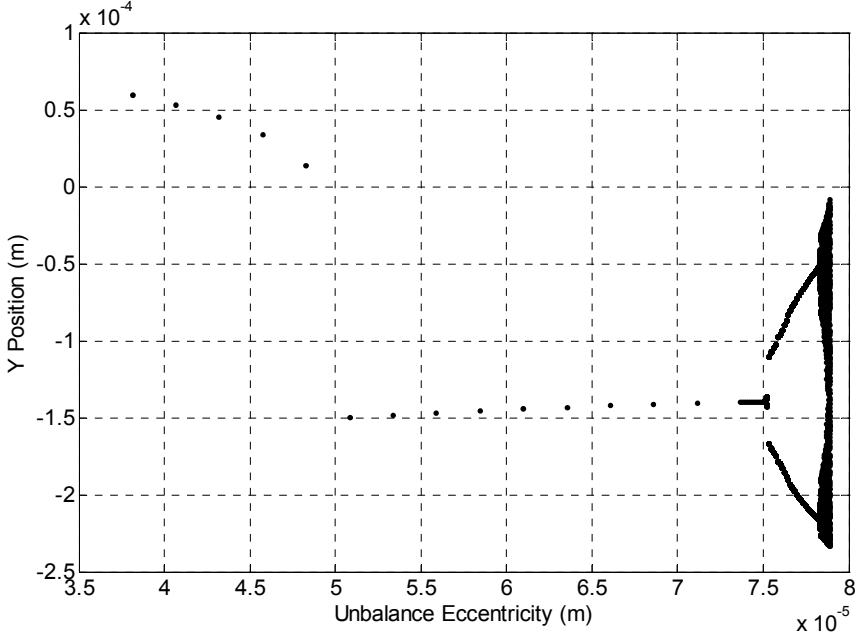
Fig. 4.16 Bifurcation diagram with unbalance eccentricity as a parameter (Y response). RPM = 13000
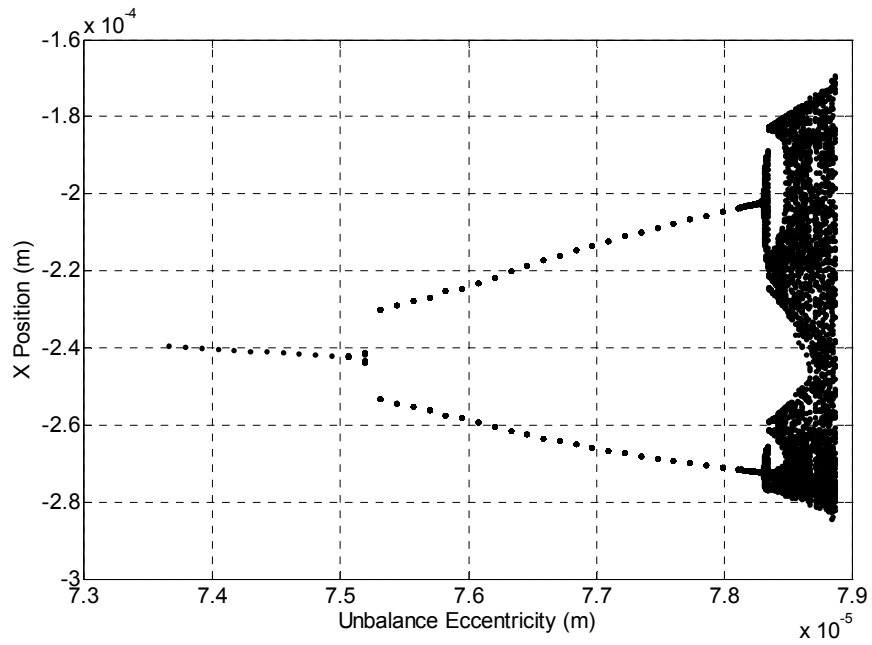
Fig. 4.17 Bifurcation diagram with unbalance eccentricity as a parameter (X response). Magnified region from period-2 to chaotic response
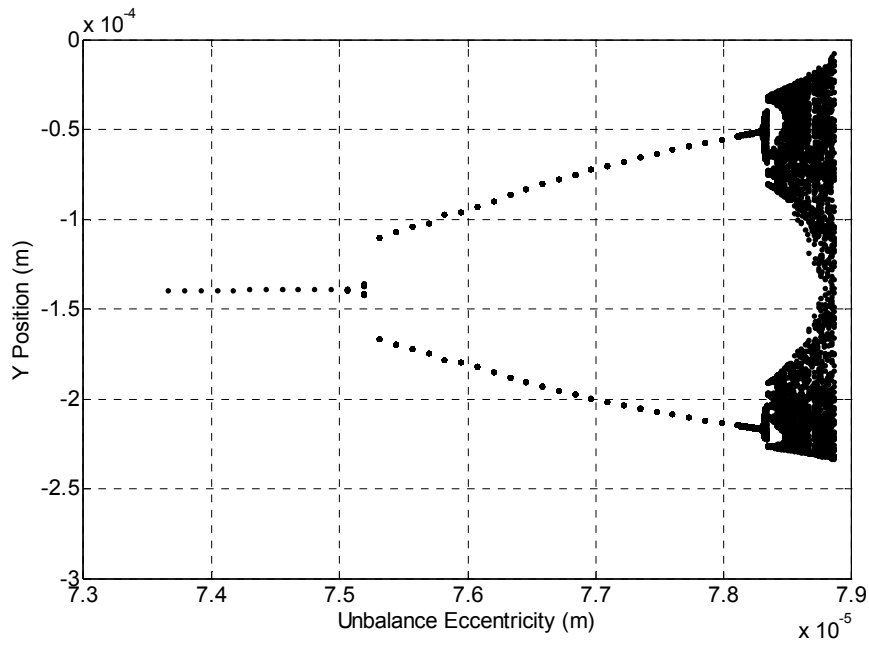
Fig. 4.18 Bifurcation diagram with unbalance eccentricity as a parameter (Y response). Magnified region from period-2 to chaotic response
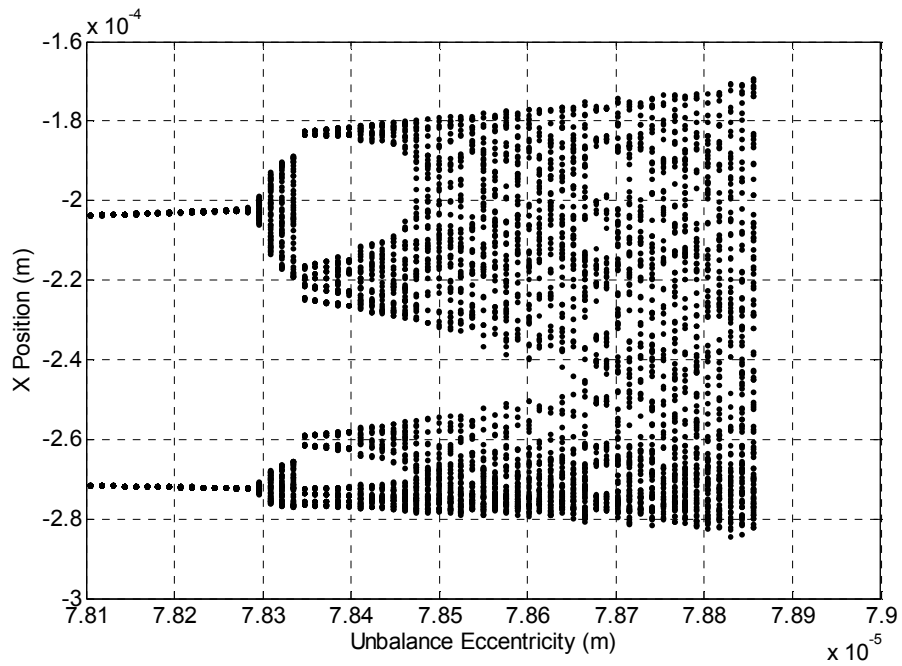
Fig. 4.19 Bifurcation diagram with unbalance eccentricity as a parameter (X response), magnified chaotic response region
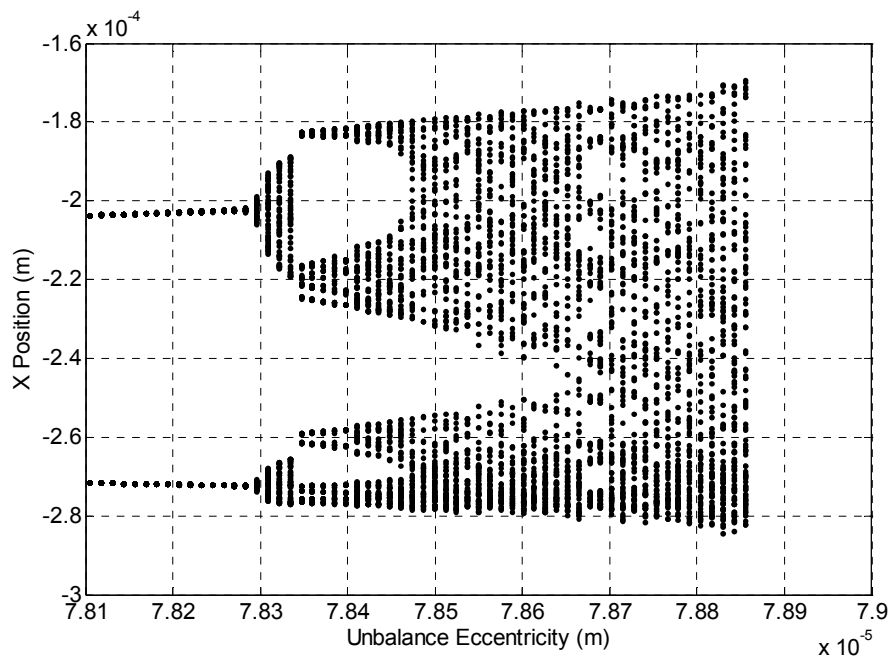
Fig. 4.20 Bifurcation diagram with unbalance eccentricity as a parameter (Y response), magnified chaotic response region
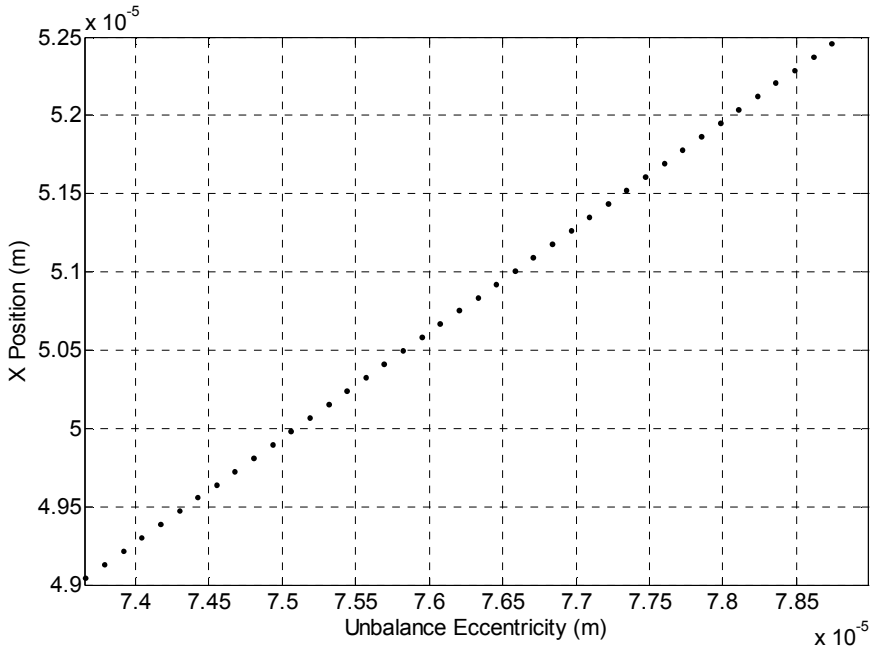
Fig. 4.21 X Poincaré points with unbalance eccentricity as a parameter. Flux saturation model is excluded
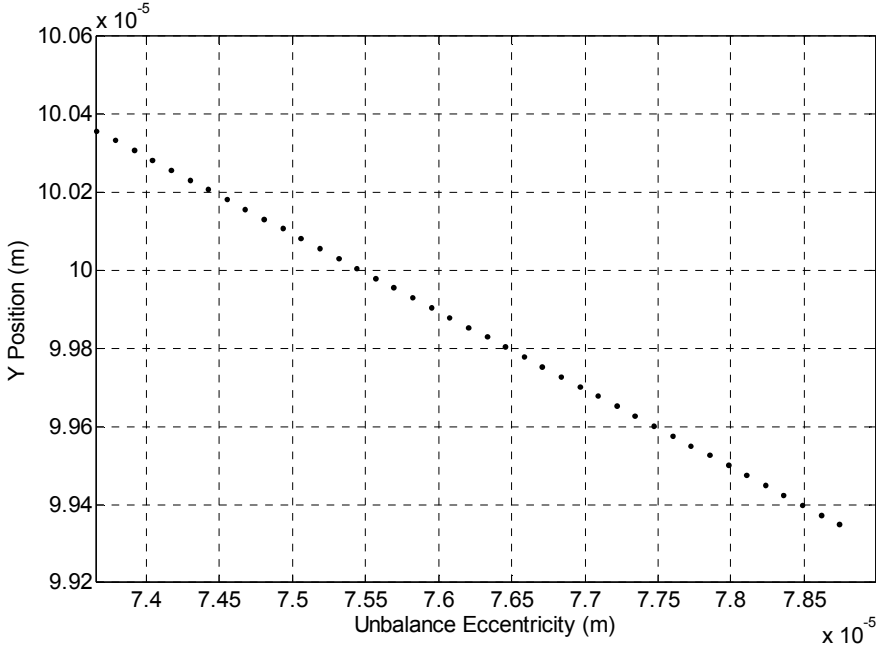
Fig. 4.22 Y Poincaré points with unbalance eccentricity as a parameter Flux saturation model is excluded
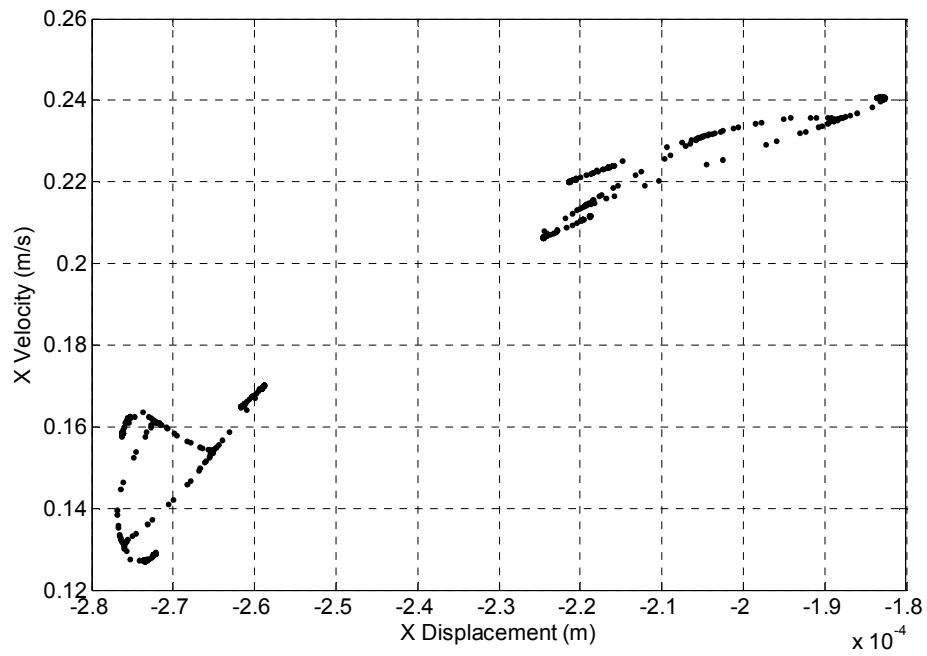
Fig. 4.23 Poincaré plot for X response. e=7.833x10^{-5}, 500 forcing periods at 13000 rpm
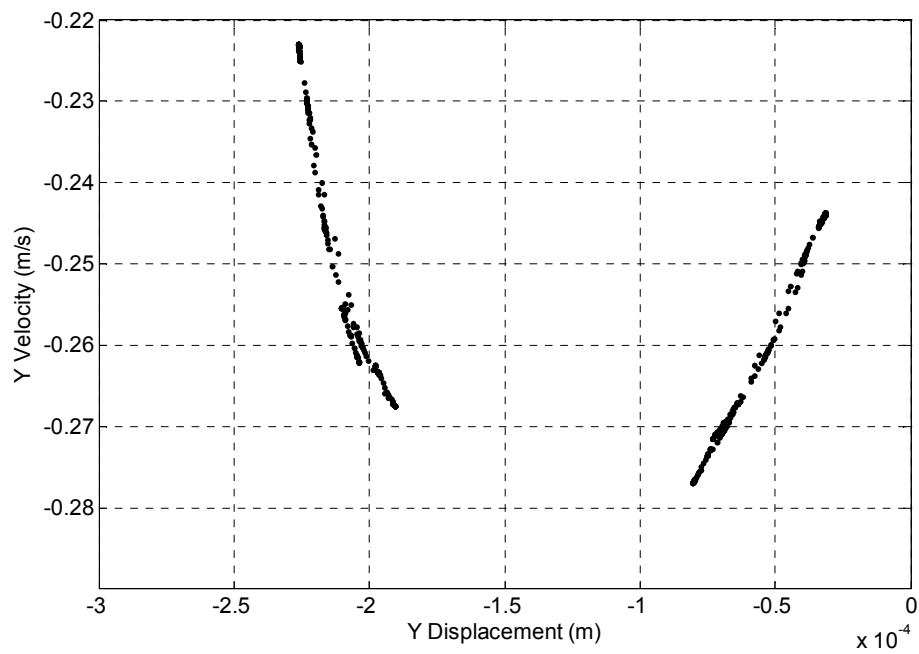
Fig. 4.24 Poincaré plot for Y response. e=7.833x10^{-5}, 500 forcing periods at 13000 rpm
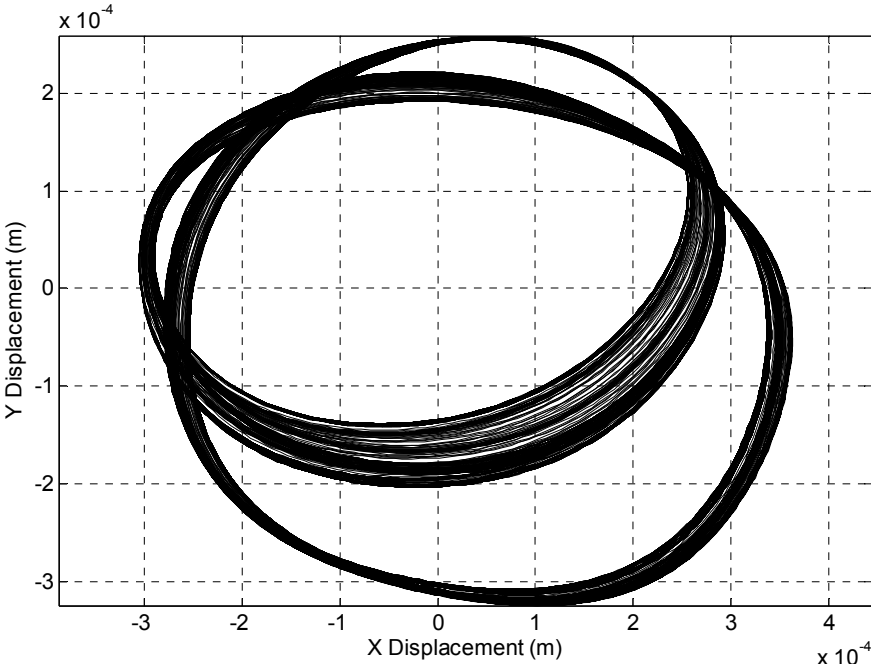
Fig. 4.25 Orbit plot with e=7.833x10^{-5} for 500 forcing periods at 13000 rpm
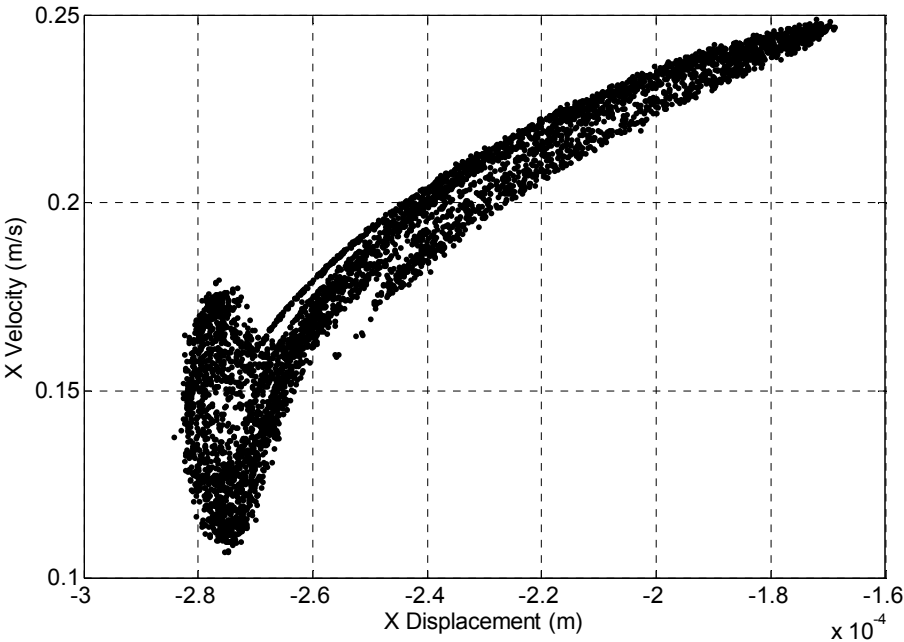
Fig. 4.26 Poincaré plot for X response. e=7.885x10^{-5}, 5000 forcing periods at 13000 rpm
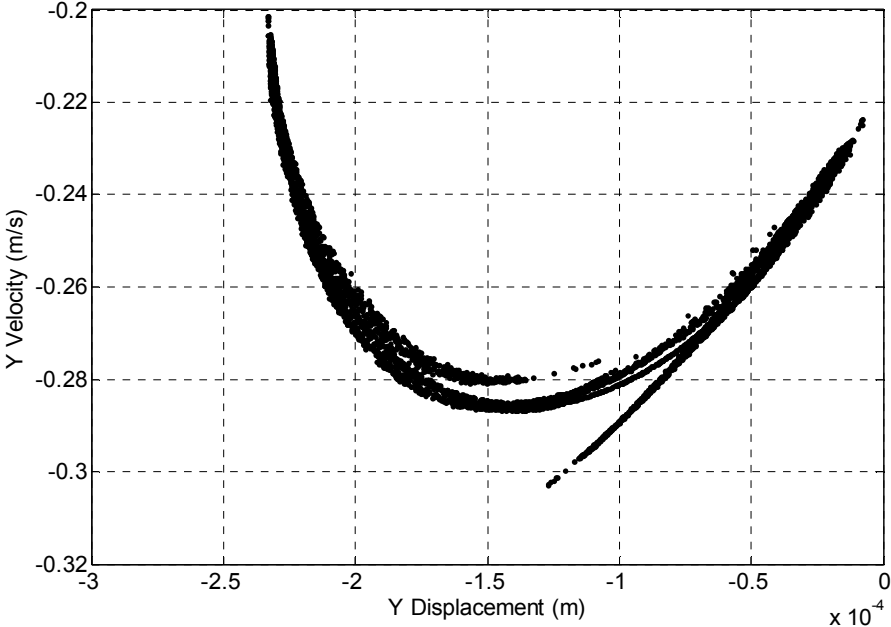
Fig. 4.27 Poincaré plot for Y response. e=7.885x10^{-5}, 5000 forcing periods at 13000 rpm
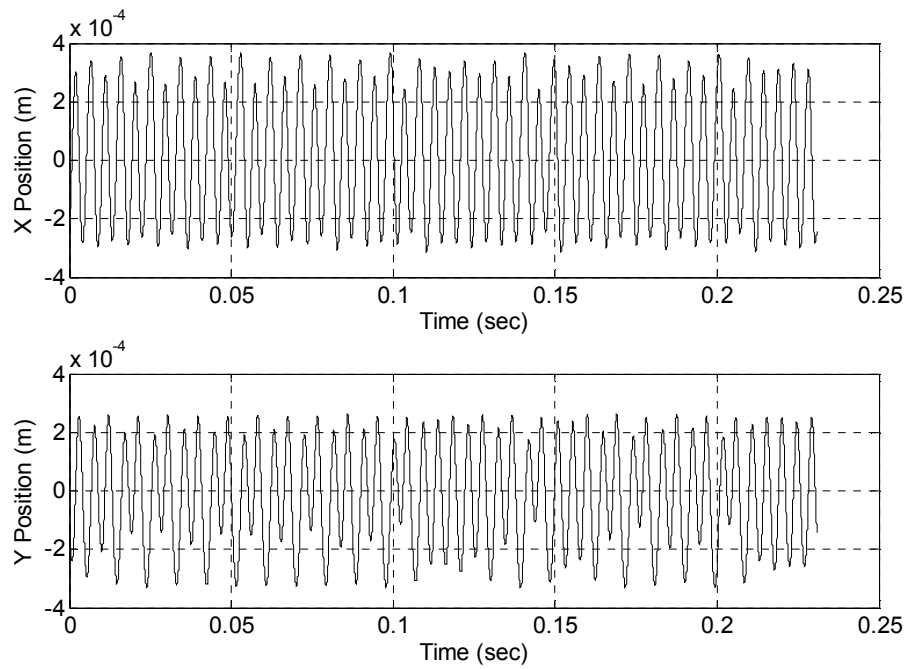
Fig. 4.28 X and Y position vs. time plot with e=7.885x10^{-5} for 50 forcing periods at 13000 rpm
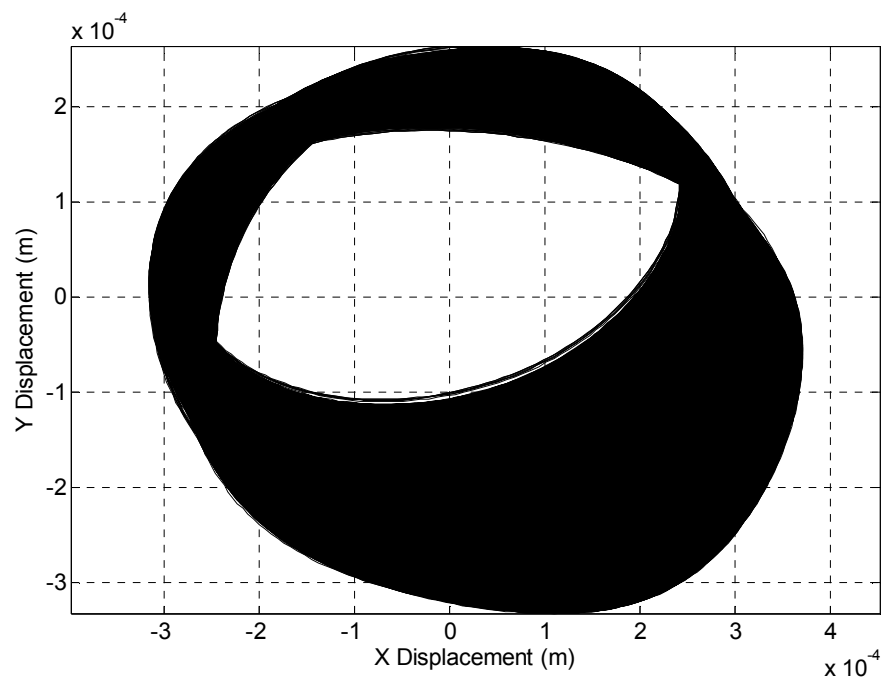
Fig. 4.29 Orbit plot with e=7.885x10^{-5} for 5000 forcing periods at 13000 rpm

4.4 Trigonometric collocation method (TCM) for periodic solutions

Trigonometric collocation method may be used to solve nonlinear period systems, i.e. periodic solution of a periodically forced nonlinear dynamic system such as steady state response of an unbalanced rotor in a nonlinear magnetic bearing[15]. In this section, TCM is investigated for finding the periodic solutions of the nonlinear rotor-bearing system that has flux saturation in the PMB HoMB model.

The method is analytic because it uses trigonometric functions in approximating the periodic solution by a Fourier series in which the frequencies are multiples or fractions of the fundamental frequency. It is also numerical because trigonometric functions and the unknown Fourier coefficients which result from substituting the assumed solution into nonlinear differential equations are found by a nonlinear algebraic equation solver. Similar to the previous sections, the Levenberg-Marquardt algorithm[24] is used to solve the set of nonlinear algebraic equations.

In the trigonometric collocation method (TCM), a periodic rotor orbit is approximated by Fourier series,

$$x(\tau) = a_{x,0} + \sum_{q=1}^{H_{pos}} \left\{ a_{x,q} \cos(q\omega_s\tau) + b_{x,q} \sin(q\omega_s\tau) \right\}, \tag{23}$$

$$y(\tau) = a_{y,0} + \sum_{q=1}^{H_{pos}} \left\{ a_{y,q} \cos(q\omega_s\tau) + b_{y,q} \sin(q\omega_s\tau) \right\}, \tag{24}$$

where $a_{x,0}, a_{x,q}, b_{x,q}, a_{y,0}, a_{y,q}, b_{y,q}$ are the coefficient to be solved for, and ω_s is the smallest frequency of interest, H_{pos} is the number of harmonics of ω_s, and τ is the collocation time. And given that the power amplifier gain is 1A/V, the currents at each pole can be

determined from the control voltage after **CDM** in terms of x and y position and velocity

(PD gains are used for the controller).

$$V_{control,x}(\tau) = K_{px}(x_{ref} - x(\tau)) + K_{dx}(\dot{x}_{ref} - \dot{x}(\tau)),$$
$$V_{control,y}(\tau) = K_{py}(y_{ref} - y(\tau)) + K_{dy}(\dot{y}_{ref} - \dot{y}(\tau)), \tag{25}$$
$$I(\tau) = \mathbf{CDM} \times \begin{bmatrix} V_{control,x}(\tau) \\ V_{control,y}(\tau) \end{bmatrix}.$$

The magnetic forces are calculated from the fluxes while the nonlinear algebraic Eq. (7)

are solved with the inputs as X and Y positions and currents. Because of the implicit

relations in this set of equations, the fluxes also need to be approximated by Fourier

series,

$$\phi_k(\tau) = a_{\phi_k,0} + \sum_{q=1}^{H_{flux}} \left\{ a_{\phi_k,q} \cos(q\omega_s\tau) + b_{\phi_k,q} \sin(q\omega_s\tau) \right\}, \quad k = 1, \cdots, 6, \tag{26}$$

where $a_{\phi_k,0}, a_{\phi_k,q}, b_{\phi_k,q}$ are the coefficients to be solved for, H_{flux} is the number of

harmonics of ω_s, and τ is the collocation time. The differential forms of Eqs. (23) and

(24) are

$$x'(\tau) = \sum_{q=1}^{H_{pos}} \left\{ -a_{x,q} q\omega_s \sin(qw\tau) + b_{x,q} q\omega_s \cos(q\omega_s\tau) \right\},$$
$$x''(\tau) = \sum_{q=1}^{H_{pos}} \left\{ -a_{x,q} \left(q\omega_s\right)^2 \cos(q\omega_s\tau) - b_{x,q} \left(q\omega_s\right)^2 \sin(q\omega_s\tau) \right\}, \tag{27}$$

$$y'(\tau) = \sum_{q=1}^{H_{pos}} \left\{ -a_{y,q} q\omega_s \sin(q\omega_s\tau) + b_{y,q} q\omega_s \cos(q\omega_s\tau) \right\},$$
$$y''(\tau) = \sum_{q=1}^{H_{pos}} \left\{ -a_{y,q} \left(q\omega_s\right)^2 \cos(q\omega_s\tau) - b_{y,q} \left(q\omega_s\right)^2 \sin(q\omega_s\tau) \right\}. \tag{28}$$

For harmonic or superharmonic responses, $\omega_s = \omega_{spin}$, and if a subharmonic with

frequency a/b (a, b are integers) are of interest, $\omega_s = \dfrac{\omega_{spin}}{b}$, where ω_{spin} is the shaft spin

frequency. Eqs. (23), (24), and (26) are substituted into the differential Eq. (10) and the

nonlinear algebraic Eq. (7), and evaluated $2\mathcal{H}+1$ collocation nodes that are equally

spaced over the fundamental period, T $(= \dfrac{2\pi}{\omega_s})$. Total number of unknowns from

trigonometric collocation is:

$$2 \times (2H_{pos} + 1) + 6 \times (2H_{flux} + 1). \tag{29}$$

If $\mathcal{H} = H_{pos} = H_{flux}$ total $8*(2\mathcal{H}+1)$ unknowns are solved for with the same

number of nonlinear algebraic equations.

The collocation method is applied to study the dynamics of a rotor in the PMB

HoMB. The results are presented as a nonlinear frequency response curve, as shown in

Fig. 4.30. In this figure, the results from both TCM and numerical integration are plotted

for increasing (INC) and decreasing (DEC) spin speeds. The rotor-bearing system with

2-dof is given by the equations of motion, Eq. (10). The control gains used are G_p

$=91.52$, $G_d = 0.00704$, and the control target point $(X, Y) = (0, 1.524 \times 10^{-4})$ m is selected

as the static force in negative Y direction 4094 N is compensated by the forces from the

bias flux. The unbalance eccentricity e is 3.048×10^{-5} m. The order of harmonics for the

assumed solution in TCM is chosen to be 6.

In order to obtain the period-1 response with TCM in the nonlinear frequency

plot, the X and Y responses and the flux responses are assumed to have the same

frequency as the rotor spin speed. With the collocation nodes chosen, for simplicity, all

initial guesses for the coefficients are taken as zeros for the first value of spin speed. The coefficients for the previous spin speed are substituted into the current initial guesses. The results from the numerical integration are also obtained to verify the results from TCM, and agree well with those from TCM. The results from TCM shown are stable.

Fig. 4.31 shows the transient responses of the period-1 for 2 forcing periods obtained by both TCM and numerical integration when the spin speed is at 12500 rpm, decreasing. Flux density plots at Fig. 4.32 also presents the results from both methods that matches well. Thus, the period-1 responses can be predicted well by TCM even when the saturated fluxes need to be assumed for the solutions.

For the period-2 responses, a bifurcation diagram is plotted with the same
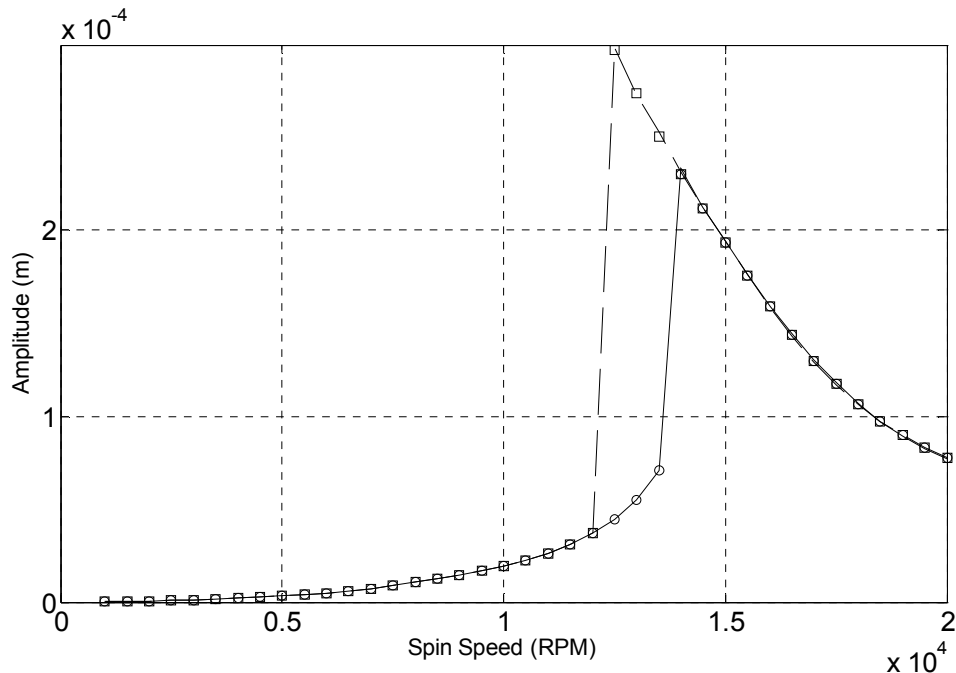
Fig. 4.30 Amplitude vs. spin speed plot. $G_p = 91.52$, $G_d = 0.00704$. Flux saturation model is included. Key: —, Numerical, INC; - -, Numerical, DEC; o, TCM, INC; □,TCM, DEC
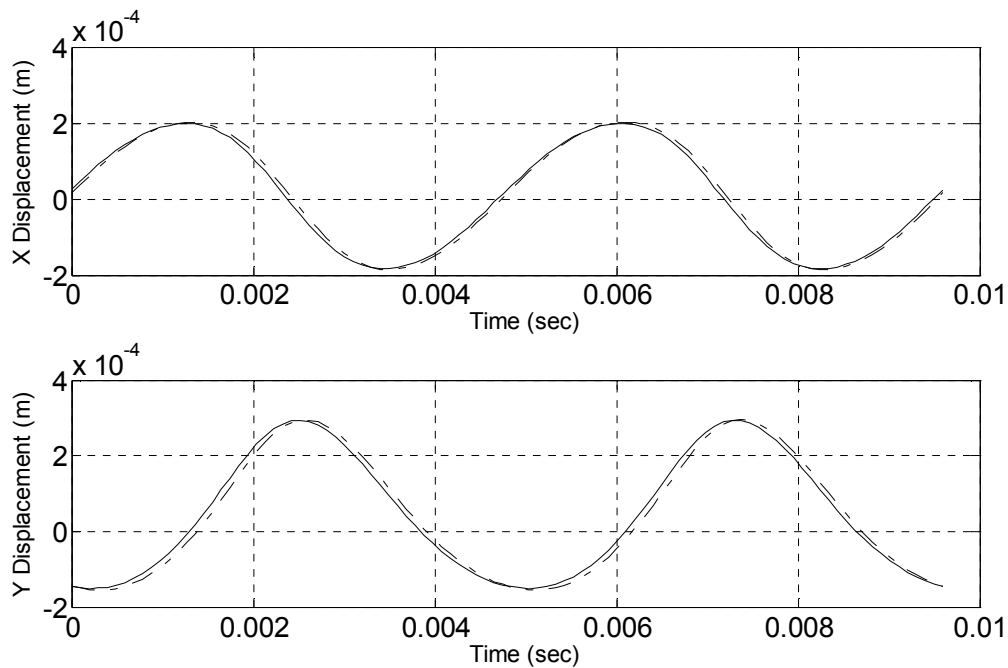
Fig. 4.31 Transient X and Y response for 2 forcing periods. RPM (decreasing) = 12500, e=3.048x10^{-5}m. Key: —, Numerical; - -, TCM

parameters used in the nonlinear frequency curve, Fig. 4.30. With the spin speed at 12500 rpm, the unbalance eccentricities as control parameter are varied in the range from 7.84x10^{-5} m to 8.103x10^{-5} m. Fig. 4.33 shows the period-2 responses at e=7.95x10^{-5} m, and with this unbalance eccentricity, the period-2 responses are compared between numerical integration and TCM. The period-2 responses obtained by TCM are similar with those from the numerical integrations, however, they contain additional high frequency components, indicating that more terms are needed in the TCM to approximate the highly saturated flux responses, as shown in Fig. 4.34 and Fig. 4.35.
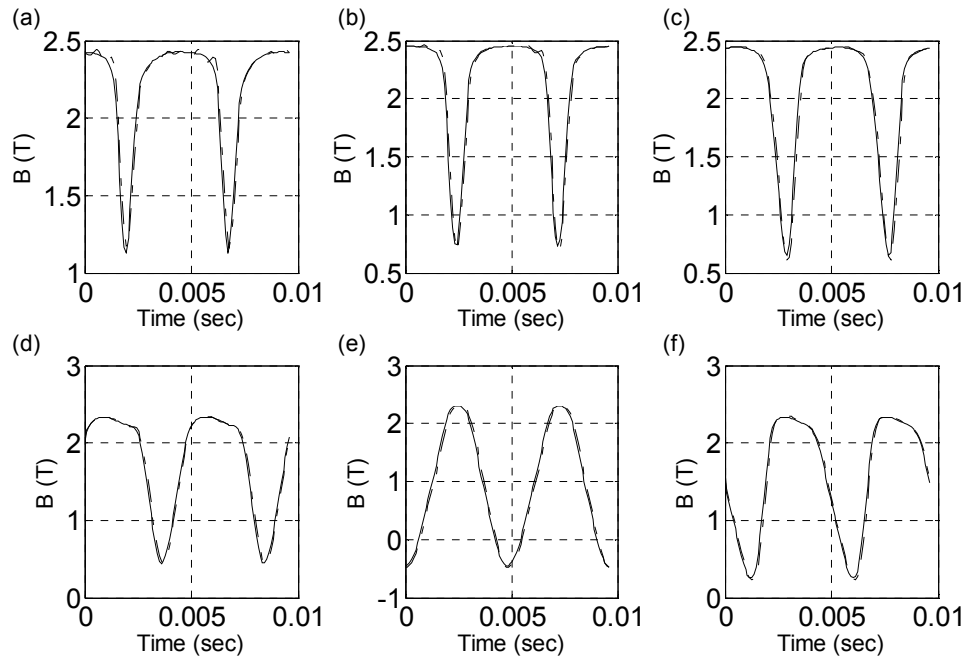
Fig. 4.32 Transient flux density response for 2 forcing periods. RPM (decreasing) = 12500, e=3.048x10^{-5}m. Key: —, Numerical; - -, TCM. (a) pole 1, (b) pole 2, (c) pole 3, (d) pole 4, (e) pole 5, (f) pole 6
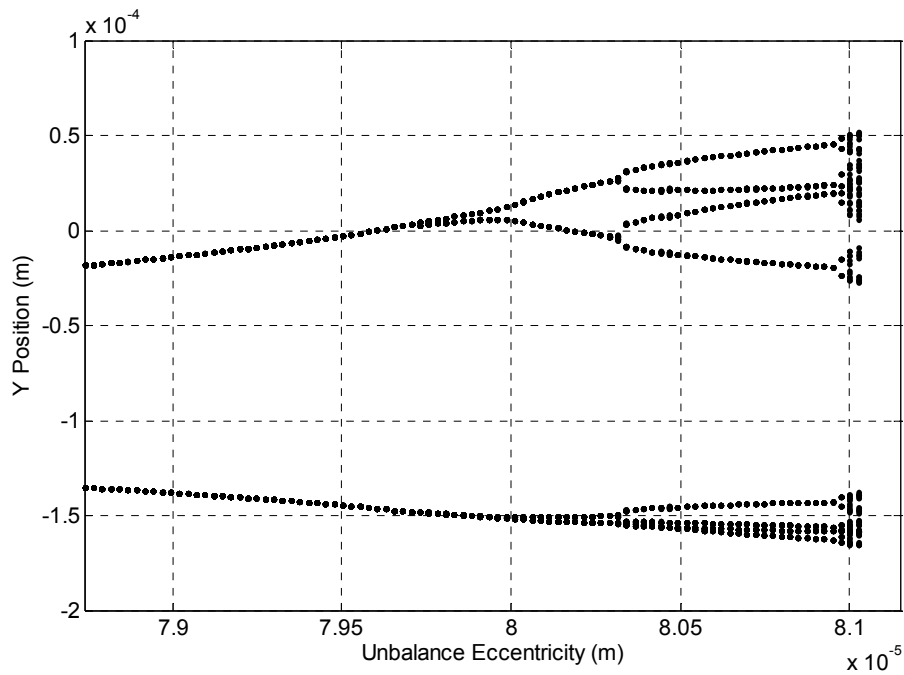
Fig. 4.33 Bifurcation diagram with unbalance eccentricity as a parameter (Y response). RPM = 13200
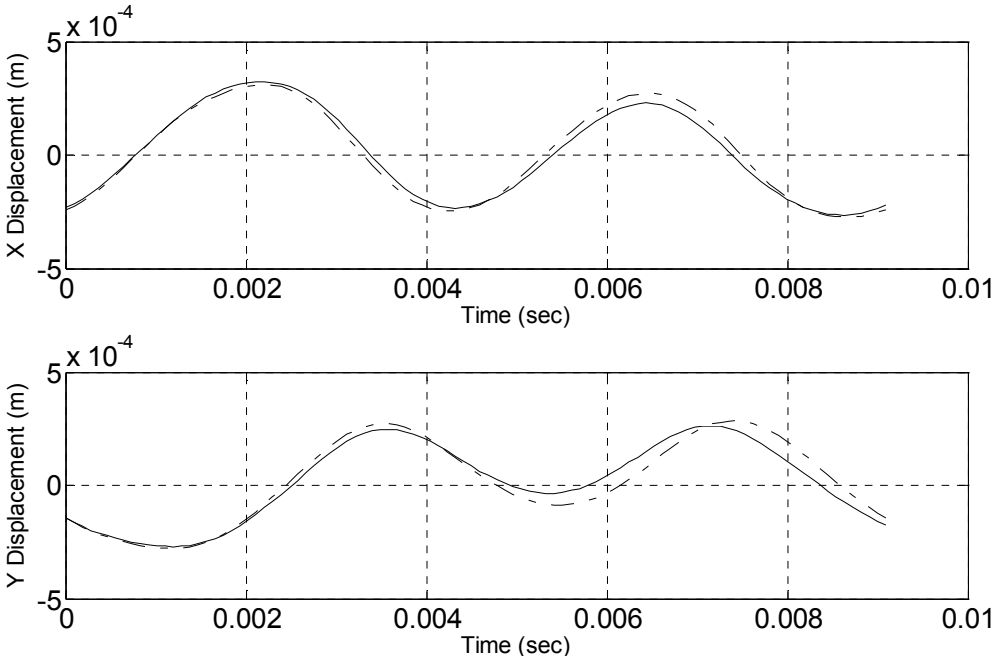
Fig. 4.34 Transient X and Y response for 2 forcing periods. RPM = 13200,
e=7.95x10^{-5}m. Key: —, Numerical; - -, TCM
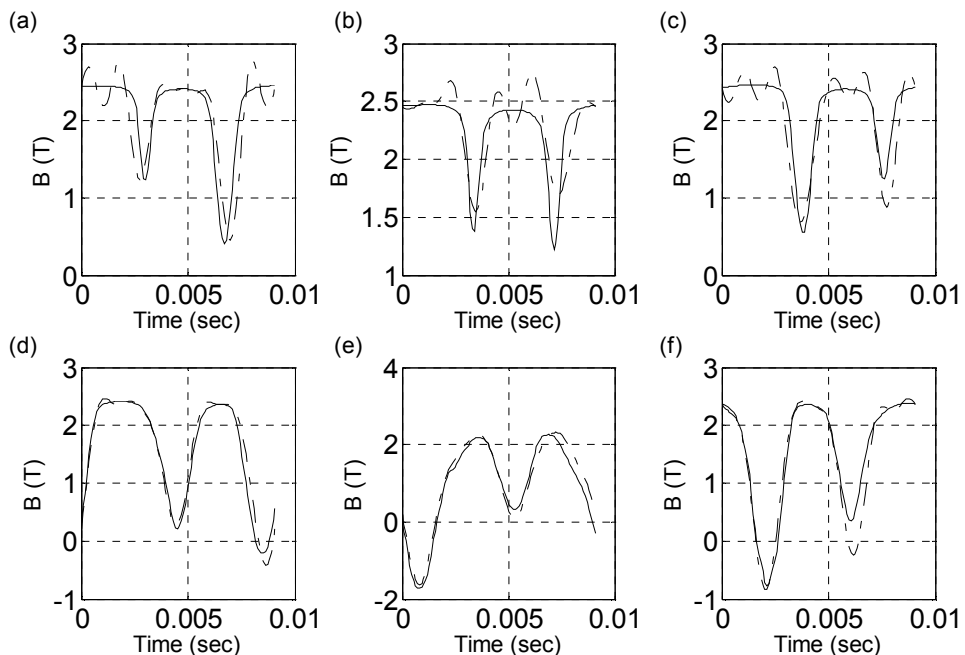
Fig. 4.35 Transient flux density response for 2 forcing periods. RPM = 13200,
e=7.95x10^{-5}m. Key: —, Numerical; - -, TCM. (a) pole 1, (b) pole 2, (c)
pole 3, (d) pole 4, (e) pole 5, (f) pole 6

CHAPTER V

DYNAMICS OF FLEXIBLE ROTOR MODEL WITH SATURATION

5.1 Natural frequencies of linearized close loop system

Nonlinear force relationship to the bearing clearance and amplifier output current along with flux saturation or without it in the material is numerically linearized at the control target point to find out the natural frequencies of closed loop with 4-dof rotor model.

Transfer function from input error to X and Y control voltage, as shown in Fig. 5.1, can be expressed as

$$\frac{V_{k,control}}{E_k} = \frac{(s+z)(G_p + G_d s)}{(s+p)(\tau s+1)^2},$$

(30)

where G_d is the derivative gain, G_p is the proportional gain, z and p are LC constants, τ is $\frac{1}{\omega_{c,LPF}}$ ($\omega_{c,LPF}$: LPF cutoff frequency, rad/sec), $V_{k,ref}$ is the reference voltage (V) depending on the target position, and G_s is the sensor gain with the value of 1969V/m.

Converting the transfer function of Eq. (30) into the differential equation form with respect to time becomes

$$\tau^2 \dddot{V}_{k,control} + \tau(2+p\tau)\ddot{V}_{k,control} + (1+2p\tau)\dot{V}_{k,control} + pV_{k,control}$$
$$= G_d \ddot{V}_{k,error} + (G_p + zG_d)\dot{V}_{k,error} + zG_p V_{k,error}.$$

(31)

The schematic of signal path between the output voltage from the controller and the input forces to the rotor is expressed in Fig. 4.2. Algebraic nonlinear (NL) equations, Eq. (7), is solved at each time step and at static condition PA can be just expressed as its
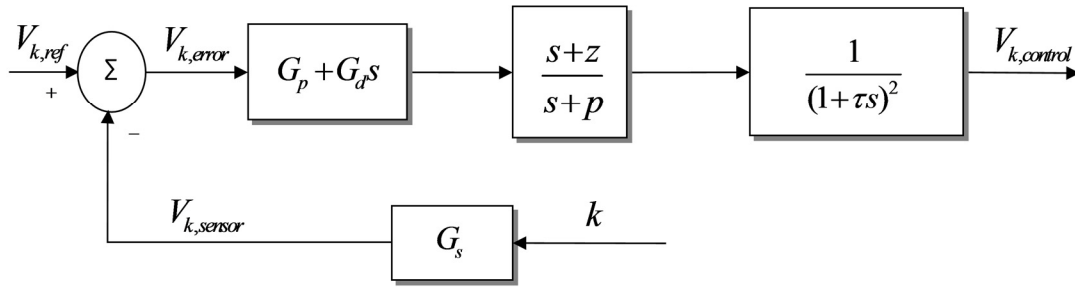
Fig. 5.1   Partial control loop from input error voltage to output control voltage

DC gain, 1A/V. This nonlinear relation can be linearized to be Eq. (19).

Fig. 4.3 shows the Y direction force calculated from Eqs. (7) and (9) without X control current and material saturation when the shaft moves in Y direction from the center of bearing. Y voltage line indicates that Y control voltage is applied while Y position is fixed at each step. Fig. 4.4 is plotted with the same way including the proposed flux saturation model. The position stiffness and voltage stiffness are calculated by Eqs. (20) and (21). The values in Table 4.1 are for the case where the flux saturation model is not considered. Table 4.2 shows the values when the flux saturation model is taken into account. The position and voltage stiffness in X and Y directions are assumed to be the same.

State variables are defined as in (32) to obtain the state space equation, neglecting all the disturbance inputs.

$$\mathbf{X} = \begin{bmatrix} x_b & \dot{x}_b & x_d & \dot{x}_d & V_{x,control} & \dot{V}_{x,control} & \ddot{V}_{x,control} & y_b & \dot{y}_b & y_d & \dot{y}_d & V_{y,control} & \dot{V}_{y,control} & \ddot{V}_{y,control} \end{bmatrix}. \quad (32)$$

The state space form of closed loop with linearized relationship between the control voltages and magnetic bearing forces is expressed combining Eqs. (11), (19), and (31) as

$$\dot{\mathbf{X}} = \mathbf{A}\mathbf{X}, \tag{33}$$

where $A_{i,j}$ is the ith row and jth column element of matrix A and

$$A_{1,1} = 1,$$

$$A_{2,1} = \frac{K_{x,p} - k_r}{M_b}(K_{x,p} > 0), \quad A_{2,3} = \frac{k_r}{M_b}, \quad A_{2,5} = \frac{K_{x,v}}{M_b},$$

$$A_{3,4} = 1,$$

$$A_{4,1} = \frac{k_r}{M_d}, \quad A_{4,3} = \frac{-k_r}{M_d},$$

$$A_{5,6} = 1, \quad A_{6,7} = 1,$$

$$A_{7,1} = \frac{G_s}{\tau^2}\left[\frac{-G_d}{M_b}(K_{x,p} - k_r) - zG_p\right], \quad A_{7,2} = \frac{-G_s}{\tau^2}(G_p + zG_d), \quad A_{7,3} = \frac{G_s}{\tau^2}\frac{G_d k_r}{M_b},$$

$$A_{7,5} = \frac{1}{\tau^2}\left(\frac{G_s G_d K_{x,v}}{M_b} - p\right), \quad A_{7,6} = \frac{-1}{\tau^2}(1 + 2p\tau), \quad A_{7,7} = \frac{-1}{\tau}(2 + p\tau),$$

$$A_{8,8} = 1,$$

$$A_{9,8} = \frac{K_{y,p} - k_r}{M_b}(K_{y,p} > 0), \quad A_{9,10} = \frac{k_r}{M_b}, \quad A_{9,12} = \frac{K_{y,v}}{M_b},$$

$$A_{10,11} = 1,$$

$$A_{11,8} = \frac{k_r}{M_d}, \quad A_{11,10} = \frac{-k_r}{M_d},$$

$$A_{12,13} = 1, \quad A_{13,14} = 1,$$

$$A_{14,8} = \frac{G_s}{\tau^2}\left[\frac{-G_d}{M_b}(K_{y,p} - k_r) - zG_p\right], \quad A_{14,9} = \frac{-G_s}{\tau^2}(G_p + zG_d), \quad A_{14,10} = \frac{G_s}{\tau^2}\frac{G_d k_r}{M_b},$$

$$A_{14,12} = \frac{1}{\tau^2}\left(\frac{G_s G_d K_{y,v}}{M_b} - p\right), \quad A_{14,13} = \frac{-1}{\tau^2}(1 + 2p\tau), \quad A_{14,14} = \frac{-1}{\tau}(2 + p\tau).$$

Therefore, the natural frequencies of linearized closed loop system can be derived from the eigenvalues of matrix A.

5.2 LPF cutoff frequency effect on close loop system

At next section, it is investigated how the flux saturation and power amplifier voltage / current saturation affect the unstable closed loop system with the flexible rotor model. And it is useful to determine linear models to provide a comparison with the nonlinear model cases that include the effects of magnetic flux saturation and amplifier voltage / current saturation.

In order to set the LPF cutoff frequency that makes closed loop system unstable, it is necessary to investigate the natural frequency of linearized closed loop system, utilizing the way described in 5.1. As shown in Fig. 5.2 and Fig. 5.3, both the damped natural frequencies and stability depends on LPF cutoff frequencies. The linearized
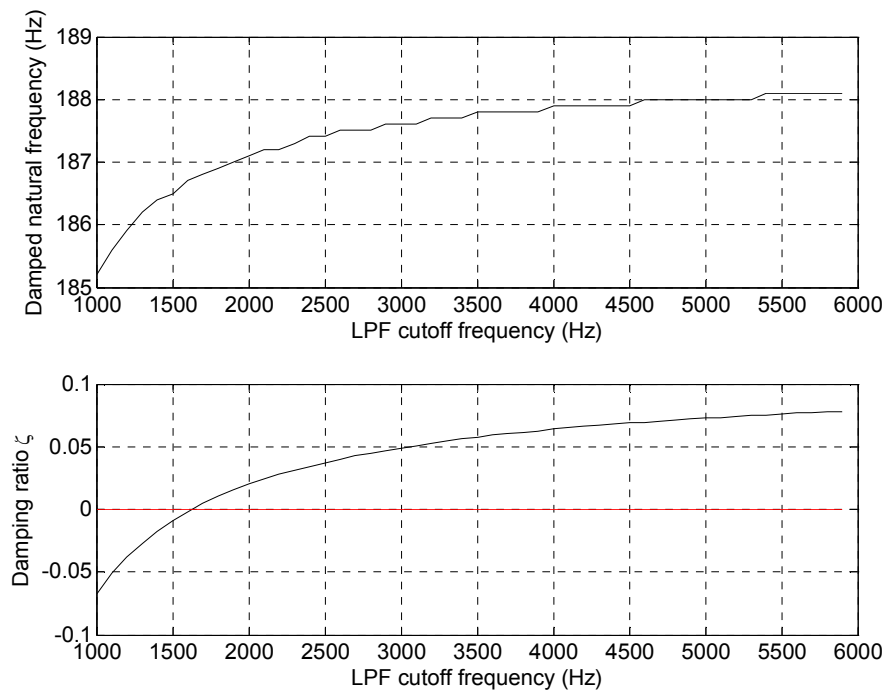
Fig. 5.2   Shaft 1$^{\text{st}}$ damped natural frequency and damping ratio of linearized closed loop system vs. LPF cutoff frequency. G_p=75.17, G_d=0.0158
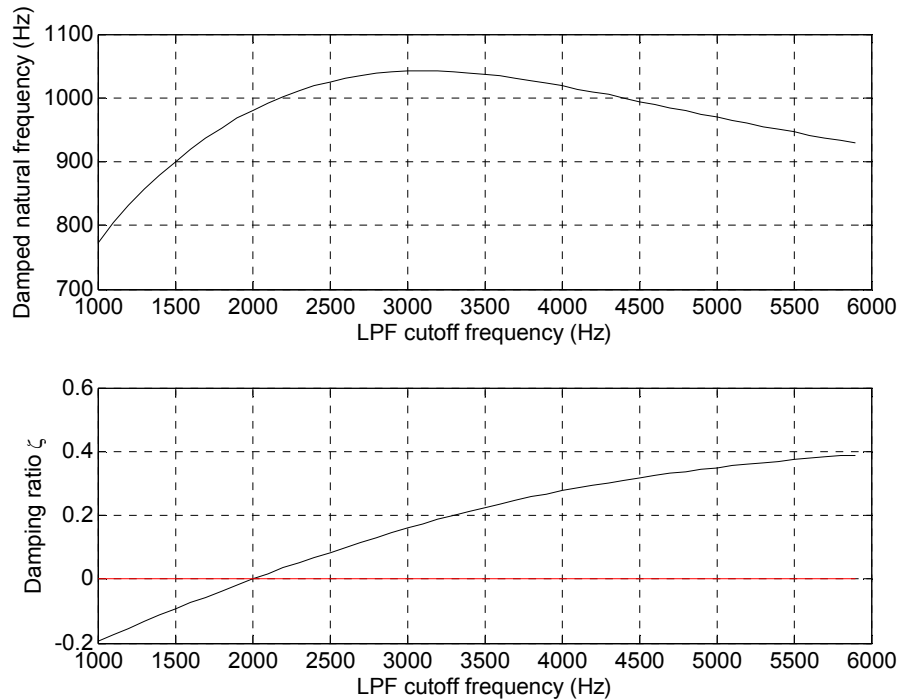
Fig. 5.3   Shaft 2nd damped natural frequency and damping ratio of linearized closed
loop system vs. LPF cutoff frequency. G_p=75.17, G_d=0.0158

closed loop system is unstable if LPF cutoff frequency is selected less than 1600 Hz,

given that the proportion gain G_p is 75.17 and the derivative gain G_d is 0.0158. Usually,

high frequency mode is oscillated to diverge when a system is unstable, so the LPF

cutoff frequency can be chosen to be maximum 2000 Hz to make an unstable system.

The damped 2nd natural frequency at given LPF cutoff frequency is used to verify the

rotor response that is calculated numerically when the system oscillates to be unstable.

5.3 Flexible shaft model with heavily loaded magnetic bearings

This section illustrates the effects of flux and power amplifier current and voltage saturations on the nonlinear dynamic response of the flexible shaft model subjected to heavy static and dynamic loading. This is representative of a high load to weight ratio bearing with light to blade-out levels of imbalance. Fig. 2.9 and Fig. 2.11 show the 4-dof flexible shaft and feedback control models. The parameters for the cases considered are shown in Table 5.1.

The target (reference) point is offset from the centered position in the opposite static load direction by an amount of 1.016×10^{-4} m in order to reduce the demand for electric current by employing the permanent magnet flux force to counteract the static load. Proportional gain (G_p) and derivative gain (G_d) of the controller are the same in x and y direction and the effective shaft stiffness (k_r) is 4.7x107 N/m. The pole path length is 3.81×10^{-2} m, the masses at the disk (M_d) and bearing (M_b) are 17.11 kg and 3.421 kg respectively. The low pass filter (LPF) stage is typically included to suppress electrical noise, shaft runout or for anti-aliasing. Note the case 1 value 1900 Hz of LPF cutoff frequency causes an unstable response for the model configuration that omits amplifier dynamics and flux saturation, based on Fig. 5.3. This is illustrated in Fig. 5.4 which shows the X and Y displacements at the disk and bearing locations. In reality these motions would cause impacts with the system's catcher bearings which are outside of the area of interest of the present work. The response remains unstable in case 2.1 where unsaturated amplifier dynamics are included in the model, as shown in Fig. 5.5. Cases 1 and 2.1 involve linear models to provide a comparison with the nonlinear model

cases that include the effects of magnetic flux saturation and amplifier voltage / current saturation.

Table 5.1 Parameter sets for saturation effect examples

Case		PA Dynamics	Voltage Saturation	Current Saturation	Magnetic Flux Saturation	LPF, PA cutoff (Hz)	Static force (N, N mm^{-2})	G_p, G_d
1		N	N	N	N	1900, N.A.	3903.8, 1.66	75.17, 0.0158
	2.1	Y	N	N	N	4000, 1000	3903.8, 1.66	75.17, 0.0403
2	2.2	Y	Y	N	N	4000, 1000	3903.8, 1.66	75.17, 0.0403
	2.3	Y	N	Y	N	4000, 1000	3903.8, 1.66	75.17, 0.0403
3		N	N	N	Y	1900, N.A.	2939.6, 1.25	75.17, 0.0158
4		N	N	N	N	2500, N.A.	3903.8, 1.66	75.17, 0.0158
5		Y	Y	Y	Y	6000, 1000	2939.6, 1.25	75.17, 0.0158

The case 3 model includes material path flux saturation but excludes current and voltage saturation (limiting) effects in the power amplifiers. The air gap fluxes are weakened by the inclusion of material path flux saturation leading to a loss of load capacity for counteracting the applied static load with the permanent magnet bias flux. The target (reference) position could be adjusted to compensate for this or the static load could be decreased to maintain the same target position in the Y direction. The latter approach was employed with a reduction of static applied load from a value of 3903.8 N to a value of 2939.6 N. Fig. 5.6 shows that the vibration becomes confined to a limit cycle similar with a Van der Pol type system, when magnetic flux saturation is included in the model. The magnitude of response is within the clearance of 5.08×10^{-4} m. This phenomenon of a limit cycle preventing destructive unstable motion has been observed

on several experimental rigs. The instability frequency 990 Hz in Fig. 5.4 indicates that the 2nd (shaft bending) mode is unstable which is consistent with the loss of phase margin caused by the power amplifier filter and LPF.

Case 2.2 in Table 5.1 is identical to case 2.1 however power amplifier voltage saturation is included with limiting voltages of ±80 volts, and current and flux saturation is excluded from the model. Fig. 5.7 shows that a limit cycle does not result from including voltage saturation and the system diverges in instability. For case 2.3, including power amplifier current saturation (limiting) at a value of ±11 amps, while excluding both voltage and flux saturation, results in a stable, limit cycle response as shown in Fig. 5.8.

Fig. 5.4   X and Y initial responses at (a) bearing and at (b) rotor, excluding flux
          saturation, power amplifier saturation and power amplifier dynamics effects

Fig. 5.5   X and Y initial responses at (a) bearing and at (b) rotor, excluding flux saturation and power amplifier saturation and including power amplifier dynamic effects

Fig. 5.6   X and Y initial responses at (a) bearing and at (b) rotor, excluding power amplifier dynamics and saturation and including flux saturation
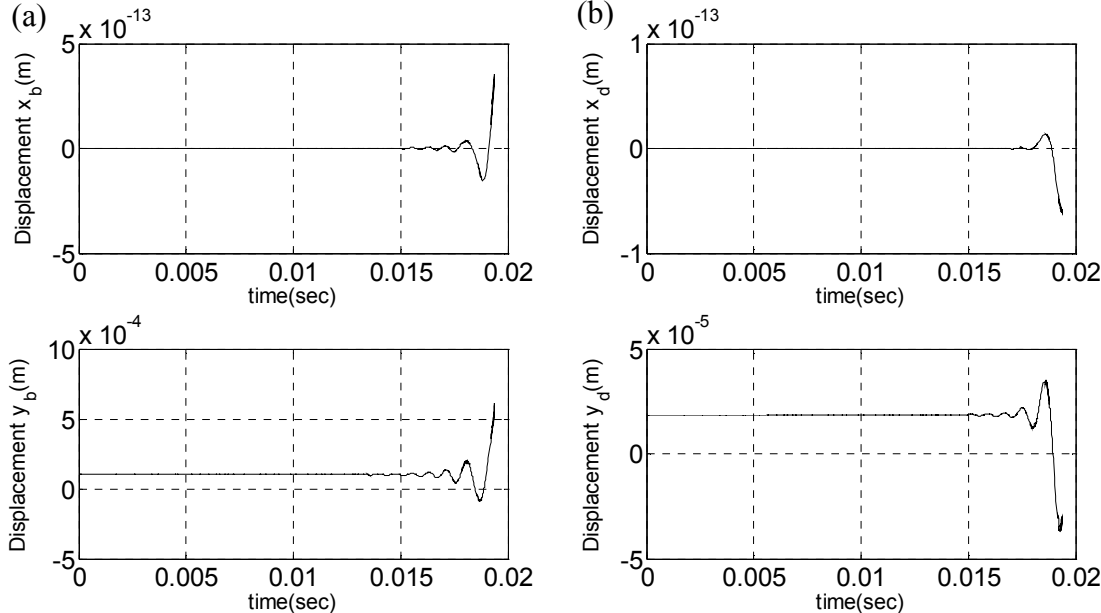
Fig. 5.7   X and Y initial responses at (a) bearing and at (b) rotor, excluding flux
saturation and including power amplifier dynamics and voltage saturation
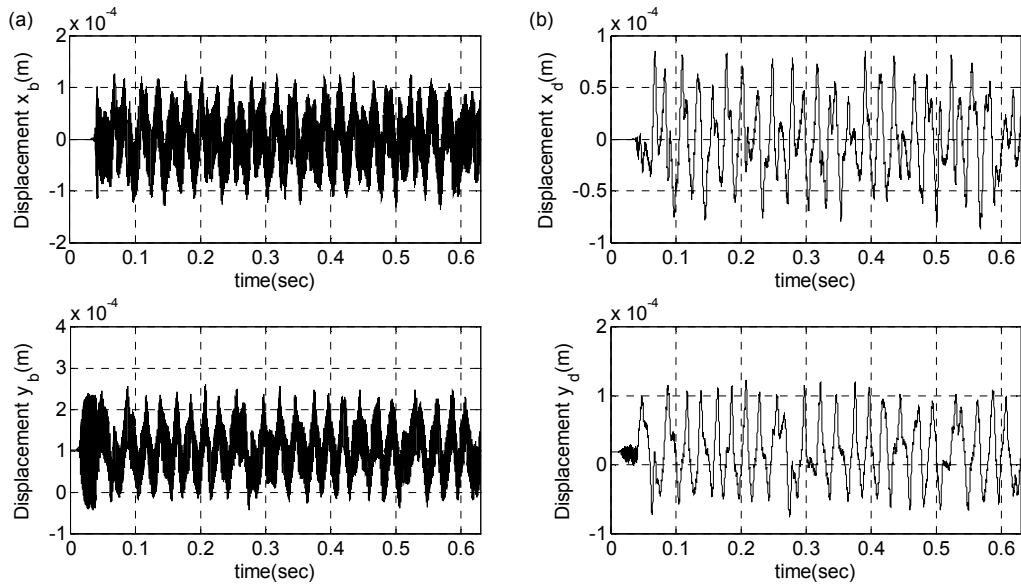
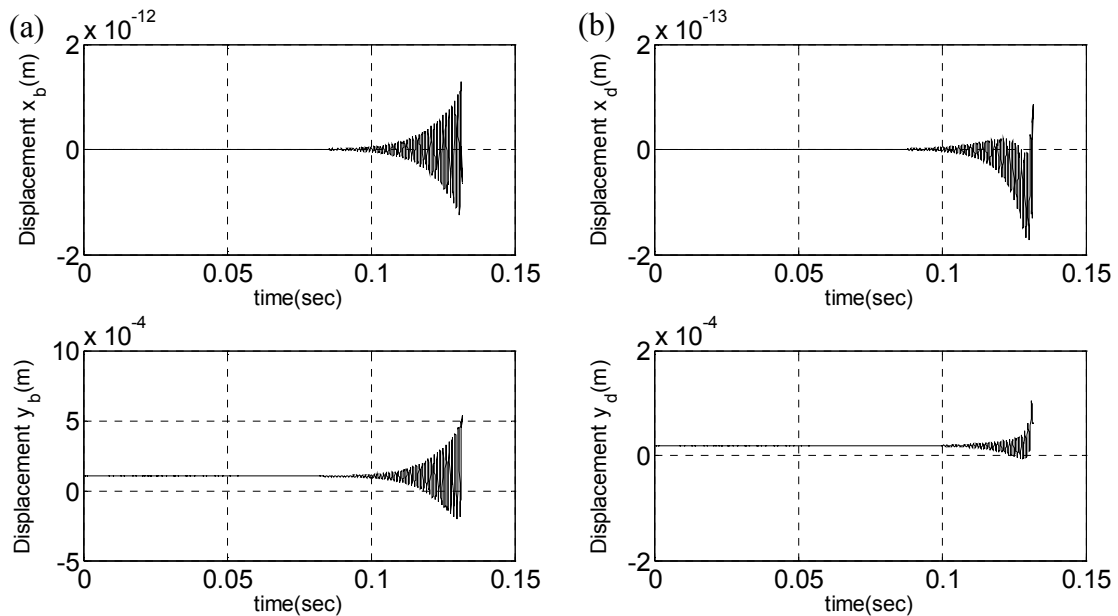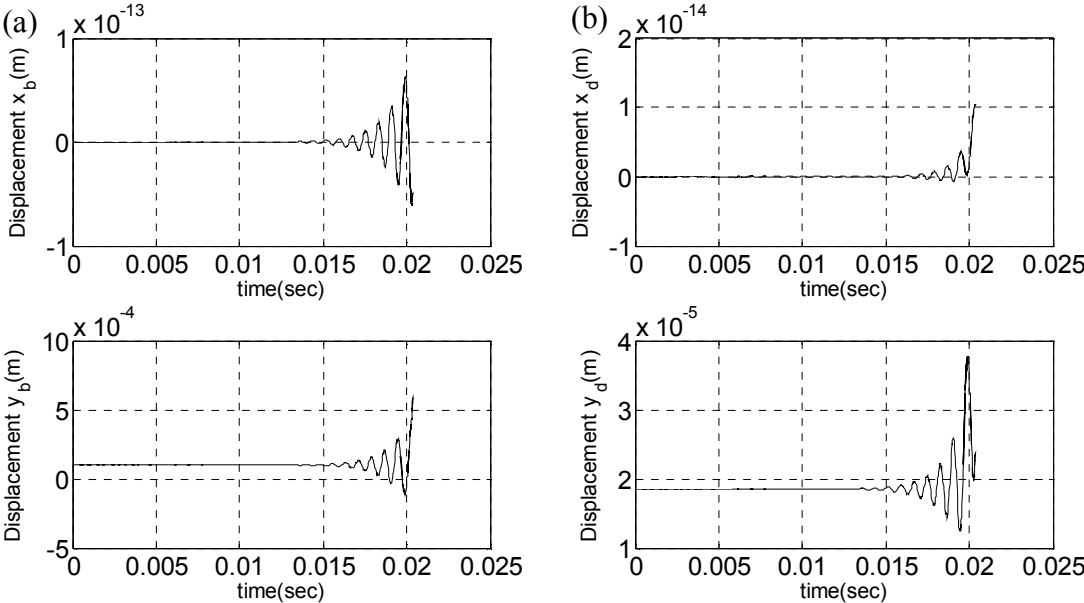Fig. 5.8   X and Y initial responses at (a) bearing and at (b) rotor, excluding flux
saturation and including power amplifier dynamics and current saturation

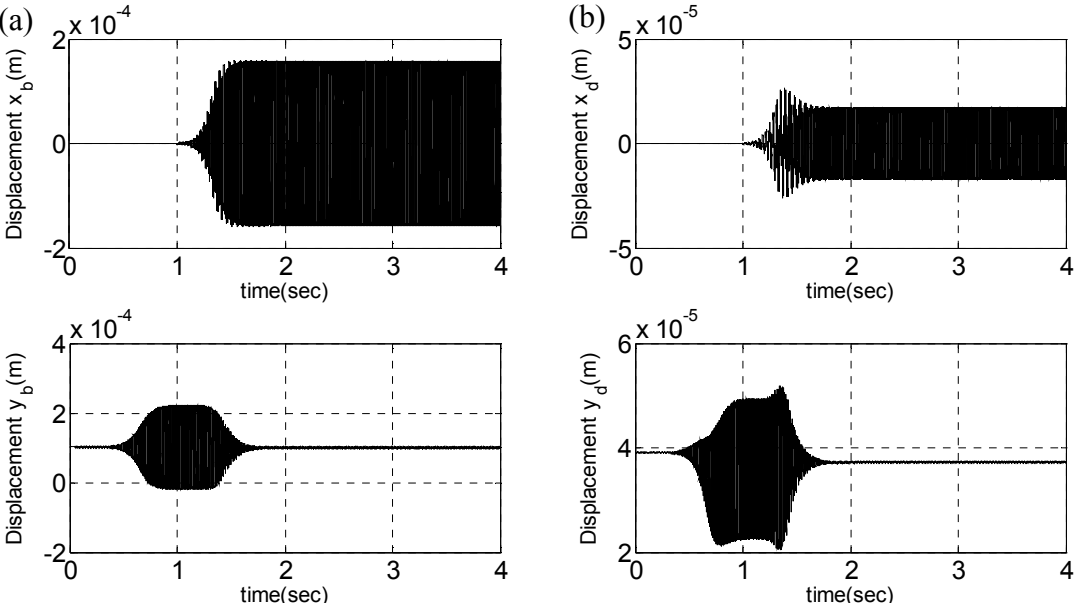## 5.4   Stable response with heavy static load and flux saturation

With the case 4 value 2500 Hz of LPF cutoff frequency in Table 5.1, the system model that omits amplifier dynamics and flux saturation remains stable at the control target position. And the system model of the case 5 that includes amplifier dynamics and flux saturation shows stable unbalance response when LPF cutoff frequency is set to 6000 Hz. This is illustrated at Fig. 5.9 and Fig. 5.10 for 20 periods when the journal rotates at 10000 rpm with the eccentricity of 3.81×10^{-5} m and the journal orbital response at the bearing is within the half of the bearing clearance, 2.54×10^{-4} m. The flux density at top 3 poles vary over saturated region (2 T), as shown in Fig. 5.11, while stable operation is maintained.
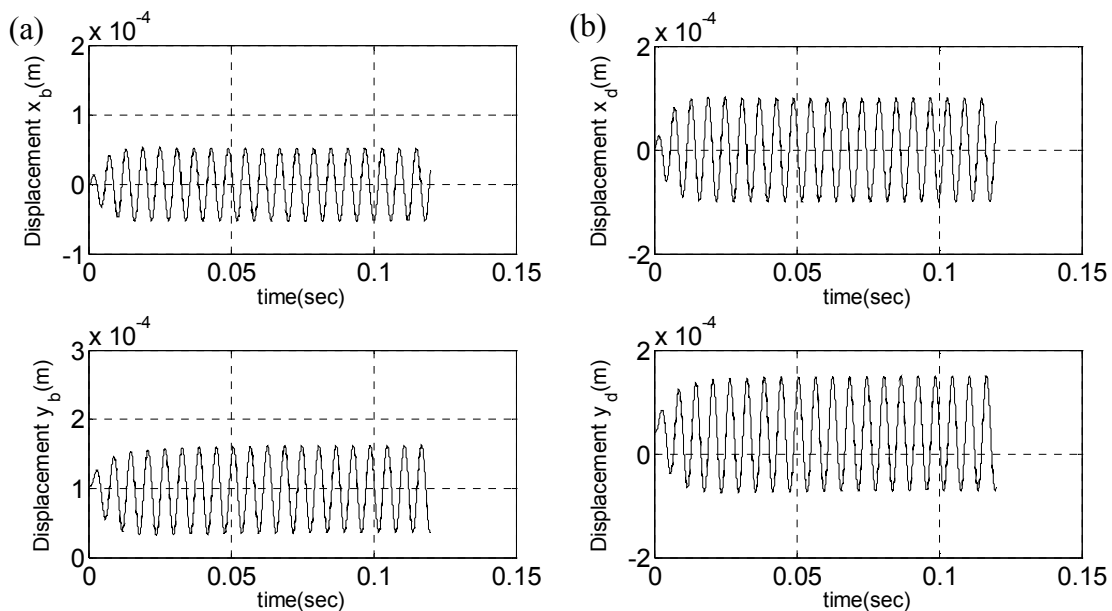
Fig. 5.9   Stable rotor response at (a) bearing and at (b) disk with the model that includes amplifier dynamics and flux saturation, when the journal rotates at 10000 rpm with the eccentricity of 3.81×10^{-5} m

Fig. 5.10 Orbit plot of stable response at (a) bearing and at (b) disk with the model that includes amplifier dynamics and flux saturation, when the journal rotates at 10000 rpm with the eccentricity of 3.81×10^{-5} m

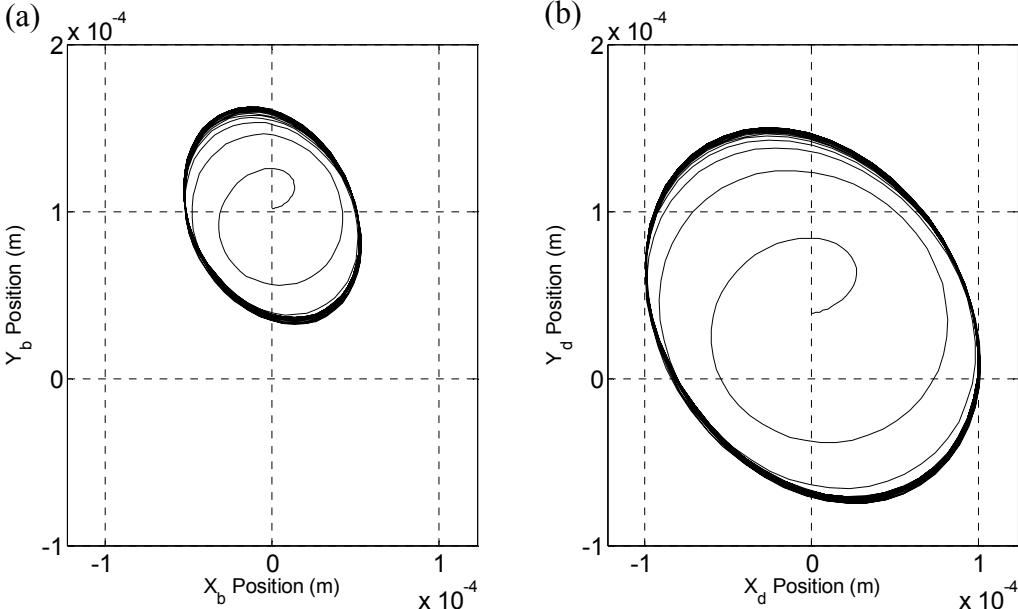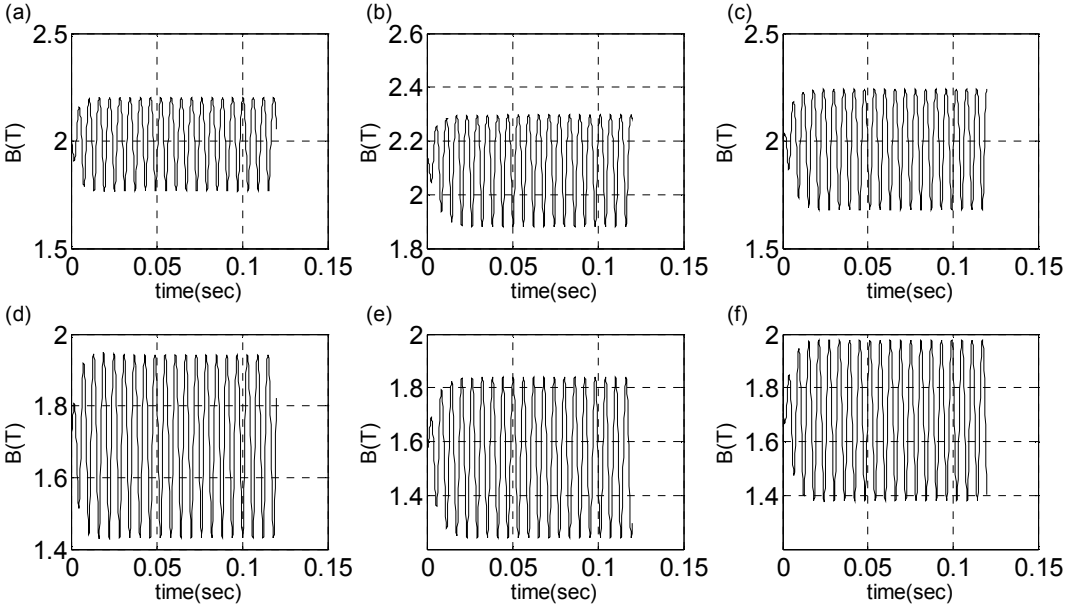Fig. 5.11 Flux density in each pole with the model that includes amplifier dynamics and flux saturation, when the journal rotates at 10000 rpm with the eccentricity of 3.81×10^{-5} m. (a) pole 1, (b) pole 2, (c) pole 3, (d) pole 4, (e) pole 5, and (f) pole 6

CHAPTER VI

SUMMARY AND CONCLUSION

The analysis of nonlinear dynamics of the flexible rotor that operates in the magnetic flux saturation zone makes it practical to utilize the full capacity of the magnetic bearings and to predict the rotor response of large amplitude or in heavily loaded situation:

(1) Modeling and simulation methodologies for including nonlinear effects in homopolar magnetic bearings were developed. Prior methods focused on heteropolar magnetic bearings.

(2) A systematic approach is made for modeling a permanent magnet-biased homopolar magnetic bearing (PMB HoMB) to express the magnetic field intensity H in terms of the flux density B, which is more suitable for solving the nonlinear algebraic equations generated from the magnetic circuit model. This analytical model of the magnetization curve provides a more accurate force prediction when the large rotor motion occurs to result the magnetic flux saturation within the bearing clearance. The standard bilinear magnetization curve approach may be unsuitable for the analysis over flux saturation limit[13], which is explained in SECTION 3.1. Modeling error can be reduced by utilizing the new modified Langmuir method with correction terms for the weak flux region when Hiperco 50 experimental magnetization data is curve-fitted.

(3) In addition to magnetic flux saturation, the investigation is made into the nonlinear dynamics of rotor-AMB system including a flexible rotor, the effects of controller gains, low pass filter, amplifier dynamics, and amplifier voltage / current saturation.

(4) The ability of actuator flux or power amplifier current saturation is demonstrated to arrest linear system instability to form a limit cycle response, a phenomena that has been observed experimentally on several experimental rigs.

(5) Investigation into nonlinear dynamics of rotor-AMB system with the above characteristics demonstrates that a flexible rotor-bearing system is able to operate stably within the flux saturation region when the external disturbance, such as unbalance force, is introduced.

This research can be extended by investigating the effect of another nonlinearity of AMB, such as eddy current [27, 28], on the dynamics of rotor-bearing system along with the amplifier dynamics and flux saturation. Also, the simulation results in this dissertation can be utilized as the basis for analysis when the experimental spin test, shown in Fig. 6.1, is performed and the data from the test are collected for comparison. Correlation between simulation and experimental data is the other valuable direction of future research.
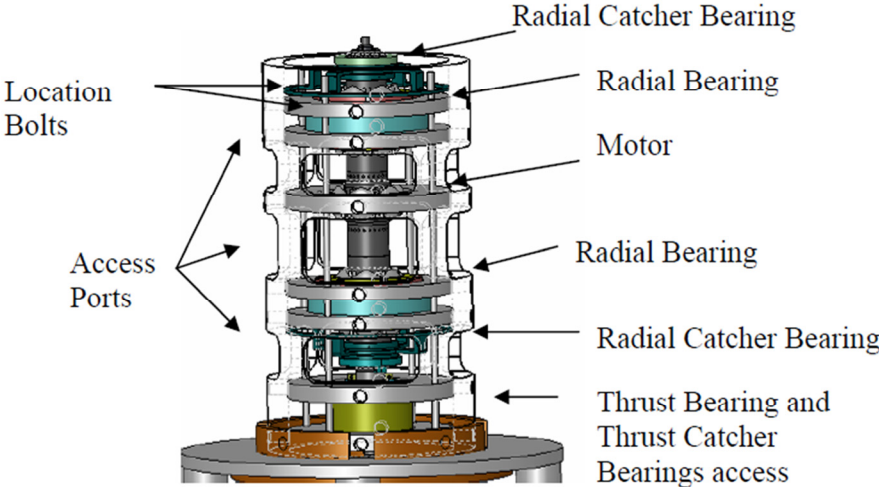
Fig. 6.1   Experimental set up for PMB HoMB

REFERENCES

[1] R. Crane, Magnetic bearings for high speed turbo molecular pumps, *Proceedings of the IEE Colloquium on High Speed Bearings for Electrical Machines*, London, UK, April 1997, pp. 4/1-4/6

[2] G. Jones, Application of homopolar magnetic bearings to turbomachinery, *Disel & Gas Turbine Worldwide* 26 (1994) 16-16.

[3] M.E.F. Kasarda, P.E. Allaire, P.M. Norris, C. Mastrangelo, E.H. Maslen, Experimentally determined rotor power losses in homopolar and heteropolar magnetic bearings, *Transactions of the ASME Journal of Engineering for Gas Turbines and Power* 121 (1999) 697-702.

[4] A. Kenny, Nonlinear electromagnetic effects on magnetic bearing performance and power loss, Ph. D. Dissertation, Texas A&M University, 2001

[5] J.C. Ji, C.H. Hansen, A.C. Zander, Nonlinear dynamics of magnetic bearing systems, *Journal of Intelligent Material Systems and Structures* 19 (2008) 1471-1491.

[6] W.K. Macfadyen, R.R.S. Simpson, R.D. Slater, W.S. Wood, Representation of magnetization curves by exponential series, *Proceedings of the Institution of Electrical Engineers* 120 (1973) 902-904.

[7] G.F.T. Widger, Representation of magnetisation curves over extensive range by rational-fraction approximations, *Proceedings of the Institution of Electrical Engineers* 116 (1969) 156-160.

[8] N. Shimatani, H. Fujita, Approximation of magnetization curves by exponential functions, *Electrical Engineering in Japan (English translation of Denki Gakkai Ronbunshi)* 101 (1981) 1-10.

[9] J. Rivas, J.M. Zamarro, E. Martin, C. Pereira, Simple approximation for magnetization curves and hysteresis loops, *IEEE Transactions on Magnetics* MAG-17 (1981) 1498-1502.

[10] E.H. Maslen, P. Hermann, M. Scott, R.R. Humphris, Practical limits to the performance of magnetic bearings: peak force, slew rate, and displacement sensitivity, *Journal of Tribology* 111 (1989) 331-336.

[11] A.-C. Lee, F.-Z. Hsiao, D. Ko, Performance limits of permanent-magnet-biased magnetic bearings, *JSME International Journal, Series C: Dynamics, Control, Robotics, Design and Manufacturing* 37 (1994) 783-794.

[12] M. Antila, Electromechanical Properites of Radial Active Magnetic Bearings, Acta Polytechnica Scandinavia Electrical Engineering Series No. 92 Helsinki University of Technology, 1998

[13] N. Steinschaden, Nonlinear Stability Analysis of Active Magnetic Bearings, *Proceedings of the 5th International Symposium on Magnetic Suspension Technology* Santa Barbara, CA, December 1999, pp. 411-427

[14] W. Zhang, J. Zu, Analysis of nonlinear dynamics for a rotor-active magnetic bearing system with time-varying stiffness, Part I. Fomulation and local bifurcation, *ASME International Mechanical Engineering Congress*, Washington, D.C., 2003, pp. 631-640

[15] M. Chinta, Steady state nonlinear rotordynamics and modeling of magnetic bearings, Ph.D. Dissertation, Texas A&M University, 1997

[16] C. Nataraj, Nonlinear analysis of a rigid rotor on magnetic bearings, *Proceedings of the International Gas Turbine and Aeroengine Congress and Exposition*, Houston, TX, June 1995, pp. 1-7

[17] I. Satoh, C. Murakami, A. Nakajima, Y. Kanemitsu, A self-excited vibraiton of magnetic bearing syste with flexible structure, *Proceedings of the 2nd International Symposium on Magnetic Bearing*, Tokyo, Japan, July 12-14 1990, pp. 329-335

[18] Y. Ishida, Nonlinear vibrations and chaos in rotordynamics, *JSME International Journal, Series C: Dynamics, Control, Robotics, Design and Manufacturing* 37 (1994) 237-245.

[19] J. Liu, P. Vora, M. Walmer, Overview of recent progress in Sm-Co based magnets, *Journal of Iron and Steel Research, International* 13 (2006) 319-323.

[20] P.E. Keuser, D.M. Pavlovic, D.H. Lane, J.J. Clark, M. Spewock, Properties of magnetic materials for use in high-temperature space power systems, *NASA Technical Report, SP-3043* (1967).

[21] Wilton, C.P.d. Silva, LAB FIT Curve Fitting Software, http://zeus.df.ufcg.edu.br/labfit, 2007.

[22] Q. Lan, A.S. Bassi, J.-X. Zhu, A. Margaritis, A modified Langmuir model for the prediction of the effects of ionic strength on the equilibrium characteristics of protein adsorption onto ion exchange/affinity adsorbents, *Chemical Engineering Journal* 81 (2001) 179-186.

[23] Z. Wodarski, Analytical description of magnetization curves, *Physica B: Condensed Matter* 373 (2006) 323-327.

[24] D. Marquardt, An Algorithm for Least-squares Estimation of Nonlinear Parameters, *SIAM Journal Applied Mathematics* 11 (1963) 431-441.

[25] M.-H. Li, A.B. Palazzolo, A. Kenny, A.J. Provenza, R.F. Beach, A.F. Kascak, Fault-tolerant homopolar magnetic bearings, *IEEE Transactions on Magnetics* 40 (2004) 3308-3318.

[26] E.H. Maslen, D.C. Meeker, Fault tolerance of magnetic bearings by generalized bias current linearization, *IEEE Transactions on Magnetics* 31 (1995) 2304-2314.

[27] D.C. Meeker, E.H. Maslen, M.D. Noh, An augmented circuit model for magnetic bearings including eddy currents, fringing, and leakage, *IEEE Transactions on Magnetics* 32 (1996) 3219-3227.

[28] H.-Y. Kim, C.-W. Lee, Analysis of eddy-current loss for design of small active magnetic bearings with solid core and rotor, *IEEE Transactions on Magnetics* 40 (2004) 3293-3301.

VITA

Name: Kyungdae Kang

Address: (Permanent address)
360-35 Yonsan8-dong, Yonje-Gu, Busan, South Korea

Email Address: kdkang92@hotmail.com

Education: B.S., Mechanical Engineering, Yonsei University, 1998

M.S., Mechanical Engineering, Korea Advanced Institute of Science and Technology, 2000

M.S., Mechanical Engineering, the University of Texas at Austin, 2003